Author: Thamarath Surendran, Smitha
Title: Towards photo-CIDNP MAS NMR as a generally applicable enhancement method
Issue Date: 2014-02-20

Towards Photo-CIDNP MAS NMR as a Generally Applicable Enhancement Method

Smitha Thamarath Surendran

Smitha Thamarath Surendran
Towards Photo-CIDNP MAS NMR as a Generally Applicable Enhancement Method
Ph.D. Thesis, Leiden University, 20th February 2014

ISBN: 978-90-821720-0-3

Cover figure designed by Dr. Tilman Kottke (tilman.kottke@uni-bielefeld.de)
Thesis Printed by Smart Printing Solutions, www.sps-print.eu

Towards Photo-CIDNP MAS NMR as a Generally Applicable Enhancement Method

PROEFSCHIFT

ter verkrijging van
de graad van Doctor aan de Universiteit Leiden,
op gezag van de Rector Magnificus C.J.J.M. Stolker,
volgens besluit van het College voor Promoties
te verdedigen op donderdag 20 februari 2014
klokke 11.15 uur

door

Smitha Thamarath Surendran
Geboren te Thrissur, India
in 1983

Promotiecommissie:

Promotores:
Prof. dr. Huub de Groot
Prof. dr. Jörg Matysik

Overige leden:
Dr. A. Alia
Dr. Tilman Kottke
Prof. dr. Jaap Brouwer
Prof. dr. Thijs Aartsma

To my Parents

CONTENTS

List of Abbreviations……………………………………………………………9

Chapter 1: Introduction…………………………………………………………….11

Chapter 2: Whole-cell NMR characterization of two photochemically active states of the photosynthetic reaction center in heliobacteria.............................27

Chapter 3: Electron spin density distribution in the special pair triplet of Rhodobacter sphaeroides R26 revealed by the magnetic field dependence of the solid-state photo-CIDNP effect...69

Chapter 4: Solid-state photo-CIDNP effect observed in phototropin LOV1-C57S by ^{13}C magic-angle spinning NMR spectroscopy...101

Chapter 5: Magnetic field dependence of the solid-state ^{13}C photo-CIDNP effect in phototropin LOV1-C57S...113

Chapter 6: General discussion..123

Summary...127

Samenvatting..129

List of publications...133

Curriculum Vitae..135

LIST OF ABBREVIATIONS

ALA	δ-aminolevulinic acid
BChl	Bacteriochlorophyll
BPheo	Bacteriopheophytin
Car	Carotenoid
DD	Differential decay
DDG	Digital delay generator
DFT	Density functional theory
DNP	Dynamic nuclear polarization
DR	Differential relaxation
EPR	Electron paramagnetic resonance
ENDOR	Electron nuclear double resonance
FMN	Flavin mononucleotide
Hb.	*Heliobacillus*
hfi	Hyperfine interaction
ISC	Intersystem crossing
LOV	Light-, oxygen- or voltage- sensitive
MAS	Magic-angle spinning
n.a.	Natural abundance
ns	Nanosecond
NMR	Nuclear magnetic resonance
OPO	Optical parametric oscillator
P	Special pair formed by two Bacteriochlorophyll *a*
P_M	Bacteriochlorophyll *a* of P attached to the M branch of the RC
P_L	Bacteriochlorophyll *a* of P attached to the L branch of the RC
PSI	Photosystem I
PSII	Photosystem II
Photo-CIDNP	Photochemically induced dynamic nuclear polarization
Rb.	*Rhodobacter*
RC	Reaction center
RPM	Radical pair mechanism
TPPM	Two-pulse phase modulation
Trp	Tryptophan
TSM	Three-spin mixing
WT	Wild type
ϕ	Bacteriopheophytin of L branch. First electron acceptor

LIST OF SYMBOLS

a_{iso}	isotropic hyperfine interaction
A_{zz}	(3,3) element of hyperfine tensor
$A_{zx},\ A_{zy}$	Pseudosecular elements of hyperfine interaction
B	Pseudosecular hyperfine interaction
D	Magnitude of electron –electron dipolar coupling

d	Electron-electron coupling
d'	Electron-electron dipolar coupling
$H_{\mathrm{S\text{-}T0}}$	Hamiltonian operator for the S-T_0 intersystem crossing
I	Nuclear spin operator
J	Electron-electron exchange coupling
S	Singlet radical state
S	Electron spin operator
S'	Fictitious electron spin operator
T	Triplet excited state of the donor
$\mathrm{T_s}$	Spin temperature
T_s	Lifetime of the singlet radical state
T_T	Lifetime of the triplet radical state
$\mathrm{T_{-1}}$	Triplet state with magnetic quantum number -1
$\mathrm{T_0}$	Triplet state with magnetic quantum number 0
$\mathrm{T_{+1}}$	Triplet state with magnetic quantum number +1
T_1	Longitudinal nuclear relaxation time
T_2	Transverse nuclear relaxation time
δ	Error of the flip angle of a $\pi/2$ magnetic pulse
ΔA	Hyperfine anisotropy
$\Delta\Omega$	Difference of the electron Zeeman interaction between the two radicals
ω_I	Nuclear Zeeman interaction

Chapter 1

Introduction

1.1 *Hyperpolarization methods*

Nuclear magnetic resonance (NMR) spectroscopy is a well known analytical technique which is used to elucidate the structure, dynamics and function of various molecules. NMR is very successful in determining structure and dynamics of small molecules and even proteins in both solution and in the solid state. The value of this technique for providing information on reaction dynamics and for constructing three-dimensional images of proteins is widely accepted. The main drawbacks of this technique are its low sensitivity and its limitation to microsecond time resolution. The unfavorable Boltzmann polarization that occurs at equilibrium conditions is a major reason for the low sensitivity.

In the presence of an external magnetic field, a spin 1/2 is found in either α or β spin orientation. The two states correspond to two energy levels with different energy values of E_α and E_β. In this context the term 'polarization' is used for the nuclear spin polarization, which is the difference of the populations (p_α, p_β) of these two levels. The energy difference ΔE for the transition of a spin from the ground state α to the exited state β depends on the magnetic field B_0, according to

$$\Delta E = E_\beta - E_\alpha = \gamma \hbar B_0. \tag{1.1}$$

In this equation γ represents the gyromagnetic ratio.

The population difference of the two levels for the spin ½ system in thermal equilibrium is governed by the Boltzmann statistics, according to

$$p_\alpha / p_\beta = \mathrm{e}^{[\Delta E/kT]} \,. \tag{1.2}$$

The term p_α/p_β is the ratio of the populations, which depends on ΔE and on the thermal energy kT. Considering a typical NMR magnet with the magnetic field of 9.4 T (*i.e.*, proton frequency 400 MHz), $\Delta E \sim 10^{-25}$ J. This ΔE is very small compared to transitions in the infrared (10^{-21} J) and the visible region (10^{-19} J). At room temperature, the ratio p_α/p_β is about $e^{0.0001}$, which is close to 1. Hence the population difference between the magnetic energy levels is very small in NMR. Because of this, the probabilities for the absorption of an incident photon or for stimulated emission are similar. The population difference is much larger in visible spectroscopy, in which almost the entire population is in the electronic ground state, and in infrared spectroscopy, in which about 90% of population is in the vibrational ground state. Therefore, and because of the higher photon energy, optical methods are generally more sensitive than NMR. The low sensitivity of NMR causes spectra with weak signal-to-noise ratio. For this reason, large amounts of samples are required. In equilibrium NMR experiments, the sensitivity is optimized by using nuclei with high gyromagnetic ratio, such as ^{1}H. In addition long acquisition times, high magnetic fields, cooled electronics and isotope enriched samples are used to enhance the sensitivity.

An alternative approach for increasing the sensitivity of NMR signals is the creation of non-Boltzmann polarization, so-called "hyperpolarization", which can be expressed as a spin temperature

$$T_s = -h\nu/k \ln(p_\alpha/p_\beta). \qquad (1.3)$$

The T_s can be negative if the nuclear spin states are inverted, corresponding with negative signals in the spectrum.

Several hyperpolarization methods have been developed for increasing the enhancement of NMR signals and their sensitivity. Some of these techniques are dynamic nuclear polarization (DNP),[1,2] optical pumping,[3] optical nuclear polarization,[4] parahydrogen induced polarization,[5,6] chemically induced dynamic nuclear polarization (CIDNP) in liquids[7-9] and in the solid state.[10] Using these hyperpolarization methods, NMR signals can be enhanced by a factor of more than 10000.

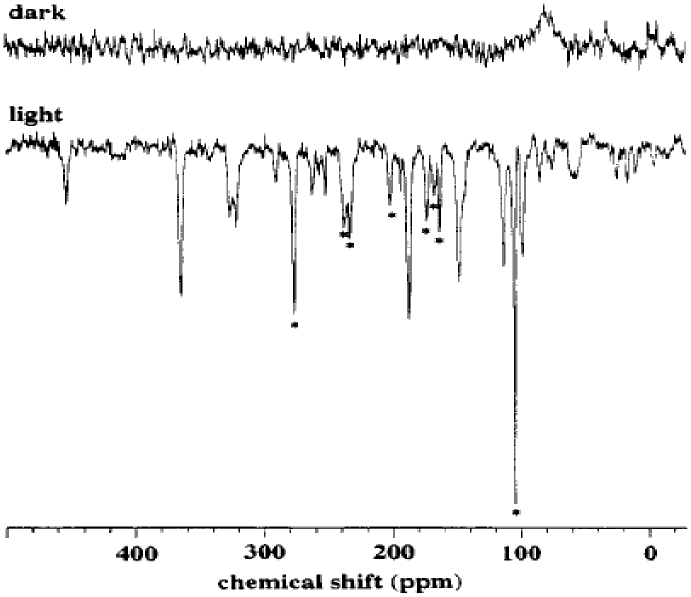

Figure 1.1. The first photo-CIDNP MAS NMR experiment reported in 1994 by Zysmilich and McDermott using ^{15}N labeled RCs of *Rb. sphaeroides* R26 .[10]

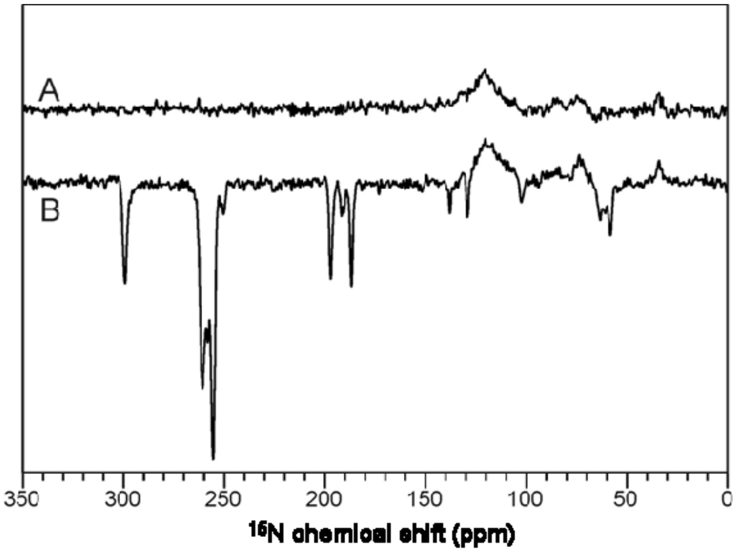

Figure 1.2. ^{15}N MAS NMR spectra of ^{15}N labeled RCs of *Rb. sphaeroides* R26 in the dark (A) and under illumination with continuous white light (B).[11]

1.2 Theory of solid-state photo-CIDNP effect

1.2.1 *Origin of solid-state photo-CIDNP effect*

Photo-CIDNP of dye molecules in solution is a well known hyperpolarization technique,[12,13] which has been discovered in 1967.[7-9] This technique has been explained using the radical pair mechanism (RPM) soon after its discovery.[14,15] In this mechanism, the different chemical fate of the products results in nuclear spin sorting. The origin of photo-CIDNP in liquids relies on the intersystem crossing (ISC) of the spin state of a photoexcited radical pair between the triplet state (T_0) and the singlet state (S) due to coherent S-T_0 mixing. The ISC is primarily due to hyperfine coupling and depends on the nuclear spin states in the radical pair. Thus, the S and T_0 states are correlated to excess and deficiency of the two spin states, respectively. Whether there is an excess of α or β nuclear spin states in the S state of the radical pair depends on the sign of the hyperfine coupling. The radical pair in its singlet state may then recombine to form ground state products. For the radical pair in its triplet state, this process is spin-forbidden, thus it diffuses apart to form escape products. If the products of the two reaction branches have different chemical shifts, nuclear polarization of the same magnitude with different sign induced in singlet and triplet products will be observable in the NMR spectrum. These two contributions of nuclear polarization would cancel each other if singlet and triplet radical pair products have the same chemical fate.

For molecules in solution, photo-CIDNP is observed due to the coupling of the spin dynamics to diffusion and reaction dynamics. Hence such an explanation is insufficient to understand the mechanism of the photo-CIDNP effect in cyclic solid-state reactions. If the nuclear spin longitudinal relaxation rate in singlet and triplet reaction products is different, the RPM can also generate net nuclear polarization. This mechanism is called ‘cyclic reactions’ in liquid-state NMR[16] and ‘differential relaxation’ in solid-state NMR (see below).

The solid-state photo-CIDNP effect is the enhancement of NMR signal intensities in the solid state, where molecular diffusion does not occur.[17,18] This effect was reported for the first time by Zysmilich and McDermott in 1994 in quinone blocked frozen ^{15}N-labeled bacterial reaction centers (RCs) of purple bacteria *Rhodobactor (Rb.) sphaeroides* R26.[10] In this experiment, they observed strong enhancement of ^{15}N magic-angle spinning (MAS) NMR signals (Figure 1.1). Later, various photosynthetic RCs, as those from *Rb. sphaeroides* wild type (WT),[19] of photosystem I (PSI)[20] and II (PSII),[21-23] as well as of green sulphur bacterial RCs[24] and heliobacterial RCs[25] were analyzed using the photo-CIDNP ^{13}C and ^{15}N MAS NMR technique (for example see Figure 1.2).

An enhancement of a factor of 10000 was observed in ^{13}C photo-CIDNP MAS NMR data collected from bacterial RCs of *Rb. sphaeroides* WT and its carotenoid less mutant R26, in a magnetic field of 4.7 T.[19,26] This very strong enhancement of MAS NMR signals by the solid-state photo-CIDNP effect makes it possible to analyze the photosynthetic RCs in whole photosynthetic systems like chromatophores[25] and cells.[26,27] The solid-state photo-CIDNP effect has been observed in all natural photosynthetic RCs studied so far and it appears to be an intrinsic property of efficient photosynthetic electron transfer. Hence, the effect provides a sensitive analytical technique to study the electronic structure of RCs in great detail. The chemical shifts of the light-induced signals provide information about the electronic structure of the diamagnetic ground state after the photocycle. Similarly, the light-induced signal intensities reveal the electron spin density distribution. In continuous illumination experiments, electron spin density in the p_z orbitals is probed[28] while laser-flash experiments reveal the electron spin densities in the *s*-orbitals.[29]

The mechanism of the solid-state photo-CIDNP effect was explained[17,18,30] following photo-CIDNP MAS NMR studies of quinone depleted or reduced bacterial RCs of *Rb. sphaeroides* WT and R26, in particular on the basis of field-dependent[19,26] and time-resolved experiments.[30] The kinetics and spin dynamics are summarized in Figure 1.3. The primary electron donor (P) of the RC protein is excited to P* by illumination with light. The primary electron donor (P) is a dimer of bacteriochlorophyll (BChl) *a* denoted the “Special pair”, whereas a bacteriopheophytin (BPheo) acts as primary electron acceptor (Φ) in RC proteins. From the excited electronic state of the special pair, an electron is transferred to the primary electron acceptor to form a radial pair. Since the excited state is a pure singlet and electron transfer is much faster than coherent evolution, the radical pair is established as a pure singlet (S). In its singlet state is not an eigenstate of the S-

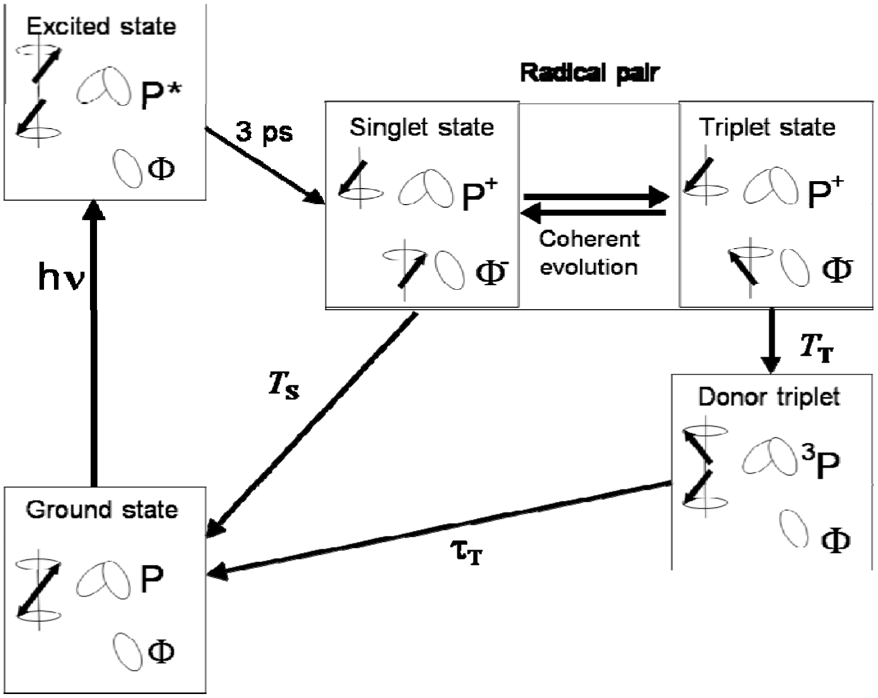

Figure 1.3 Photocycle in quinone-depleted RCs of *Rb. sphaeroides* WT and R26. Upon illumination and fast electron transfer from an excited singlet state, a radical pair is formed in a pure singlet state having high electron spin order. The radical pair is formed by a radical cation at the two donor BChls (Special pair, P) and a radical anion on the BPhe acceptor cofactor (Φ) of the active branch. The chemical fate of the radical pair depends on its electronic spin state: the singlet state is allowed to recombine with the lifetime of T_S = 20 ns and this recombination pathway is termed singlet channel. For the triplet state a direct recombination is spin-forbidden and a donor triplet (^{3}P) is formed with a lifetime of T_T= 1 ns. The lifetime of the donor triplet state (τ_T) is 100 ns for WT RCs and 100 μs for R26 RCs. The recombination pathway of the donor triplet to the ground state is termed triplet channel. Mechanisms building up photo-CIDNP under steady-state conditions are Three spin mixing, Differential decay and Differential relaxation.

T_0 subsystem, this spin-correlated radical pair[31,32] evolves into the triplet state (T_0), or it can decay to the diamagnetic ground state. The formation of the ground-state is a chemical reaction proceeding with the kinetic decay constant T_S. The coherent evolution is controlled by the secular part of the hyperfine interaction A, the coupling of the electrons d, and the difference $\Delta\Omega$ of electron Zeeman interactions between the two electrons and involves the nuclear Zeeman splitting as well.[17] For the triplet state, a direct decay to the ground state is spin-forbidden; therefore it forms a molecular triplet state on the donor (^{3}P). This chemical reaction is

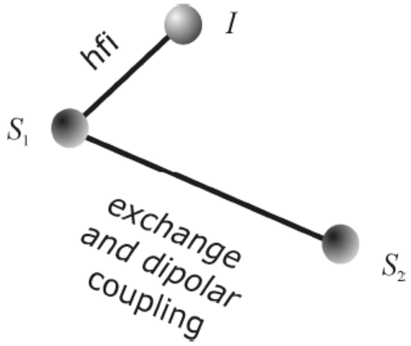

Figure 1.4. The electron-electron- nucleus model system which is used to explain the mechanisms of solid-state photo-CIDNP effect.

described with the kinetic decay constant T_T. The lifetime of the donor triplet state depends on the possibilities for relaxation by coupling to its environment. In WT RCs, the nearby carotenoid provides an excellent relaxation channel, leading to a short lifetime. In the R26 mutant, no carotenoid is available, therefore the ^{3}P lifetime is significantly longer.

Upon generation of the radical pair in a pure singlet state, perfect electron spin order is created, which is associated with zero-quantum coherence between the $S_{1\alpha}S_{2\beta}$ and $S_{1\beta}S_{2\alpha}$ electron spin states of the radical pair. This zero-quantum coherence is partially transferred into nuclear polarization by two mechanisms, called three-spin mixing (TSM) and differential decay (DD). These two mechanisms run in parallel and explain the emissive pattern of solid state photo-CIDNP NMR signals in the bacterial RCs of *Rb. sphaeroides* WT. In R26 RCs excitation produces a long-lived donor triplet, and differential relaxation (DR) occurs as a third mechanism.[26] These three competing mechanisms, which contribute to the polarization transfer from electrons to nuclei, are explained in detail below.

The solid-state photo-CIDNP effect due to the TSM and DD mechanisms is explained by assuming an electron-electron-nucleus model system (Figure 1.4). This model system consists of two electron spins S_1=1/2, S_2=1/2 and one nuclear spin I=1/2, which is hyperfine coupled to S_1. Since at high magnetic fields, the T_+ and T_- triplet states are energetically too distant to become involved, the spin dynamics occurs selectively on the S-T_0 subsystem at the zero-quantum transition of the two electron spins (Figure 1.5). In this case, the S-T_0 subsystem can be reduced to an interaction of one nuclear spin I and a fictitious electron spin $S' = ½$.[33] Now, the Hamiltonian of this S-T_0 subsystem is given by[17]:

$$H_{\mathrm{ST0}} = \Delta\Omega S_z' + \omega_I I_z + A_{zz} S_z' I_z + A_{zx} S_z' I_x + A_{zy} S_z' I_y - d S_x'. \qquad (1.4)$$

Here $\Delta\Omega$ and ω_I correspond to the electron and nuclear Zeeman interaction respectively. A_{zz} and the $B = (A_{zx}^2 + A_{zy}^2)^{1/2}$ constitute the secular and pseudosecular hyperfine coupling, respectively. The total coupling between the electrons, d, is equal to $2J+d'$. J is the exchange coupling and d' is the dipole-dipole coupling. These parameters and the kinetic constants T_S and T_T (see above) are relevant for the explanation of the photo-CIDNP effect in the solid state by TSM and DD mechanisms.

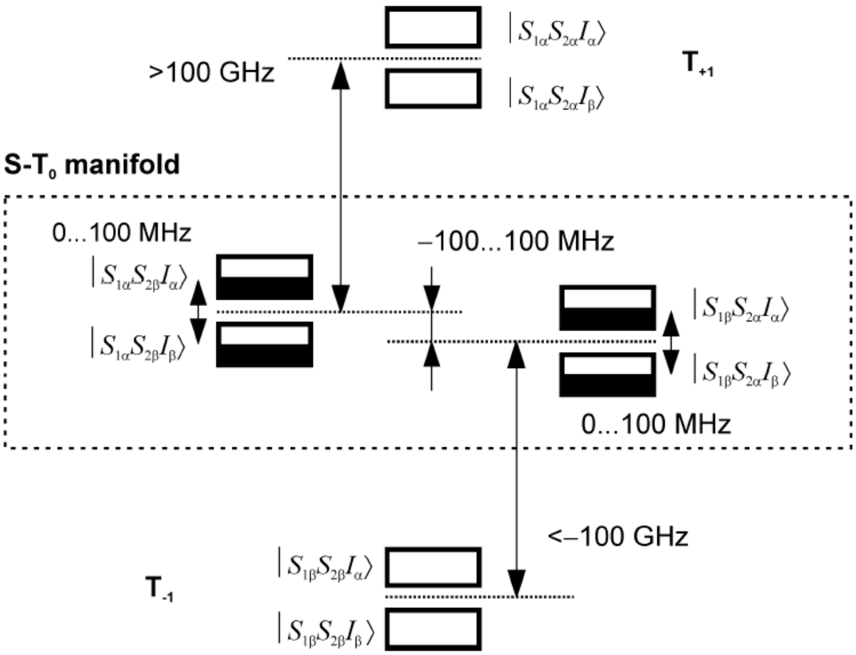

Figure 1.5. The energy levels of the radical pair. According to the Boltzmann distribution, all the spin states are virtually equally populated at thermal equilibrium. Only the singlet (S) state is populated immediately after the photo-induced electron transfer and radical pair formation. During the life time of this radical pair, the S state interconverts to the triplet radical pair T_0 resulting in an S-T_0 subsystem. The difference of the Zeeman interaction of the electron spins, the nuclear Zeeman interaction, hyperfine coupling and the electron-electron coupling are the interactions which split the S-T_0 manifold into four quantum states.

The first three terms in equation 1.4 describe the reaction dynamics according to the RPM, the last three terms are main contributing elements in three-spin mixing. The photo-CIDNP is only active in a small distance range of the radical pair: At this distance the radical pair is subject to mixing while, as often in solution, at shorter or longer distance either the $S_{1\alpha}S_{2\beta}$ and $S_{1\beta}S_{2\alpha}$ or the S and T_0 states become eigenstates and there is no possibility for such mixing.

1.2.2 *Three spin mixing (TSM)*

This pure solid-state mechanism has been proposed by Jeschke in 1997.[33] Here, the anti-symmetry of the coherent spin evolution in the correlated radical pair between the S and T_0 states is broken by state mixing due to B (terms 4 and 5 in equation 1.4) and the electron-electron dipolar coupling (term 6). The symmetry breaking concerning the nuclear states is caused by the B, which tilts the quantization axes of nuclear spins with respect to the external magnetic field. The tilt angles and tilt direction differ in the electron spin $S_{1\alpha}$ and $S_{1\beta}$ manifold. This tilt converts part of the electron-electron zero-quantum coherence that exists in a singlet-born radical pair to electron-electron-nuclear zero/single quantum coherence. A further tilt of the electron spin quantization axes by the exchange coupling or by the electron-electron dipole-dipole coupling converts part of this three-spin coherence into nuclear antiphase coherence. This corresponds to a symmetry breaking with respect to the singlet and triplet state of the radical pair. The antiphase nuclear coherence further evolves to nuclear coherence during the lifetime of the radical pair. On recombination of the pair, part of this coherence is projected to polarizations, since the tilt of the nuclear spin quantization axes due to the pseudo-secular hyperfine field suddenly vanishes.

The TSM gains maximum effect if the double matching condition is fulfilled

$$2\,|\Delta\Omega| = 2\,|\omega_I| = |A|$$

The nuclear polarization by TSM vanishes when the pseudosecular hyperfine contribution approaches zero, $B = (A_{zx}^2 + A_{zy}^2)^{1/2} = 0$, and persists at $\Delta\Omega = 0$ and $A_{zz} = 0$. The contribution of TSM to nuclear polarization is maximum at $\Delta\Omega = 0$.[17] The relevant conditions for TSM are explained in the Figure 1.6. If the double-matching condition is fulfilled, the three lowest energy levels ($S_{1\alpha}S_{2\beta}I_\beta$, $S_{1\beta}S_{2\alpha}I_\alpha$ and $S_{1\beta}S_{2\alpha}I_\beta$) in the S-$T_0$ subsystem are degenerate without the coupling terms $BS_{1z}I_x$ and

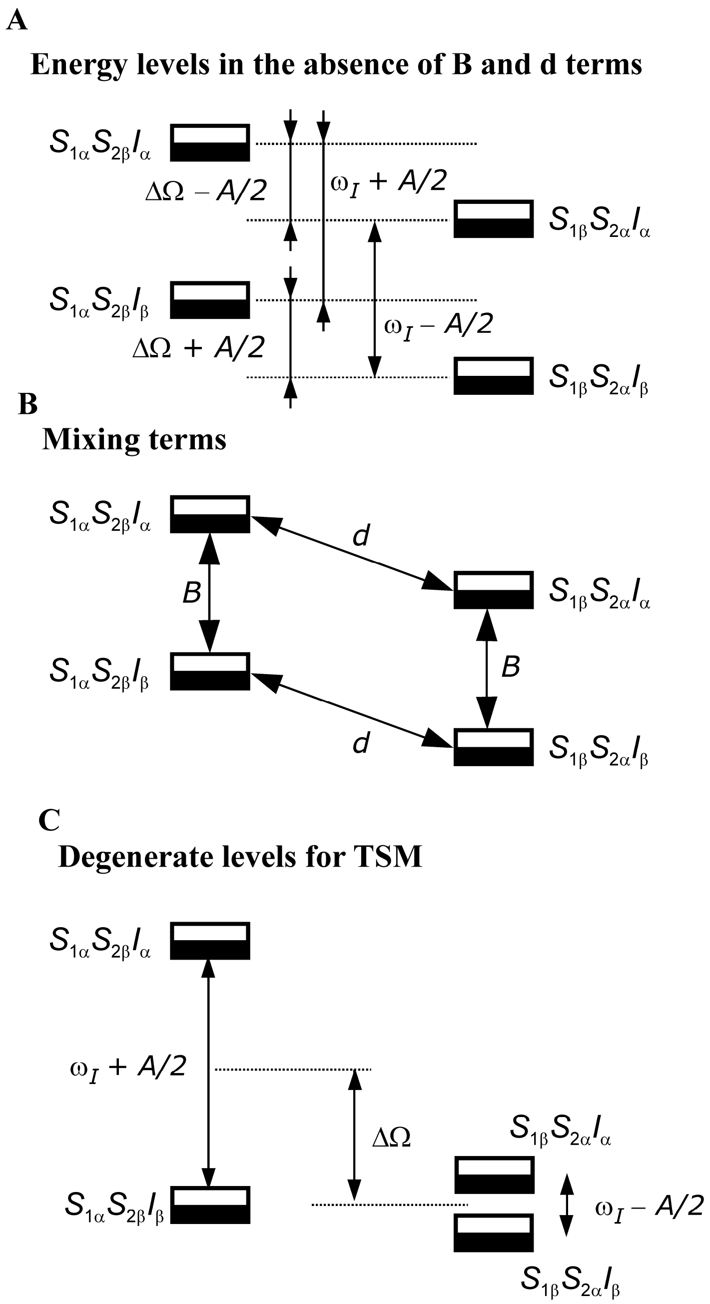

Figure.1.6. (A) Energy levels for the eigenstates according to the first three mutually commuting terms in the fictitious spin representation Hamiltonian (1.4) that provide a basis to describe the S-T_0 manifold. The pseudosecular hyperfine interaction (*B*) and the electron-electron coupling (*d*) combine the four quantum base states of the S-T_0 manifold, as indicated in panel (B). In (C) it is indicated how the double matching condition for TSM shifts the base states to produce the degeneracy.

$d(S_{1x}S_{2x}+S_{1y}S_{2y})$. The levels $S_{1\beta}S_{2\alpha}I_{\alpha}$ and $S_{1\beta}S_{2\alpha}I_{\beta}$ are degenerate for $\omega_I = A/2$ and the $S_{1\alpha}S_{2\beta}I_{\beta}$ level becomes degenerate with these two levels if also $\Delta\Omega = \omega_I$. In the initial state all four levels have almost equal initial population and in the absence of the pseudosecular couplings coherence would exist between the left and right pair of levels with the fourth level ($S_{1\alpha}S_{2\beta}I_{\alpha}$) having different energy. Electron electron coupling d splits the two degenerate energy states ($S_{1\alpha}S_{2\beta}I_{\beta}$, $S_{1\beta}S_{2\alpha}I_{\beta}$) that are coherently superimposed and converts the coherence to a transient polarization difference between the two eigenstates. In contrast, the third degenerate ($S_{1\beta}S_{2\alpha}I_{\alpha}$) and the fourth, non-degenerate level ($S_{1\alpha}S_{2\beta}I_{\alpha}$) are only weakly mixed by the electron-electron coupling d and coherence between these two levels can evolve. In addition, the pseudosecular B term of the hyperfine coupling mixes one of the coherently superimposed degenerate levels ($S_{1\beta}S_{2\alpha}I_{\alpha}$) with the third degenerate level ($S_{1\beta}S_{2\alpha}I_{\beta}$). Thus, three of the four levels ($S_{1\alpha}S_{2\beta}I_{\beta}$, $S_{1\beta}S_{2\alpha}I_{\alpha}$ and $S_{1\beta}S_{2\beta}I_{\beta}$) are strongly mixed, while the fourth, non-degenerate level ($S_{1\alpha}S_{2\alpha}I_{\alpha}$) is only weakly admixed. Spin evolution under these conditions leads to partial interconversion between electron-electron zero-quantum coherence and nuclear coherence. When the radical pair recombines, the hyperfine coupling suddenly vanishes, the quantization axis of the nuclear spin changes, and part of the nuclear coherence is converted to nuclear polarization. The contribution to nuclear polarization by the TSM mechanism also depends on the radical pair life times and the coupling d. With very large values of d, this contribution to nuclear polarization becomes negligible, since then the S and T_0 states become eigenstates and evolution of the zero-quantum coherence is blocked. In other words, the fourth level is then also strongly admixed. Hence, photo-CIDNP effect by TSM require moderate coupling between the electrons. In addition, the sign of the photo-CIDNP MAS NMR signals by the TSM contribution depends on the sign of d. Since electron-electron couplings are generally negative, TSM contributions are mostly emissive.[17]

1.2.3 *Differential decay (DD)*

The DD mechanism allows for a solid-state photo-CIDNP effect in the system without relying on the electron-electron coupling d.[34] In this mechanism, the generation of nuclear polarization from the correlated radical pair state is due to the different lifetimes of singlet (T_S) and triplet radical pairs (T_T). Numerical simulations show that[17] only a single matching of interactions is required for the polarization transfer by the DD mechanism.

$$2 \left| \omega_I \right| = \left| A_{zz} \right|$$

Note, however, that the timescales of radical pair recombination and hyperfine-induced spin evolution must also match. Similar to TSM, the Zeeman interaction and the pseudosecular hyperfine interaction B are essential for polarization transfer in the DD mechanism. The nuclear polarization by the DD mechanism vanishes if $T_S = T_T$, $\Delta\Omega = 0$, or $A_{zz}=0$. For polarization transfer in photo-CIDNP via the DD mechanism, both the secular part of hyperfine interaction and a difference between g values of the two electron spins are required. On the other hand, the DD contribution persists when the electron-electron coupling vanishes (d=0). The sign of the DD contribution to nuclear polarization depends on the sign of A_{zz}, $\Delta\Omega$, ω_I and the relative lifetimes of singlet (T_S) and triplet radical pair (T_T).

These two competing mechanisms during radical pair evolution explain the emissive ^{13}C photo-CIDNP MAS NMR signals of *Rb. sphaeroides* WT bacterial RCs. The relative intensity and the chemical shifts of these signals give information about the spin density distribution of the radical pair state and the electronic structure of the ground state, respectively.[19]

1.2.4 *Differential relaxation (DR)*

Bacterial RCs of the R26 mutant of *Rb. sphaeroides* show very similar chemical shifts of photo-CIDNP MAS NMR signals as WT RCs, but the signs of the donor signals are inverted.[26] Here, the contribution to polarization transfer is explained by the DR mechanism. In this mechanism the nuclear polarization is generated similar to the 'cyclic reactions'[16] concept within the radical pair mechanism. The nuclear polarization is created in singlet and triplet branches with the same magnitude and opposite sign, and thus usually cancels in a cyclic reaction. However, nuclear polarization is retained due to different longitudinal nuclear relaxation in both branches.[12] This occurs in the solid state due to hyperfine-induced longitudinal nuclear spin relaxation in the donor triplet state. Relaxation of the electron spin in the triplet state modulates the hyperfine field at the nucleus, which in turn causes stochastic transitions between nuclear spin states. The mechanism is termed differential relaxation (DR) mechanism.

The R26 mutant has a long living donor triplet that is not rapidly quenched by *e.g.* a carotenoid co-factor near to the special pair P as in the corresponding WT.[42] During this long lifetime of the donor triplet (τ=100 μs), when compared to that in WT (τ=100 ns), a part of triplet born polarization is relaxed. The difference of the photo-CIDNP MAS NMR spectra of *Rb. sphaeroides* WT and R26 RCs is explained by this mechanism.[35,36] Since the DR mechanism relies on relaxation induced by a stochastically fluctuating hyperfine field in the donor triplet state, the relative line intensities of the photo-CIDNP MAS NMR signals can provide information about the electron spin density distribution in the donor triplet state.

1.3 *Photo-CIDNP MAS NMR set-up*

1.3.1 *Setup for continuous illumination photo-CIDNP MAS NMR.*

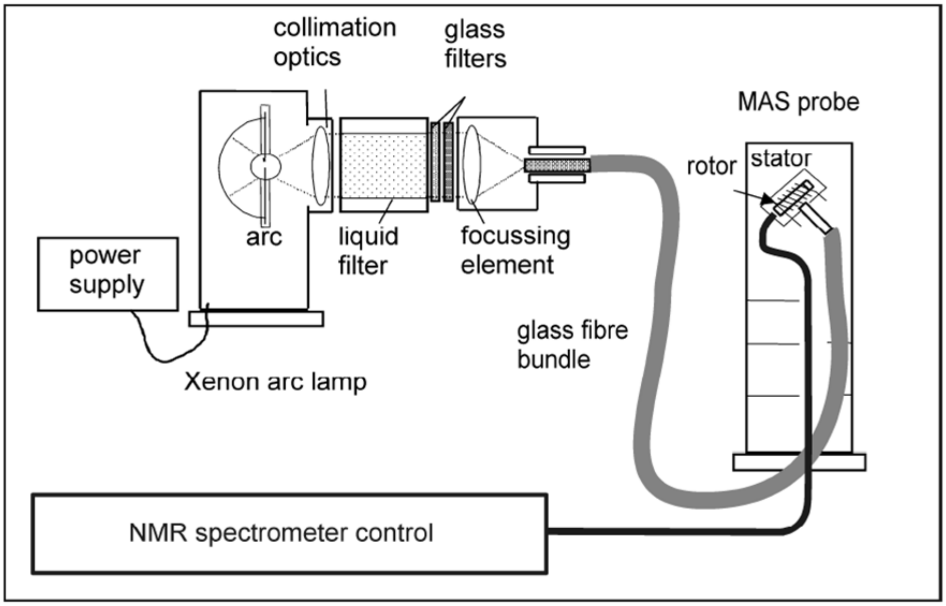

Figure 1.7: The setup for continuous illumination photo-CIDNP MAS NMR experiments

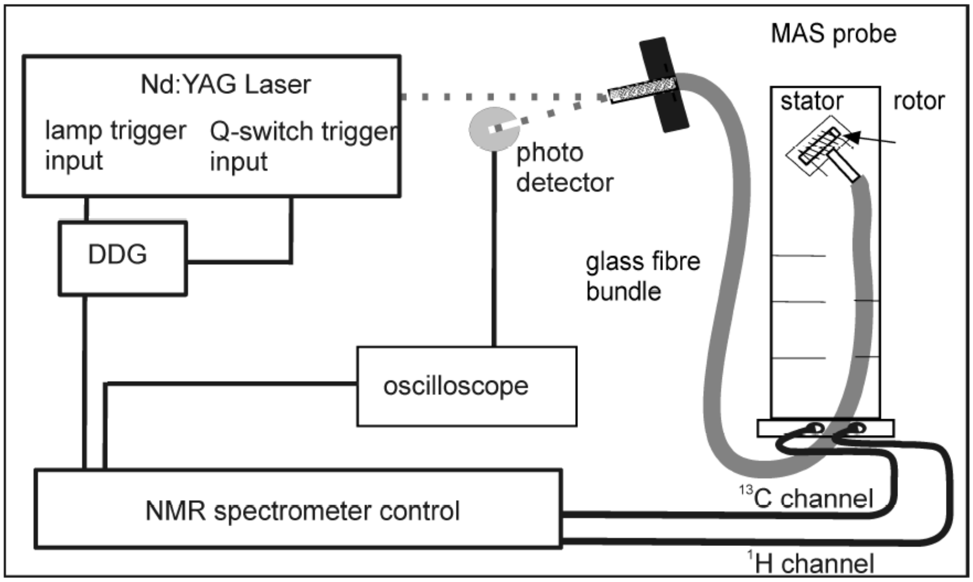

Figure 1.8. The setup for time resolved photo-CIDNP MAS NMR experiments.

Figure 1.7 shows the setup for continuous illumination photo-CIDNP MAS NMR experiments. For illumination of the sample, a 1000 W xenon arc lamp equipped with collimation optics, liquid filter and glass filters is used. The sample is illuminated with radiation similar to sunlight, which includes the range from UV to IR. The IR radiation is filtered using liquid and glass filters. An optical fiber is used to connect the illumination setup to the sample and it is attached to the stator of the MAS NMR probe. The probe was already modified for getting proper illumination from the side and the changes include (a) a bore drilled into the upper partition plate which separates the electronics and stator; (b) a small opening made in the stator to illuminate the sample; and (c) a coil wound from thin silver wire. Transparent sapphire rotors are generally used for allowing a homogeneous illumination of the sample. The Hahn echo pulse sequence[37] with two-pulse phase modulation (TPPM) proton decoupling[38] is used for collecting continuous illumination photo-CIDNP MAS NMR spectra.

1.3.2 *Laser setup for time-resolved photo-CIDNP MAS NMR*

A nano-second laser setup is used for time resolved photo-CIDNP MAS NMR studies for getting information about the electronic structure of RCs at atomic resolution. The laser setup shown in the Figure 1.8 consists of a laser with a 15 Hz repetition rate at 532 nm. This wavelength is opted for because green light gives maximum penetration to optically dense samples. A digital delay generator (DDG) is used to trigger the pump lamps, exciting both the Nd:YAG crystal and the laser Q-switch. The DDG is connected to the NMR spectrometer control that provides the triggering impulse by NMR pulse programming. A fiber aligner is used to fix the multimode optical light fiber. Laser pulses with pulse widths of 6-8 ns and energies between 20-270 mJ were produced. A 500 MHz oscilloscope, which is connected to the ^{13}C channel of the spectrometer and to the homemade photo detector, checks the timing between the laser pulse and the NMR pulse. The photo-detector consists of a fast photo-diode and a custom made amplifier. The laser pulses are transferred to the sample by a multimode optical fiber, attached to the stator of MAS NMR probe.

The same NMR pulse sequence for continuous illumination experiments is used for time resolved experiments with some modifications.[39] Additional ^{13}C presaturation pulses are applied prior to each laser pulse to destroy any polarization from previous laser flashes. Due to the destruction of this primary polarization by ^{13}C presaturation pulses, the recycle delay can be reduced to ~200 ms compared to the recycle delay of ~4 s in steady state experiments.[39]

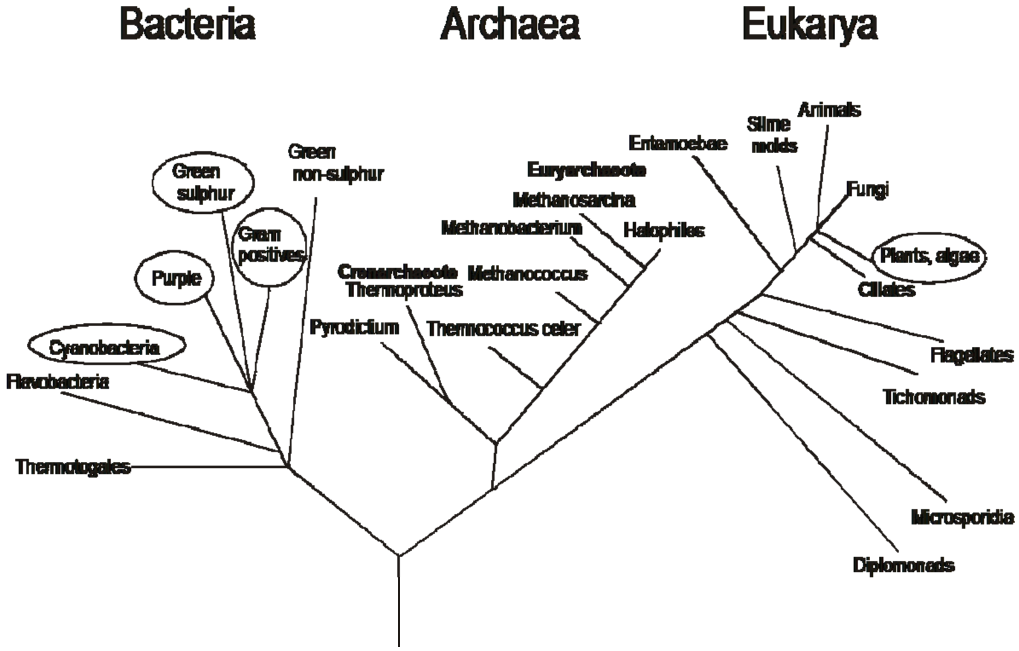

Figure 1.9. This figure shows the phylogenetic tree based on the small subunit RNA method. The photo-CIDNP MAS NMR is active in the photosynthetic organisms that are encircled.

1.4 *Applications of the solid state photo-CIDNP effect*

The solid state photo-CIDNP effect is proven to be an efficient method to analyze the electronic structure of cofactors in the RC proteins of different photosynthetic organisms. The combination with different isotope labeling methods adds further to selectivity and sensitivity. New developments as two-dimensional photo-CIDNP MAS NMR and nano-second flash photo-CIDNP MAS NMR allow exploring not only the aromatic cofactors, but also their surroundings in the protein binding pocket. The maximum enhancement of MAS NMR signals was observed in a magnetic field of 4.7 T.[19,26] Over the years, it was found that the solid state photo-CIDNP effect occurs in all tested phyla of photosynthetic organisms (Figure 1.9). It thus appears that this effect is an intrinsic property of natural photosynthetic systems.[40] Solid-state photo-CIDNP MAS NMR has been developed into a fully operational analytical method to study structure and function of different RCs in various photosynthetic organisms.

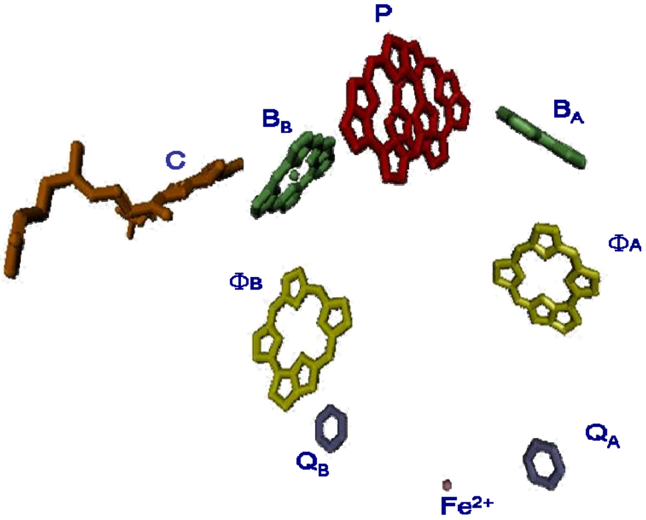

Figure 1.10: The cofactor arrangement in RCs of *Rb. sphaeroides* WT.

1.4.1 *Purple bacteria Rb. sphaeroides WT and R26.*

Rb. sphaeroides WT are anaerobic photosynthetic bacteria consisting of a photosynthetic apparatus with photosynthetic RC proteins and two light harvesting (LH) complexes, LH1 and LH2. The sunlight is captured by these LHs, which transfer the excitation energy to the RC.[41] The RC is a transmembrane protein complex in which the light (L) and medium (M) polypeptides subunits bind the cofactors. The cofactors of RC proteins consist of a well-interacting homodimer of BChl *a* molecules, two non-interacting BChl *a*, two BPheo *a* molecules, two ubiquinone-10 (Q) molecules, a non-heme iron (Fe^{2+}) and a carotenoid molecule. These cofactors are arranged in two branches, the active A branch and the inactive B branch. The homodimer of BChl *a* forms a special pair P, which is the primary electron donor. The other BChl *a* molecules are located on either side of the special pair and function as accessory pigments (B_A and B_B). The primary electron acceptor BPheo *a* molecules (Φ_A and Φ_B) are situated below the special pair in Figure 1.10. The quinones Q_A and Q_B are located below this and finally the Fe^{2+} is placed at the center of the two branches. The carotenoid that is placed near B_B breaks the symmetry of this cofactor arrangement. This carotenoid is absent in the RC of the mutant strain, *Rb. sphaeroides* R26.

Even though the RC protein has a symmetric structure, the electron transfer pathway is asymmetric and charge separation proceeds selectively through the A branch.[42] The special pair P of the RC is formed by two BChl *a* cofactors P_L and P_M, corresponding to the polypeptide chains to which they are attached. The asymmetry of the special pair P in its radical cation state has been investigated by experimental techniques like EPR, ENDOR, TRIPLE resonance studies etc. These studies reveal excess electron density in P_L compared to P_M.[43-45] This asymmetry has been attributed to a different packing structure for the two BChls in P_L and P_M, in combination with other effects of the environment around the special pair.[43] These experimental techniques have not been able to provide information about the ground state electronic structure of the special pair. Photo-CIDNP MAS NMR on site specific ^{13}C labeled RCs of *Rb. sphaeroides* WT is the only technique which has provided insight into the ground state electronic structure of the special pair.[19] Moderate differences in the electronic structure between the two BChl molecules of the special pair in the electronic ground state are observed by photo-CIDNP ^{13}C MAS NMR chemical shifts. This difference was attributed to hydrogen bonding of one of the BChl molecules.[46] The delocalisation of a major fraction of the electron spin density over the two BChl molecules of the special pair and the photochemically active BPhe is also confirmed from these experiments.[46] Photo-CIDNP MAS NMR shows very strong enhancement of NMR signals from the RCs of *Rb. sphaeroides* WT. These experiments revealed that the electron spin density ratio of special pair cofactors P_L and P_M is 3:2 in the radical cation state.[19] This is well in agreement with the ENDOR data.[43]

The photo-CIDNP MAS NMR spectrum was also observed in RCs of the carotenoid less mutant *Rb. sphaeroides* R26 and showed sign inversion for light induced signals in the region 170-130 ppm caused by the DR mechanism.[26] The magnetic field dependence of photo-CIDNP MAS NMR was also investigated in RCs of *Rb. sphaeroides* R26 and showed maximum enhancement in a magnetic field of 4.7 T.[26] This strong enhancement allows for 2-dimensional photo-CIDNP MAS NMR experiments on different site-directed ^{13}C labeled RCs of *Rb. sphaeroides* WT. The RFDR or PDSD pulse sequences, for example, in which the cross polarization pulse is replaced by $\pi/2$ pulse, were applied in 2-d experiments.

Chemical shift assignments of light induced signals from the special pair, accessory chlorophylls and BPheo *a* of the RCs have been obtained.[47] The time-resolved photo-CIDNP MAS NMR experiments on RCs of *Rb. sphaeroides* WT and R26 have been performed allowing for detailed understanding of the mechanism of the solid-state photo-CIDNP.[30] These experiments also provide information about the true electron spin densities at atomic resolution and help to elucidate the spin dynamics of the spin correlated radical pair at the microsecond timescale.[29]

1.4.2 *Rhodopseudomonas acidophilia* (*Rps. acidophilia*)

As for *Rb. sphaeroides*, *Rps. acidophilia* is also belonging to the family of purple bacteria. The solid-state photo-CIDNP effect was observed in ^{13}C labeled LH1-RC complexes of *Rps. acidophilia*.[48] It was detected by light induced ^{13}C MAS NMR signals in the aromatic region of the spectrum. Light induced ^{13}C MAS NMR data collected from *Rps. acidophilia* show the emissive signals very similar to those in *Rb. sphaeroides* WT RCs. Both of them have a similar distribution of electron spin density in the radical pair state.

1.4.3 *Green Sulphur bacteria: Chlorobium tepidum (C. tepidum)*

The green sulfur bacterium *C. tepidum* is an anoxygenic photosynthetic species with type I RCs.[49,50] The cofactors of the RC protein comprise eight molecules of BChl *a*, two Chl *a* molecule derivatives and carotenoids.[51,52] The primary electron donor is the homodimer of BChl *a*[52,53] and a derivative of a Chl *a* molecule acts as the primary electron acceptor.[54] The Fe-S clusters act as terminal electron acceptors.[55] The solid state photo-CIDNP effect was observed in purified FMO-RC particles of *C. tepidum*.[24] It was detected by light induced ^{13}C MAS NMR signals. The photo-CIDNP MAS NMR spectrum of *C. tepidum* shows an emissive light induced spectrum that is comparable to data obtained from *Rb. sphaeroides* WT RCs.

1.4.4 *Heliobacteria Heliobacillus mobilis (Hb. mobilis)*

Hb. mobilis, strictly anaerobic photosynthetic bacteria, are present mainly in rice paddy fields of Thailand. *Hb. mobilis* has less complex RCs and the RCs and the antennae pigments are bound to a single pigment protein complex, which is embedded in cytoplasmic membranes.[56] *Hb. mobilis* is also characterized by the presence of unique BChl *g* pigments. The primary electron donor in heliobacterial RCs is the homodimer of BChl *g*.[57,58] BChl *g* also act as antennae pigments. The primary electron acceptor is 8'-hydroxy Chl *a*.[59] The RCs of *Hb. mobilis* belong to the class of type I RCs, which possess Fe-S clusters as terminal electron acceptors.[60,61] The ^{13}C photo-CIDNP MAS NMR spectrum was observed in isolated membrane fragments of *Hb. mobilis*.[25] The photo-CIDNP spectrum shows light induced absorptive and emissive signals reminiscent of those obtained from RCs of *Rb. sphaeroides* R26. It was assumed that the positive signals were coming from the primary electron donor BChl *g* and the negative signals from the electron acceptor 8^1-hydroxy Chl *a*.[25]

1.4.5 *Plants and cyanobacteria*

In plants and cyanobacteria, the RCs possess a similar basic structure and are located in the photosynthetic membrane. They have the most complex photosynthetic systems in which both PSI and PSII can drive the light induced electron transfer simultaneously. PSI belongs to the type I RCs which have Fe-S clusters as terminal electron acceptors. In PSI, the cofactors for electron transfer are arranged in two branches which include six chlorophylls, two phylloquinones and three iron sulphur clusters.[62] The first pair, the heterodimer of Chl *a* and its epimer acts as a primary electron donor called P700 which is a strong reducing agent and the next pair of Chl *a* acts as accessory pigments. The primary electron acceptor is the third pair of Chl *a*. The phylloquinones act as secondary electron acceptors. The oxidation of water to oxygen is done by PSII in which the oxidized primary electron donor $P680^{\bullet+}$ is a strong oxidizing agent. The RC complex contains two subunits D_1 and D_2 and the cofactors are arranged in two branches.[63,64] This arrangement consists of a pair of Chl *a* molecules P_{D1} and P_{D2} and are followed by two other Chl *a* molecules. The two pheophytins, $Pheo_{D1}$ and $Pheo_{D2}$, are also

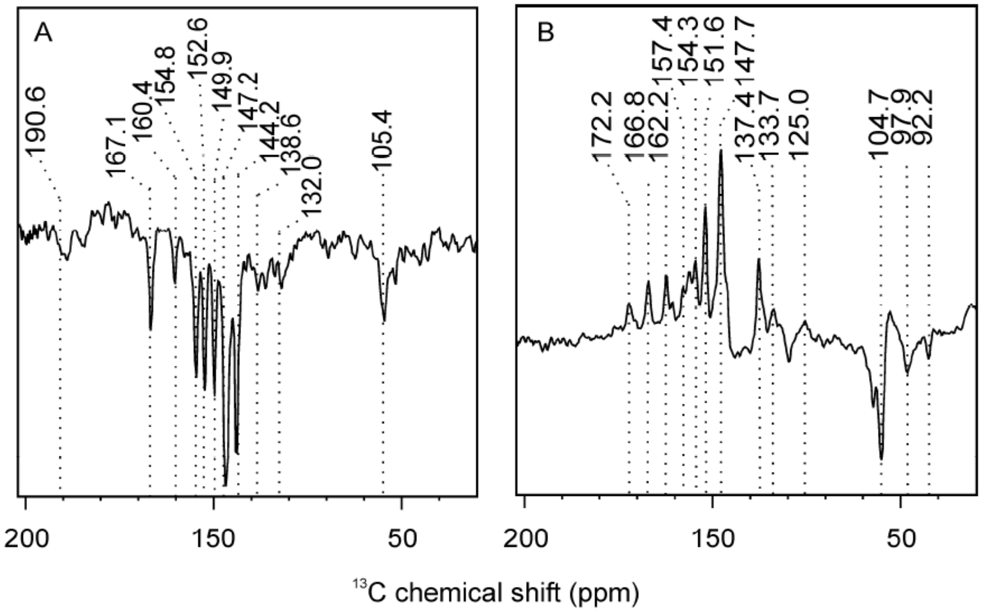

Figure 1.11. ^{13}C photo-CIDNP MAS NMR spectra of (A) PSI and (B) PSII at the magnetic field of 9.4 T and spinning frequency of 9 kHz.

present. PS II belongs to the type II RCs which have two plastoquinones. These plastoquinones act as terminal electron acceptors. The differences in electronic structure and redox properties of both photosystems in plants are yet to be fully understood.[65-67]

The solid-state photo-CIDNP effect was observed in RC preparations of PSI and PSII and detected by the huge enhancement of ^{13}C MAS NMR signals (Figure 1.11). The ^{13}C photo-CIDNP spectra of PSI preparations show emissive signals comparable to *Rb. sphaeroides* WT RCs.[20] The emissive and absorptive patterns of ^{13}C photo-CIDNP MAS NMR signals in PSII preparations are similar to those in *Rb. sphaeroides* R26 RCs.[21,22] In the photo-CIDNP spectrum of PSI, all signals are assigned to a donor cofactor Chl *a*. In PSII, the absorptive signals are assigned to a Chl *a* donor cofactor and the additional emissive signals assigned to an axial histidine that interacts with the donor. The intensities of the light induced signals in the PSII spectrum reveal the distribution of electron spin density over the donor. The difference with monomeric Chl *a* in solution is explained by the shifting of charge towards the pyrrole rings III/IV of the donor Chl *a* due to its interaction with an axial histidine.[23] This also might relate to the extraordinary redox potential of the P680$^{\bullet+}$. The photo-CIDNP studies in PSI and PSII show that the primary electron donor of PSI is the radical cation of P700 which appears to be an undisturbed cofactor Chl *a*.[20]

1.5 *Scope of the thesis*

The central issue of the thesis addresses a fundamental problem of solid state NMR spectroscopy: The increase of sensitivity and selectivity of NMR, *i.e.* to develop and improve spin-hyperpolarization methods. Various hyperpolarization methods have been developed for this purpose. One such method is the photo-CIDNP MAS NMR, a nuclear hyperpolarization method induced by photo-chemical reactions.

The photo-CIDNP MAS NMR was observed in the membrane fragments of heliobacteria *Hb. mobilis*. Photo-CIDNP MAS NMR studies on entire cells of heliobacteria *Hb. mobilis* are presented in ***Chapter 2***. RCs of *Hb. mobilis* photoisomerize to the aerobic form in the presence of oxygen. Both anaerobic and aerobic forms of *Hb. mobilis* cells are analyzed here using photo-CIDNP MAS NMR. It is remarkable that the electron transfer, the symmetric nature and the kinetics of the RCs in both forms can be resolved with the help of the photo-CIDNP MAS NMR technique, even though the X-ray structures of heliobacterial RC are not available. This chapter also demonstrates that photo-CIDNP MAS NMR can be applied as an analytical tool directly on the cellular level. It implies that this hyperpolarization method can be applied to cells and bacteria even if no further purification is known or possible.

To improve the knowledge of the solid-state photo-CIDNP effect, field dependencies are measured over large ranges (***Chapter 3***). The maximum enhancement of the photo-CIDNP MAS NMR effect is determined to be at the magnetic field of 4.7 T and it is a factor of about 10000 in the RCs of *Rb. sphaeroides* WT and R26. This matching optimum is well explained with the TSM and DD as the constituting mechanisms. For R26 RCs, the photo-CIDNP MAS NMR effect increases significantly below 4.7 T. Experimental observations, computer simulations and theoretical predictions are used to describe the effect in terms of the DR. The analysis of the DR allows constructing the electron spin density distribution in the ^{3}P donor triplet state. Hence, another mechanism with another analytical aspect stresses the versatility of photo-CIDNP MAS NMR as hyperpolarization method.

Chapter 4 describes the first observation of photo-CIDNP MAS NMR in phototropin LOV1-C57S, overcoming an old limitation of the method. Until now, the photo-CIDNP MAS NMR has been restricted only to natural photosynthetic RCs. ***Chapter 5*** provides the first analytical studies on the LOV1 system. The observation underlines the potential to develop photo-CIDNP MAS NMR into an enhancement method generally applicable to electron transfer proteins. In ***Chapter 6*** this leads to a new paradigm, expecting plenty of photo-CIDNP hyperpolarization if the experiment is optimized for the LOV1 system.

References

(1) Griffin, R. G.; Prisner, T. F. *Phys. Chem. Chem. Phys.* **2010**, *12*, 5737-5740.

(2) Leggett, J.; Hunter, R.; Granwehr, J.; Panek, R.; Perez-Linde, A. J.; Horsewill, A. J.; McMaster, J.; Smith, G.; Kockenberger, W. *Phys. Chem. Chem. Phys.* **2010**, *12*, 5883-5892.

(3) Kastler, A. *Science* **1967**, *158*, 214-21.

(4) Maier, G.; Haeberlen, U.; Wolf, H. C.; Hausser, K. H. *Phys. Lett.* **1967**, *25A*, 384-385.

(5) Bowers, C. R.; Weitekamp, D. P. *Phys Rev Lett* **1986**, *57*, 2645-2648.

(6) Bowers, C. R.; Weitekamp, D. P. *J. Am. Chem. Soc.* **1987, *109,*** 5541-5542.

(7) Bargon, J.; Fischer, F.; Johnsen, U. *Z. Naturforsch.* **1967**, *A 22*, 1551-1555.

(8) Bargon, J.; Fischer, H.; *Z. Naturforsch.* **1967,** *A 22*, 1556-1562.

(9) Ward, H. R.; Lawler, R. G. *J. Am. Chem. Soc.* **1967**, *89*, 5518.

(10) Zysmilich, M. G.; McDermott, A. *J. Am. Chem. Soc*. **1994**, *116*, 8362-8363.

(11) Prakash, S.; Tong, S. H.; Alia, A.; Gast, P.; Jeschke, G.; Matysik, J. in Photosynthesis: Fundamental Aspect to Global Perpectives, (A. ed. by van der Est, A. Bruce), Allen Press Montreal, pp. 236-237, (**2005**).

(12) Hore, P. J.; Broadhurst, R. W. *Progr. NMR Spectrosc.* **1993**, *25*, 345-402.

(13) Goez, M. (1997) *Photochemically induced dynamic nuclear polarization* In Advances in photochemistry, (eds. Neckers, D. C; Volman, D. H; von Bülau, G.) Wiley, New York, *Volume 23*, pp 63-163.

(14) Closs, G. L.; Closs, L. E. *J. Am. Chem. Soc*. **1969**, *91*, 4549-4550.

(15) Kaptein, R.; Oosterhoff, J. L. *Chem. Phys. Lett.* **1969**, *4*, 195-197.

(16) Closs, G. L. *Chem. Phys. Lett.* **1975**, *32*, 277-278.

(17) Jeschke, G.; Matysik, J. *Chem. Phys.* **2003***, 294***,** 239-255.

(18) Daviso, E.; Jeschke, G.; Matysik, J. in Biophysical Techniques in Photosynthesis II (Aartsma T.J., Matysik, J., eds.), Springer Dordrecht, pp. 385-399 (**2008**).

(19) Prakash, S.; Alia; Gast, P.; de Groot, H. J.; Jeschke, G.; Matysik, J. *J. Am. Chem. Soc.* **2005**, *127*, 14290-8.

(20) Alia; Roy, E.; Gast, P.; van Gorkom, H. J.; de Groot, H. J.; Jeschke, G.; Matysik, J. *J Am Chem Soc* **2004**, *126*, 12819-26.

(21) Matysik, J.; Alia; Gast, P.; van Gorkom, H. J.; Hoff, A. J.; de Groot, H. J. *Proc. Natl. Acad. Sci. U. S. A* **2000**, *97*, 9865-70.

(22) Diller, A.; Alia; Roy, E.; Gast, P.; van Gorkom, H. J.; Zaanen, J.; de Groot, H. J.; Glaubitz, C.; Matysik, J. *Photosynth Res* **2005**, *84*, 303-8.

(23) Diller, A.; Roy, E.; Gast, P.; van Gorkom, H. J.; de Groot, H. J.; Glaubitz, C.; Jeschke, G.; Matysik, J.; Alia, A. *Proc. Natl. Acad. Sci. U. S. A.* **2007**, *104*, 12767-71.

(24) Roy, E.; Alia; Gast, P.; van Gorkom, H.; de Groot, H. J.; Jeschke, G.; Matysik, J. *Biochim Biophys Acta* **2007**, *1767*, 610-5.

(25) Roy, E.; Rohmer, T.; Gast, P.; Jeschke, G.; Alia, A.; Matysik, J. *Biochemistry* **2008**, *47*, 4629-35.

(26) Prakash, S.; Alia, A.; Gast, P.; de Groot, H. J.; Matysik, J.; Jeschke, G. *J. Am. Chem. Soc.* **2006**, *128*, 12794-9.

(27) Janssen, G. J.; Daviso, E.; van Son, M.; de Groot, H. J.; Alia, A.; Matysik, J. *Photosynth Res*, *104*, 275-82.

(28) Diller, A.; Prakash, S.; Alia, A.; Gast, P.; Matysik, J.; Jeschke, G. *J Phys Chem B* **2007**, *111*, 10606-14.

(29) Daviso, E.; Prakash, S.; Alia, A.; Gast, P.; Neugebauer, J.; Jeschke, G.; Matysik, J. *Proc Natl Acad Sci U S A* **2009**, *106*, 22281-6.

(30) Daviso, E.; Alia, A.; Prakash, S.; Diller, A.; Gast, P.; Lugtenburg, J.; Jeschke, G.; Matysik, J. *J. Phys. Chem. C* **2009**, *113*, 10269-10278.

(31) Hore, P. J.; Hunter, D. A.; McKie, C. D.; Hoff, A. J. *Chem. Phys. Lett.* **1987**, *137*, 495-500.

(32) Closs, G. L.; Forbes, M. D. E.; Norris, J. R. *J. Phys. Chem.* **1987**, *91*, 3592-3599.

(33) Jeschke, G. *J. Chem. Phys.* **1997**, *106*, 10072-10086.

(34) Polenova, T.; McDermott, A. E. *J. Phys. Chem. B* **1999**, *103*, 535-548.

(35) Goldstein, R. A.; Boxer, S. G. *Biophys. J.* **1987**, *51*, 937-946.

(36) McDermott, A.; Zysmilich, M. G.; Polenova, T. *Solid State Nucl. Mag. Res.* **1998**, *11*, 21-47.

(37) Matysik, J.; Alia; Hollander, J. G.; Egorova-Zachernyuk, T.; Gast, P.; de Groot, H. J. M. *Indian J. Biochem. Biophys.* **2000**, *37*, 418-423.

(38) Bennett, A. E.; Rienstra, C. M.; Auger, M.; Lakshmi, K. V.; Griffin, R. G. *J. Chem. Phys.* **1995**, *103*, 6951-6958.

(39) Daviso, E.; Diller, A.; Alia, A.; Matysik, J.; Jeschke, G. *J. Magn. Reson.* **2008**, *190*, 43-51.

(40) Matysik, J.; Diller, A.; Roy, E.; Alia, A. *Photosynth. Res.* **2009**, *102*, 427-435.

(41) Hu, X. C.; Ritz, T.; Damjanovic, A.; Autenrieth, F.; Schulten. K. *Q. Rev. Biophys.* **2002**, *35*, 1.

(42) Hoff, A. J.; Deisenhofer, J. *Phys. Rep.* **1997**, *287*, 2.

(43) Lendzian, F.; Huber, M.; Isaacson, R. A.; Endeward, B.; Plato, M.; Bonigk, B.; Möbius, K.; Lubitz, W.; Feher, G. *Biochim. Biophys. Acta* **1993**, *1183*,v139.

(44) Lubitz, W.; Lendzian, F.; Bittl, R. *Acc. Chem. Res.* 2002, *35*, 313.

(45) Rautter, J.; Lendzian, F.; Lubitz, W.; Wang, S.; Allen, J. P. *Biochemistry* **1994**, *33*, 12077.

(46) Schulten, E. A.; Matysik, J.; Alia; Kiihne, S.; Raap, J.; Lugtenburg, J.; Gast, P.; Hoff, A. J.; de Groot, H. J. *Biochemistry* **2002**, *41*, 8708-17.

(47) Prakash, S.; Alia, A.; Gast, P.; de Groot, H. J.; Jeschke, G.; Matysik, J. *Biochemistry* **2007**, *46*, 8953-60.

(48) Diller, A.; Alia, A.; Gast, P.; Jeschke, G.; Matysik, J. In Energy from the sun (Allen, J.; Gantt, E.; Golbeck, J.; Osmond, B. eds.), Springer Dordrecht, pp. 55-58 (**2008**).

(49) Blankenship, R. E. *Photosynth. Res.* **1992**, 33, 91-111.

(50) Golbeck, J. H. *Proc. Natl. Acad. Sc**i. U**. S. A.* **1993**, 90, 1642-1646.

(51) Permentier, H.P.; Schmidt, K.A.; Kobayashi, M.; Akiyama, M.; Hager-Braun, C.; Neerken, S.; Miller, M.; Amesz, J., *Photosynth. Res.* **2000**, 64, 27-39.

(52) Takaichi, S.; Oh-Oka, H.; *Plant Cell Physiol.* **1999**, 40, 691-694.

(53) Kobayashi, M.; Oh-Oka, H.; Akutsu, S.; Akiyama, M.; Tominaga, K.; Kise, H.; Nishida, F.; Watanabe, T.; Amesz, J.; Koizumi, M.; Ishida, N.; Kano, H., *Photosynth. Res* **2000**, 63, 269-280.

(54) Nuijs, A.M.; Vasmel, H.; Joppe, H.L.P.; Duysens, L.N.M.; Amesz, J., *Biochim. Biophys. Acta**1985**, 807,* 24-34.

(55) Vassiliev, I.R.; Antonkine, M.L.; Golbeck, J.H., *Biochim. Biophys. Acta* **2001**, 1507, 139-160.

(56) Golbeck, J. *Photosyn. Res.* **2007**, *91*, 139-140.

(57) Brok, M.; Vasmel, H.; Horikx, J.T.G.; Hoff, A.J., *FEBS Lett.* **1986**, 194, 322-326.

(58) Kobayashi, M.; van de Meent, E.J.; Erkelens, C.; Amesz, J.; Ikegami, I.; Watanabe, T., *Biochim. Biophys. Acta* **1991***, 1057*, 89-96.

(59) van de Meent, E. J.; Kobayashi, M.; Erkelens, C.; Vanveelen, P. A.; Amesz, J.; Watanabe, T. *Biochim. Biophys. Acta* **1991**, *1058*, 356-362.

(60) Prince, R. C.; Gest, H.; Blankenship, R. E. *Biochim. Biophys. Acta* **1985**, *810*, 377-384.

(61) Kleinherenbrink, F.A.M.; Amesz, J., *Biochim. Biophys. Acta* **1993**, 1143, 77-83.

(62) Watanabe, T.; Kobayashi, M.; Hongu, A.; Nakazato, M.; Hiyama, T.; Murata, N., *FEBS Lett.* **1985,** 191, 252-256.

(63) Zouni, A.; Witt, H.T.; Kern, J.; Fromme, P.; Krauss, N.; Saenger, W.; Orth, P., *Nature* **2001**, 409, 739-743.

(64) Ferreira, K.N.; Iverson, T.M.; Maghlaoui, K.; Barber, J.; Iwata, S., *Science* **2004**, 303, 1831-1838.

(65) Webber, A.N.; Lubitz, W. *Biochim. Biophys. Acta* **2001**, *1507*, 61-79.

(66) Barber, J. *Quart. Rev. Biophys*,**2003**, 36, 71-89.

(67) Witt, H. T. *Photosynth. Res*. **2004**, 80, 85-107.

Chapter 2

Whole-cell NMR characterization of two photochemically active states of the photosynthetic reaction center in heliobacteria

---

2.1 *Abstract*

The photo-CIDNP (photochemically induced dynamic nuclear polarization) MAS (magic-angle spinning) NMR studies of light-induced spin-correlated radical pairs in whole cells of *Heliobacillus mobilis* demonstrate that heliobacterial reaction centers (RCs) are operational in two different states. A culture maintained anaerobically is called Braunstoff (German for brown substance). After exposure to oxygen, Braunstoff is converted to Grünstoff (green substance) as indicated by a color change due to the conversion of BChl *g* to Chl *a*. It is shown that electron transfer occurs symmetrically via both branches of cofactors in both forms. The donor and acceptor cofactors remain identical and unchanged upon conversion while the intermediate accessory cofactors are transformed from BChl *g* to Chl a_F. The donor triplet state in Braunstoff is localized on the special pair donor and lives for 100 μs, demonstrating the presence of a long lived donor triplet state which is not quenched, *e.g.*, by nearby carotenoids. In Grünstoff, the donor triplet becomes mobile and appears to be formed on an accessory cofactor.

This chapter is published in *Biochemistry* 51, 5763-5773 (2012).

2.2 *Introduction*

Heliobacillus (Hb.) mobilis is a strictly anaerobic, nitrogen fixing photosynthetic organism found in abundance in rice paddy fields.[1-3] The photosynthetic machinery of *Hb. mobilis* contains antenna pigments and most of the RC cofactors are bound to a single polypeptide dimer in the cytoplasmic membrane. *Hb. mobilis* has a Type I RC similar to PSI in having an iron-sulfur cluster F_X as a bound electron acceptor.[4] Because it is a homodimer and has a simple polypeptide composition, the heliobacterial RC has been proposed as the evolutionary ancestor of PSI.[5,6] The more complex heterodimeric PSI may thus have evolved by a simple gene duplication event.[7] Unlike other photosynthetic bacteria, *Hb. mobilis* contains few complex structures such as intercytoplasmic membranes and it has no chlorosomes.[1,8] Due to its less complex structure, the heliobacterial RCs would represent attractive models for understanding the homodimeric RCs.[3] However, thus far there is very little structural information available for the heliobacterial RC.

The absorption spectrum of anaerobic *Hb. mobilis* cells is shown in Figure 2.1 (solid line). The color appears brownish green and it is therefore called here Braunstoff. A unique pigment, bacteriochlorophyll *g* (BChl *g*, see Figure 2.2 A), has been identified in these bacteria.[9] BChl *g* acts as antenna pigment and two 13^2 epimers (BChl *g*') act as the primary electron donor special pair ($P798^+$).[10] The primary electron acceptor is 8^1-hydroxy chlorophyll a_F (8^1-OH Chl a_F, Figure. 2.2 B).[11,] The intense absorbance peaks at 570 nm and 798 nm correspond to BChl *g*. The less intense peak at 670 nm corresponds to 8^1-OH Chl a_F.[11,12] Both isolated RCs and membranes have been studied by FT-IR,[13] EPR techniques,[14] and photo-CIDNP MAS NMR[15].

A peculiarity of BChl *g* is the photoconversion at pyrrole ring II when exposed to oxygen in the presence of light. The color change from brownish green to emerald green is observed during this process[3] and leads to a product called Grünstoff here. The pigment becomes spectroscopically equivalent to Chl a_F, which is present in cyanobacteria and green plants.[3] The absorption spectrum of *Hb.*

mobilis after this process is shown in Figure 2.1 (dotted line). All absorbance peaks of BChl *g* pigments decrease upon the conversion. The small remaining peak at 798 nm indicates that the conversion is almost complete. The peak at 670 nm, indicating Chl a_F, becomes more intense. There is not much information available

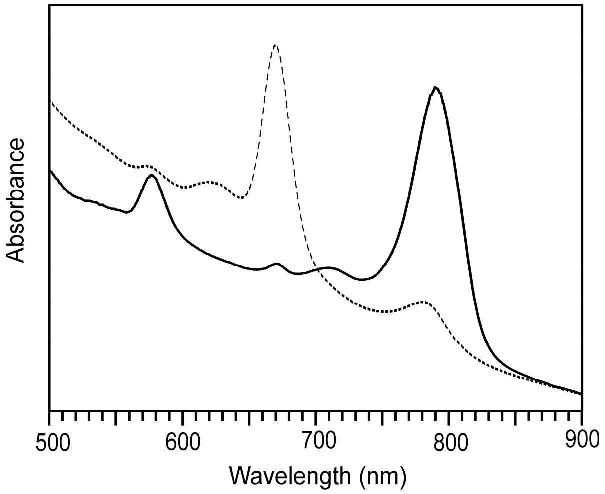

Figure 2.1: Absorption spectra of heliobacterial cells in the anaerobic (Braunstoff, solid line) and aerobic (Grünstoff, dashed line) states. The absorbance is presented in arbitrary units.

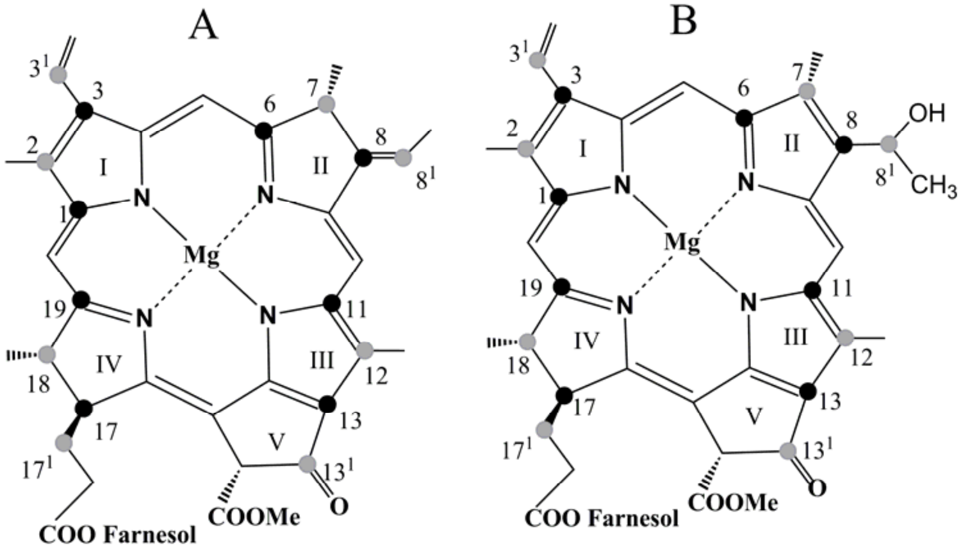

Figure 2.2: BChl *g* (A) and 8^1-OH BChl a_F (B) with label patterns obtained by feeding 4-ALA (black) or 3-ALA (gray). The double bond and metal coordination pattern represents the predominant resonance structure for the bacteriochlorin (A) and the chlorin (B), and follows the corresponding pheophorbides, with >N- pyrrole type nitrogens in rings I and III, and ≥N| pyridine type nitrogens in rings II and IV.

about Grünstoff other than its absorption spectrum.[3] The present work demonstrates that in heliobacterial RCs under aerobic conditions, radical pairs are also formed in Grünstoff by light-induced electron transfer. Here, both Braunstoff and Grünstoff are studied by ^{13}C and ^{15}N photo-CIDNP MAS NMR directly at the cellular level.

The solid-state photo-CIDNP effect, discovered in 1994 by Zysmilich and McDermott[16] has been observed in all natural RCs studied and the effect may well be an intrinsic property of light-induced electron transfer in photosynthesis.[17] In this effect, non-Boltzmann nuclear spin polarization is detected as strongly enhanced ^{13}C or ^{15}N MAS NMR signals.[18] Nuclear spin polarization is established

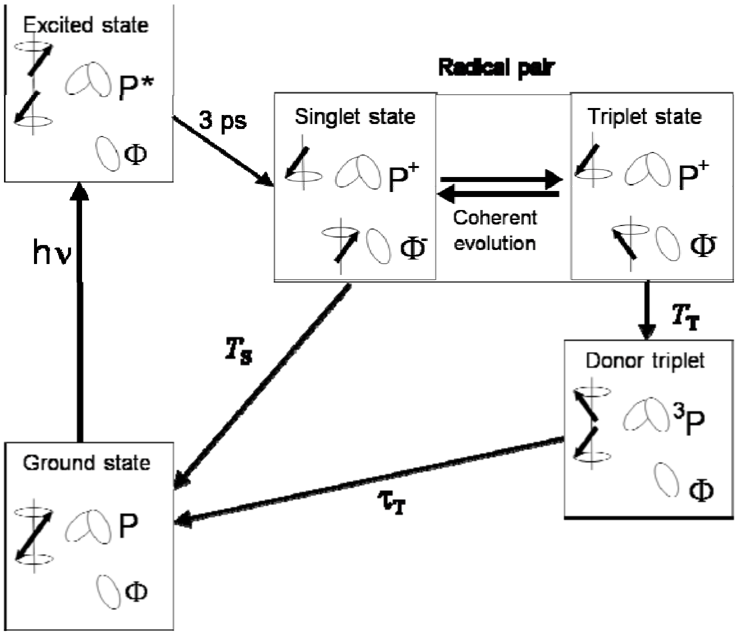

Scheme 2.1: Photocycle in quinone-depleted RCs of *Rb. sphaeroides* WT and R26. Upon illumination and fast electron transfer from an excited singlet state, a radical pair is formed in a pure singlet state having high electron spin order. The radical pair is formed by a radical cation at the two donor BChls (Special pair, P) and a radical anion on the BPhe acceptor cofactor (Φ) of the active branch. The chemical fate of the radical pair depends on its electronic spin state: the singlet state is allowed to recombine with the lifetime of $T_S = 20$ ns and this recombination pathway is termed singlet channel. For the triplet state a direct recombination is spin-forbidden and a donor triplet (^{3}P) is formed with a lifetime of $T_T = 1$ ns. The lifetime of the donor triplet state ($τ_T$) is 100 ns for WT RCs and 100 μs for R26 RCs. The recombination pathway of the donor triplet to the ground state is termed triplet channel. Mechanisms building up photo-CIDNP under steady-state conditions are TSM, DD and DR. Transient nuclear polarization is observed in time-resolved experiments and includes a contribution from the RPM.

by symmetry breaking of the correlated radical pair state via the hyperfine interaction.[19] At the high magnetic fields as applied in an NMR experiment, it is explained by one or more of three parallel mechanisms that can occur in the solid state with continuous illumination:[20-22] three spin mixing (TSM),[23] differential decay (DD)[24] and differential relaxation (DR).[25]

These mechanisms are well understood in photo-CIDNP MAS NMR studies of the quinone-depleted RCs of *Rb. sphaeroides* and in theoretical simulations based on these experiments.[19,22] Scheme 2.1 shows the spin chemical cycle processes that lead to strong nuclear polarization in RCs of *Rb. sphaeroides* WT and its carotenoid less mutant R26. By illumination with white light, the primary electron donor, which is a special pair of BChl *a* molecules, is excited and forms a radical cation by donating an electron to the primary electron acceptor Φ, BPhe *a*. This leads to the formation of a spin-correlated radical pair, initially in its singlet state (S), which is not an eigenstate and converts to the triplet state (T_0) and back by coherent evolution. The high electron spin order of the initial pure electronic singlet state is transferred to a net nuclear polarization by two parallel and competing mechanisms termed TSM[23] and DD.[24] The TSM mechanism is explained by the combined action of electron-electron dipolar coupling or exchange coupling and the pseudosecular hyperfine coupling (hfc) $B = (A_{zx}^2 + A_{zy}^2)^{1/2}$, which breaks the antisymmetry of $<I_z>$ nuclear spin population in coherent spin evolution of the spin correlated radical pair. [23] Due to different lifetimes of the S and of the T_0 states, antisymmetry of the nuclear spin population in the spin correlated radical pair can be broken by a buildup of net nuclear polarization via the *B* in a DD mechanism. The polarization transfer by the DD mechanism occurs due to a single matching condition of $2|\omega_I| = |A_{zz}|$, and the difference of singlet and triplet radical pair lifetimes must be of the order of the inverse hyperfine splitting, *i.e.* $|T_T^{-1}-T_S^{-1}| \sim [(\omega_I+A/2)^2+B^2/4)]^{1/2} - [(\omega_I-A/2)^2+B^2/4)]^{1/2}$. The electron Zeeman interaction drives nuclear-spin independent interconversion between the singlet and triplet state of the radical pair, thus not affecting nuclear spin populations. This remains true even in the presence of *B*, since this coupling is too small to mix different electron spin states. Only if electron spin states are mixed by electron-electron coupling (*d*), as in the TSM mechanism, mixing of nuclear spin states by *B* will also be affected by an electron spin state mixing. If the singlet and triplet state of the radical pair have different lifetimes, as in the DD mechanism, pairs in these two states will experience hyperfine evolution for a different time, which also breaks the antisymmetry of the nuclear spin populations. For B=0 the contribution of the nuclear Zeeman interaction (ω_I) to spin evolution is independent of the electron spin state and will thus not lead to any polarization transfer. For $B\neq0$ the ratio $|\omega_I/A_{zz}|$ determines the extent of mixing of the nuclear spin states, and thus also the extent to which population antisymmetry is violated. Maximum mixing occurs if the ratio is one. The emissive signals of the photo-CIDNP MAS NMR spectrum of WT RCs are due to the predominance of the TSM mechanism over the DD mechanism, and the contribution of the DD to emissive/absorptive patterns depends on the Δg for the two electron spins involved, which is negative for BChl and BPheo.[19] The relative intensity of these emissive photo-CIDNP MAS NMR signals provides information about the spin density distribution of the radical pair in RCs.[20] In the carotenoid-less mutant R26 of *Rb. sphaeroides,* RCs that have a long lived donor triplet, polarization transfer by a DR mechanism occurs in addition.[21,25] This is a modified RPM and depends on the different nuclear longitudinal relaxation rates.[19,26,27]

While electron polarization does not build up during subsequent photocycles, the long ^{13}C longitudinal nuclear relaxation time (T_1)[18] allows for the accumulation of nuclear polarization in a photo-CIDNP MAS NMR experiment. During subsequent photocycles, the electron spin order is transferred to nuclear polarization and during the ^{13}C T_1 time, this nuclear polarization can be accumulated in a steady-state photo-CIDNP experiment since the ^{13}C T_1 is longer than the time constant for nuclear polarization build up. The CIDNP effect can be invoked without quinone depletion by providing high light that reduces the secondary acceptor and blocks the transfer of electrons along the photosynthetic conversion chain. It has been shown to allow for a signal enhancement of more than 10000 relative to the signal in the dark, and hence for the detection of cofactors directly in whole cells.[21,28] Recently, it has been demonstrated that the effect is not limited to frozen natural photosynthetic RCs at NMR fields, but it also occurs in a blue-light photoreceptor (see chapter 4), in liquid membranes,[29] and is predicted to occur at earth's field.[30] Since the effect relies on hyperfine interactions, it requires a radical pair lifetime of at least some tens of nanoseconds. Hence, any observation of the effect implies that light-induced radical pairs with a lifetime significantly longer than ten nanoseconds are generated in a sample.

In time-resolved experiments, the RPM, TSM, DD and DR mechanisms can lead to transient nuclear polarization.[31] In particular for R26 samples, the electronic ground state can be formed from the radical pair in its singlet state on a time scale $T_s = 20$ ns, while for the triplet state of the radical pair the decay to the ground state takes much longer, $\tau = 100$ μs (Scheme 2.1). Since the nuclear hyperpolarization on this triplet pathway is partially extinguished by longitudinal relaxation, the nuclear polarization from the singlet pathway is observed selectively. This enables the observation of transient nuclear polarization selectively from the singlet state during the lifetime of the donor triplet.[22]

The work in this chapter builds upon and extends the initial studies of Roy *et al.* on the photo-CIDNP effect in heliobacteria (Braunstoff) on the membrane level.[15] Due to the presence of a long-lived donor triplet, a strong contribution of DR mechanism to the photo-CIDNP effect in Braunstoff was observed. In this chapter, the previous work is extended to a detailed analysis of Braunstoff at the cellular level and the photoconversion of heliobacterial cells to Grünstoff is described. In addition, a detailed study of both forms of heliobacteria using different isotope label incorporation and by time-resolved photo-CIDNP MAS NMR experiments is performed. This resolves the contribution of different mechanisms for the photo-CIDNP effect in both Braunstoff and Grünstoff and provides a concept about the functional mechanisms and the changes in the RC induced by the photoconversion.

2.3 *Materials and Methods*

2.3.1 *Sample Preparation*

Cells of *Hb. mobilis* strain ATCC 43427 (DSMZ 6151) were used in this study. The cells were cultured in medium no. 1552[32] anaerobically at 37ºC with continuous light. After seven days of growth, cells were harvested by centrifugation (4000 rpm). One half of the harvested cells were uniformly suspended in deoxygenated 20 mM Tris HCl buffer (pH = 8) containing 10 mM sodium ascorbate. In a dry nitrogen gas flow, the Braunstoff sample was reduced with 50 mM sodium dithionite and packed in a 4-mm sapphire rotor for MAS NMR experiments. The other half of the harvested cells was used for preparing Grünstoff. These cells were washed with the medium no.1552 that does not contain sodium ascorbate. The cells were resuspended in the same non-ascorbate medium and were bubbled with oxygen gas under illumination. The conversion to Grünstoff was monitored by taking absorption spectra every 15 minutes. After 3 hours, the conversion to Grünstoff was almost complete and the cells were collected by centrifugation. The cells were resuspended in 20 mM Tris HCl buffer (pH = 8) containing 10 mM sodium ascorbate and reduced with 50 mM sodium dithionite under a nitrogen gas flow. The Grünstoff sample was packed in a 4 mm sapphire rotor for the MAS NMR experiments.

Since NH_4^+ ions appear to be the nitrogen source for the chlorophylls in *Hb. mobilis* cells,[8] $^{15}NH_4Cl$ was used as the precursor for ^{15}N labeling. The *Hb. mobilis* cells were grown anaerobically in medium no. 1552, which contained 46 mM $^{15}NH_4Cl$. The conversion to Grünstoff and the preparation of Braunstoff and Grünstoff samples for ^{15}N MAS NMR experiments was carried out as described above. For selective ^{13}C isotope labeling of BChls and Chls,[33] *Hb. mobilis* cells were grown anaerobically in medium no.1552 containing 1 mM [4-^{13}C]-δ-aminolevulinic acid (ALA) or 3-^{13}C ALA. The carbon atoms C-1, C-3, C-6, C-8, C-11, C-13, C-17 and C-19 of the two BChl species (Figure 2.2, black labels) are selectively isotope labeled by 4-^{13}C ALA incorporation. The 3-^{13}C ALA incorporation produces selective ^{13}C isotope labeling of C-2, C-3^1, C-7, C-8^1, C-12, C-13^1, C-17^1, C-18 carbon atoms of the BChls (Figure 2.2, gray labels). The conversion of Braunstoff to Grünstoff was carried out for both 4-^{13}C ALA and 3-^{13}C-ALA labeled *Hb. mobilis* cells as described above. The 4- and 3-^{13}C ALA labeled Braunstoff and Grünstoff samples were reduced by 50 mM sodium dithionite and packed in 4 mm sapphire rotors for ^{13}C MAS NMR measurements.

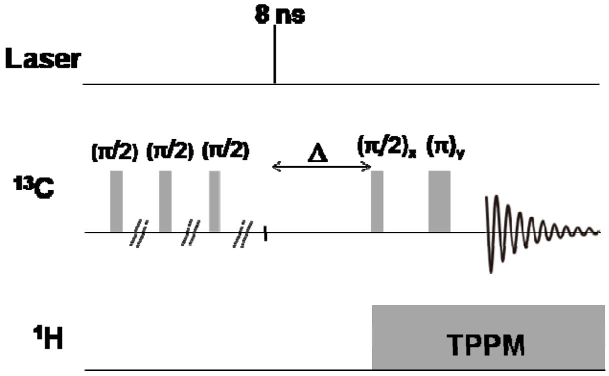

Figure 2.3: Pulse program for time-resolved photo-CIDNP MAS NMR experiments. The delay time Δ is the time difference between the nanosecond laser pulse and the NMR pulse.

2.3.2 *MAS-NMR Measurements*

^{13}C and ^{15}N MAS NMR experiments of *Hb. mobilis* cells were measured with a DMX-200 MHz spectrometer equipped with a 4-mm MAS probe (Bruker, Karlsruhe, Germany). The sample was packed into an optically transparent 4-mm MAS sapphire rotor and inserted into the MAS probe. A very low spinning frequency of 500 Hz was applied during freezing to achieve a homogeneous distribution of sample against the rotor wall.[34] The spinning frequency was increased to 8 kHz after the sample was completely frozen at 235 K.

For continuous illumination photo-CIDNP MAS NMR experiments, white light from a 1000 W xenon lamp was used. Both dark and photo-CIDNP spectra were obtained with a simple Hahn echo pulse sequence[35,36] with TPPM proton decoupling.[37] Laser flashes with pulse lengths of 6-8 ns and energy of 20 mJ were used for time resolved photo-CIDNP MAS experiments. The 532 nm laser flashes were produced using a Nd:YAG laser (SpectraPhysics Quanta-Ray INDI 40-10, Irvine CA, USA). The Hahn echo pulse sequence with TPPM proton decoupling was used for the time resolved photo-CIDNP MAS NMR experiments (Figure 2.3). Additional ^{13}C presaturation pulses were also used prior to a new scan to scramble the remaining ^{13}C coherence and polarization.[31] The nanosecond laser flash was synchronized with the π/2 pulse at the start of the Hahn-echo pulse sequence using an external 500 MHz oscilloscope. The delay time Δ is the time difference between the nano-second laser flash and the π/2 NMR pulse.

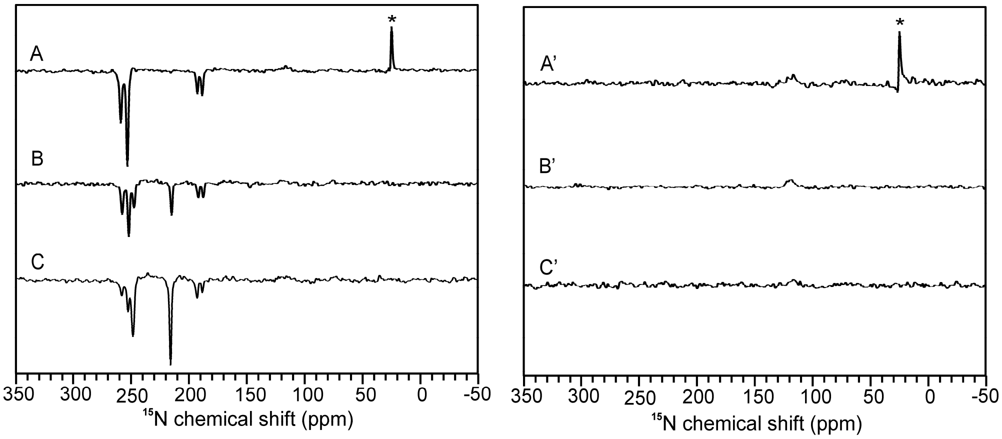

Figure 2.4: ^{15}N MAS NMR spectra of anaerobically (Braunstoff) (A, A'), half-converted (anaerobic/aerobic) (B, B'), aerobically treated (Grünstoff) (C, C') uniformly ^{15}N labeled cells of *Hb. mobilis* cells obtained by illumination with continuous white light (left side) and the data collected in the dark (right side). The spectra have been obtained in a magnetic field of 4.7 T and at a temperature of 235 K. The asterisk on the signal at 23 ppm indicates remaining$^{15}NH_4^+$ ions in the sample.

In the NMR experiments, a recycle delay of 2s was applied. ^{13}C MAS NMR signals of cells with ^{13}C in natural abundance and ^{13}C-ALA labeled *Hb. mobilis* cells were collected for 40 h, and 12 h respectively. ^{13}C time resolved experiments were carried out for 9 h in 3-^{13}C ALA labeled *Hb. mobilis* cells. Both dark and light ^{13}C MAS NMR spectra were referenced to the ^{13}COOH chemical shift of solid tyrosine•HCl at 172.1 ppm and artificial line broadening of 50 Hz was applied prior to Fourier transformation. All ^{15}N MAS NMR spectra were collected for 40 h. Chemical shifts are given relative to the $^{15}NH_3$ resonance frequency, using the response of solid $^{15}NH_4NO_3$ at $\delta = 23.5$ ppm as a reference. For ^{15}N MAS NMR spectra, artificial line broadening of 20 Hz was applied prior to Fourier transformation. ^{13}C and ^{15}N photo-CIDNP MAS NMR spectra were normalized with the most intense signal in each spectrum.

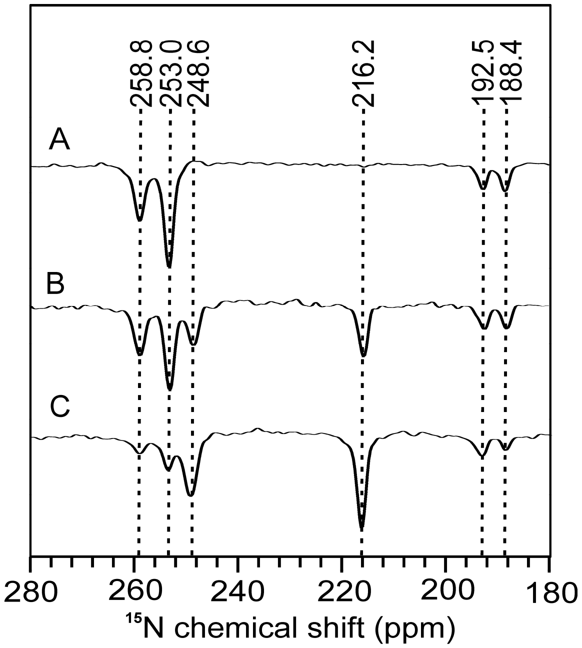

Figure 2.5: Expanded view of ^{15}N photo-CIDNP MAS NMR spectra of anaerobically (Braunstoff) (A), half-converted (anaerobic/aerobic) (B), aerobically treated (Grünstoff) (C) uniformly ^{15}N labeled cells of *Hb. mobilis* cells, obtained by illumination with continuous white light.

2.4 *Results*

2.4.1 *^{15}N photo-CIDNP MAS NMR experiments*

The present work demonstrates that the solid-state photo-CIDNP effect is observable by ^{15}N MAS NMR in whole cells of both forms of uniformly ^{15}N labeled *Hb. mobilis* (Figure 2.4 and Figure 2.5). Since the build-up of photo-CIDNP requires radical pair lifetimes of at least some tens of nanoseconds (Fig 2.1), the occurrence of the effect demonstrates that this condition is fulfilled in both forms, Braunstoff and Grünstoff. In addition to the spectra of the two forms of *Hb. mobilis* cells, the spectrum of a half-converted sample is also shown (Spectra B and B' in Figure 2.4). The respective ^{15}N MAS NMR spectra (A', B' and C') measured in the dark are shown in the right panel of Figure 2.4. In ^{15}N MAS spectra collected in the dark, only signals from the protein backbone are visible, while light induced signals appear in the ^{15}N photo-CIDNP MAS NMR spectra. These light-induced ^{15}N MAS NMR signals of *Hb. mobilis* cells show emissive signs reminiscent of ^{15}N labeled RCs of *Rb. sphaeroides* [16,40] and of PSII.[38] In Figure 2.4, both ^{15}N MAS

NMR spectra collected in the dark (A') and with light (A) show a narrow signal at 23.5 ppm due to the presence of free NH_4^+ ions. During conversion of *Hb. mobilis* cells to Grünstoff, the cells were resuspended in a medium that does not contain $^{15}NH_4Cl$. Therefore, the signal at 23.5 ppm is absent in spectra (B, B') and (C, C').

Figure 2.5 shows an expanded view of the ^{15}N photo-CIDNP MAS NMR spectra in Braunstoff (A) as well as of half converted (B) and in Grünstoff (C) *Hb. mobilis* cells. In spectrum A, four signals appear, with chemical shifts of 188.4, 192.5, 253.0 and 258.8 ppm. ^{15}N photo-CIDNP MAS NMR provides less complex data compared to ^{13}C, allowing for a more straightforward analysis.[38,39] A tentative assignment (Table 2.1) of these signals was performed by comparison to similar data collected from Chl *a* in PSI and PSII[38] and BChl *a* of *Rb. sphaeroides* R26.[16,39] In BChl *g*, pyrrole ring II is different from that of Chl *a* and similar to that of BChl *a*. The data confirm that all ^{15}N light-induced MAS NMR signals in the spectrum of Braunstoff are due to the four nitrogen atoms of BChl *g*' of the donor while the signals from the putative acceptor 8^1-OH Chl a_F are not observed[15]. For ^{15}N NMR data, the distinction between pyrrole and pyridine nitrogens is straightforward, as is the recognition of a chlorin-type response. However, a full assignment of N-I, N-II, N-III and N-IV is not straightforward, only the ^{15}N-II for the chlorin is clear. The ^{15}N chemical shifts at 188.4 ppm, 258.8 ppm, 192.5 ppm and 253.0 ppm are thus tentatively assigned to the N-I, N-II, N-III and N-IV nitrogen atoms of BChl *g*', respectively. The primary donor in *Hb. mobilis* RCs was proposed to be a homodimer of BChl *g*' molecules.[10] The heterodimeric donor of PSI show broadening and splitting of ^{15}N signals in its spectra,[38] and a pronounced splitting of photo-CIDNP signals was observed in the case of chemically identical cofactors of the special pair of *Rb. sphaeroides*[20]. Thus it is possible that two cofactors give rise to the same response by lack of both static and dynamic heterogeneity, or that dynamic heterogeneity leads to a single response of one of the two cofactors depending on the trajectory along collective vibrational modes of the two BChl *g*' comprising the homodimeric donor.[41]

In spectrum (B), in addition to four signals from BChl *g*', two signals with chemical shifts of 216.2 and 248.6 ppm appear and the intensities of the signals at 253.0 and 258.8 ppm decrease. The signals at 216.2 and 248.6 ppm can be

Assignment	Chl a^*		BChl a^+	BChl g	8^1-OH Chl *a*
Atom	PS-I σ_{solid}	PS-II σ_{solid}	σ_{solid}	σ_{solid}	σ_{solid}
N-I	186.2 (e)		187.2	188.4	188.4
	190.9 (a)		189.3		
N-II	206.1 (a)	211.5 (e)	261.2	258.8	216.2
	211.5 (e)		251.0		
N-III	193.2 (a)	195.3 (e)	197.4	192.5	192.5
			191.9		
N-IV	233.3 (a)	247.6 (e)	255.9	253.0	248.6
	250.3 (e)		258.8		
	254.9 (e)				

Table 2.1: Tentative assignments of ^{15}N photo-CIDNP MAS NMR signals. Chemical shifts are referenced to liquid ammonia with use of an external standard of solid $^{15}NH_4NO_3$ ($\delta = 23.5$).

*^{15}N-photo-CIDNP MAS NMR data collected from PSI and PSII, where the emissive signals (e) are from the donor and the absorptive signals (a) from the acceptor Chl (38).

+^{15}N-photo-CIDNP MAS NMR on R26 (39).

attributed to the N-II and N-IV nitrogen atoms of the primary electron acceptor 8^1-OH Chl a_F (Table 2.1). In spectrum (C), the signals at 216.2 and 248.6 ppm (N-II and N-IV of 8^1-OH Chl a_F) are stronger than the signals at 253 and 258.8 ppm (N-II and N-IV of BChl *g*'), which decrease further in intensity relative to the data in Figure 2.5B. The two ^{15}N NMR signals at 188.4 and 192.5 ppm (N-I and N-III) remain unchanged during the conversion, implying that the chemical shifts are similar in both BChl *g*' and 8^1-OH Chl a_F cofactors.

For the Braunstoff, a long donor triplet lifetime τ leads to a predominant contribution of the DR mechanism to the photo-CIDNP effect.[15] The DR mechanism operates mainly on donor cofactors, with very little contribution from the acceptor.[21] In contrast, for the data collected from the Grünstoff, the observation of acceptor signals in addition to the donor signals indicates changes of the electron-electron coupling upon photoconversion. Since emissive signals are generally attributed to TSM (Fig 2.1), the acceptor signals can be explained by the increase of the contribution from the TSM mechanism relative to the DD contribution. The mixed sample (Spectrum B) does not show any additional signal that would not belong to Braunstoff or Grünstoff. This suggests that the transformation does not lead to metastable asymmetric intermediate states in which one half of the RC is transformed and the other not.

It appears that the chemical constitution of the donor remains unchanged. Hence the color change is not caused by a change in the donor cofactors. Since also the acceptor signals in Grünstoff are not split, it appears that the strongly symmetric character remains intact upon transformation.

Assuming that the photo-CIDNP intensities of steady-state experiments correlate with electron spin densities in *p*-orbitals,[38] a similarity to PSII is observed in Braunstoff , with the highest electron spin density on a pyridine-type nitrogen, probably the N-IV.[38] On the other hand, the highest electron spin density of Grünstoff is observed on the N-II nitrogen atoms, and this is similar to PSI.[38].

2.4.2 *^{13}C photo-CIDNP MAS NMR on natural abundance samples*

The next step is to demonstrate that the solid-state photo-CIDNP effect can be observed in both natural abundance (n.a.) Braunstoff and Grünstoff *Hb. mobilis* cells by ^{13}C MAS NMR. In spectra A and C of Figure 2.6, the samples are measured in the dark and only weak and broad features from the protein are visible. Spectra B and D are the ^{13}C photo-CIDNP spectra of Braunstoff and Grünstoff, respectively, obtained with continuous illumination. Several light induced signals are observed in the region between 200 and 80 ppm. The ^{13}C photo-CIDNP spectrum of Braunstoff shows emissive (negative) and absorptive (positive) light-induced signals, comparable to those of RCs from *Rb. sphaeroides* R26[21] and PSII.[42] The long-lived donor triplet state (^{3}P) favors a strong contribution from the DR mechanism to the photo-CIDNP effect, which matches the ^{15}N data in Fig 2.5 and validates the early photo-CIDNP studies that were performed on *Hb. mobilis.*[15] The strong contribution from the DR mechanism indicates that the cofactor arrangement in Braunstoff may be similar to the pigment orientation in R26 RCs.

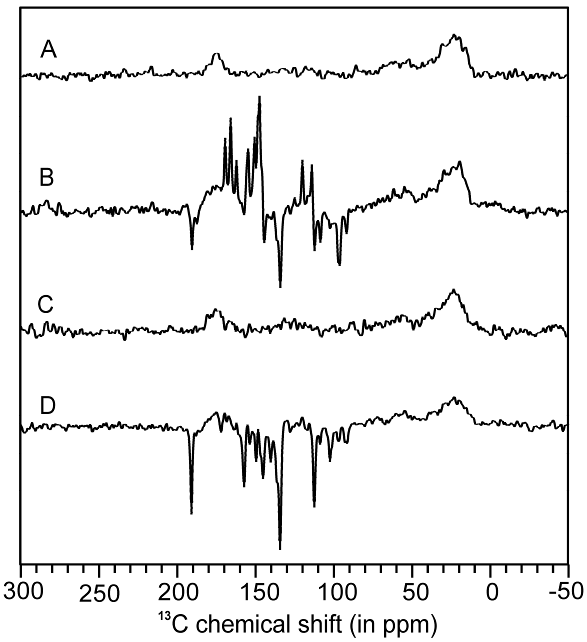

Figure 2.6: ^{13}C MAS NMR spectra of anaerobically (Braunstoff) and aerobically (Grünstoff) treated cells of *Hb. mobilis* obtained by illumination with continuous white light (B and D) and the data collected in the dark (A and C).

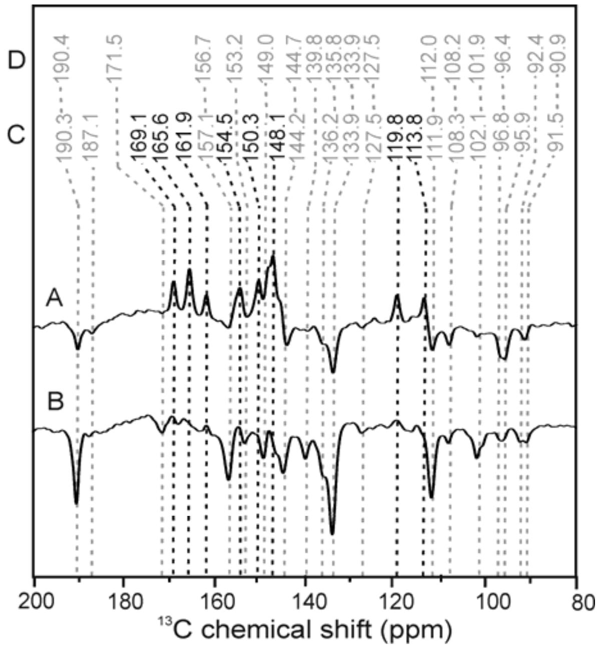

Figure 2.7: Aromatic part of the ^{13}C photo-CIDNP MAS NMR spectra of anaerobically (Braunstoff) (A) and aerobically (Grünstoff) (B) treated cells of *Hb. mobilis.* Lower row of chemical shifts C belong to Braunstoff and the assignments in the upper row D belong to Grünstoff. Black dashed lines point to the absorptive peaks and gray dashed lines indicate emissive peaks.

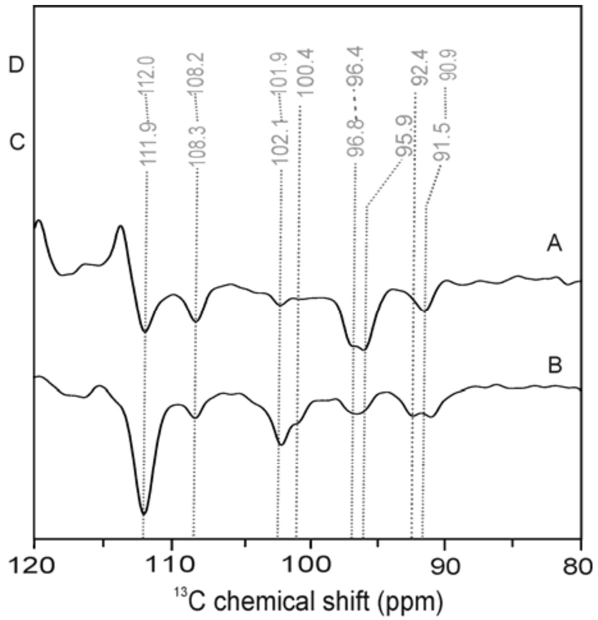

Figure 2.8: The methine region of ^{13}C photo-CIDNP MAS NMR spectra of anaerobically (Braunstoff) (A) and aerobically (Grünstoff) (B) treated cells of *Hb. mobilis.* Chemical shifts in the lower row C belong to Braunstoff and the assignments in the upper row D belong to Grünstoff.

The emissive signals cannot be explained by the DR mechanism.[19] These are attributed to a contribution from the TSM mechanism that is strong relative to the DD mechanism and involves the acceptor. Upon conversion, all the photo-CIDNP signals contribute to the emissive pattern that marks the TSM mechanism, even though the chemical shifts of the signals are almost the same as for the signals in Braunstoff (Figure 2.7).

Figure 2.7 shows an expanded view of the aromatic region of the ^{13}C photo-CIDNP MAS NMR spectra of n.a. Braunstoff and Grünstoff cells. The chemical shifts from Braunstoff (lower row of values C) and Grünstoff (upper row of values D) are compared with the chemical shifts of Chl *a* and BChl *a* obtained from other photo-CIDNP studies in Table 2.2. Apparently the interaction between the cofactors is modified, leading to different activities of the three competing mechanisms. In Grünstoff, the emissive character of the signals can be explained by decay through the singlet channel with T_S = 20 ns, which leads to an enhanced contribution of TSM mechanism[23] over the DR mechanism, for instance due to a change in electron-electron coupling. The negative signal at 190.3 ppm can be

Carbon No.	Chl *a* [a]	BChl *a* [b]	*Hb. mobilis* (Braunstoff)[c]	*Hb. mobilis* (Grünstoff)[c]
13^1	190.6	188.2	190.3(E)^2	190.1(E)^2
17^3	175.3	174.0		
13^3	171.2	171.4		
19	170.2	168.9	165.6(A)^1	165.6(A)^1
14	162.0	160.7	161.1(A)^3	
1	155.9	153.5	154.5(A)^1	154.5(A)^1, 156.7(E)^1
6	154.4	170.2	169.1(A)^1	169.1(A)^1 171.5(E)^1
16	154.0	150.1	150.3(A)^3	153.2(E)^3
4	150.7	152.2	148.1(A)^3	153.2(E)^3
11	147.2	147.2	145.8(A)^1	145.8(A)^1
9	147.2	158.0	150.2(A)^3	149.0(E)^3
8	146.2			144.7(E)^1
8^1			64.3(E)^2	64.3(E)^2
3	137.0	136.1		139.8(E)^1
2	136.1	140.1	133.9(E)^2	133.9(E)^2
12	134.0	119.9	119.8(A)^2	119.8(A)^2
7	133.4		43.5(A)^2	43.5(A)^2
13	126.2	124.1	127.5(E)^1	127.5(E)^1
3^1	126.2	194.5	113.8(A)^2	113.8(A)^2
3^2	113.4		111.9(E)^3	112.0(E)^3
10	108.2	100	108.3(E)^3	108.2(E)^3
15	102.8	105.8	102.1(E)^3	101.9(E)^3, 100.4(E)^3
5	98.1	98.8	96.8(E)^3,95.9(E)^3	96.4(E)^3
20	93.3	93.7	91.5(E)^3	92.4(E)^3, 90.9(E)^3
17	51.4		52.4(A)^1	52.4(A)^1
17^1			29.0(A)^2	
18			47.1(A)^2	

Table 2.2: Preliminary assignments of ^{13}C photo-CIDNP MAS NMR signals in the spectra of Braunstoff and Grünstoff. Labels (A) indicate absorptive and (E) emissive signals, respectively. [a] Ref. 43; [b]Ref 32; [c] this work: The superscripts 1,2,3 in the chemical shifts corresponds to the assignments from 4-ala, 3-ala and unlabelled heliobacterial cells respectively

assigned to the C-13^1 carbonyl carbon atom of the acceptor 8^1-OH Chl a_F. The positive signals at 169.1, 165.6, 161.9, 154.5 150.3, 148.1, 119.8 and 113.8 ppm, which are absent in the spectra of Grünstoff, can be tentatively assigned to carbon atoms C-6, C-19, C-14, C-1, C-16, C-4, C-12 and C-3^1, respectively, of the donor BChl *g*. The negative signals at 171.5, 157.1, 153.2, 149.0, 144.7, 139.8, 133.9 and 112 ppm match well to C-6, C-1, C-16, C-9, C-8, C-3, and C-3^2 carbon atoms of acceptor 8^1-OH Chl a_F. These assignments of BChl *g*' and 8^1-OH Chl a_F are based on the comparison with the data obtained for Chl *a* and Bchl *a* in the RCs of PSI and *Rb. sphaeroides* (see Table 2.2). Hence, the chemical shift patterns show that in Braunstoff all the light induced absorptive signals are due to BChl *g*' (the electron donor) and in both forms the emissive signals are due to 8^1-OH Chl a_F (the electron acceptor).

The signals in the methine region show an emissive pattern in both Braunstoff and Grünstoff (for an expanded view, see Figure 2.8). The signals at 108.3 and 102.1 ppm are attributed to ^{13}C-10 and ^{13}C-15 carbon nuclei of 8^1-OH Chl a_F, respectively. The methine carbon atom C-5 is observed as a doublet (96.8 and 95.9 ppm) in Braunstoff, while in Grünstoff only a single signal (96.4 ppm) occurs. On the other hand, the methine carbon atom C-20 in Grünstoff is split (92.4 and 90.9 ppm) but not in Braunstoff (91.5 ppm). Since in both cases the negative signals originate from the acceptor, we conclude from the splitting that in both forms the two acceptor branches are active, and that the acceptors are slightly distinguishable and are probably the two acceptor 8^1-OH Chl a_F molecules. The activity of both branches of cofactors, as measured by the photo-CIDNP signal intensity pattern, is similar to that found for PSI.[44]

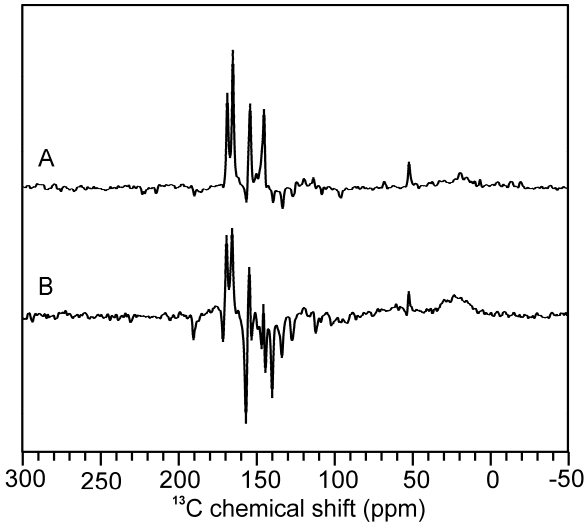

Figure 2.9: ^{13}C photo-CIDNP spectra of 4-ALA *Hb. mobilis* cells, anaerobically (Braunstoff) (A) and aerobically (Grünstoff) (B) treated. The spectra have been obtained by illumination with continuous white light in a magnetic field of 4.7 T and at a temperature of 235 K.

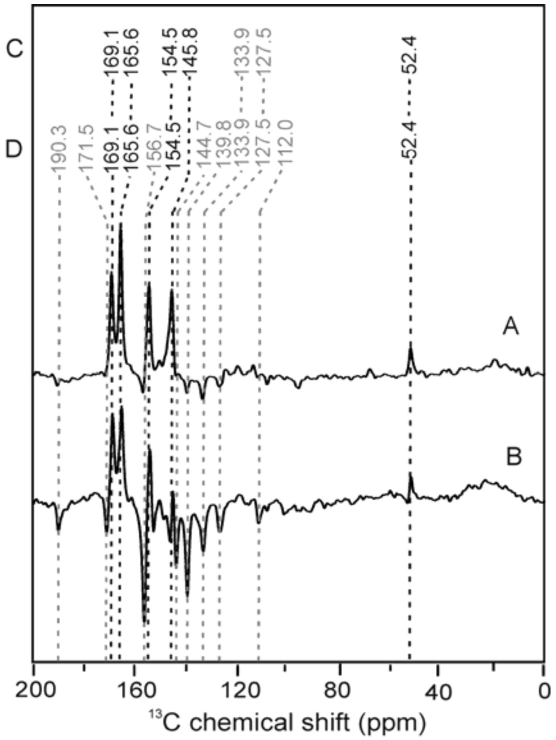

Figure 2.10: Expanded view of the ^{13}C photo-CIDNP MAS NMR spectra of anaerobically (Braunstoff) (A) and aerobically (Grünstoff) (B) treated cells of 4-ALA labelled *Hb. mobilis*. Chemical shifts in the upper row C belong to Braunstoff and the assignments in the lower row D belong to Grünstoff. Black dashed lines indicate the absorptive peaks and gray dashed lines correspond with emissive peaks.

2.4.3 *^{13}C photo-CIDNP MAS NMR on selectively ^{13}C labeled samples.*

Selective enhancement of ^{13}C photo-CIDNP MAS NMR signals by isotope labeling can help in the assignment of the light-induced signals. ^{13}C isotope labeling of the cofactors has been achieved in the RCs of Braunstoff and Grünstoff by biosynthetic incorporation of labels, using selectively labeled ALA as precursor (Figure 2.2). The position of the ^{13}C label in the RC cofactors depends on the position of the ^{13}C label in the precursor ALA. Both 4-^{13}C ALA and 3-^{13}C ALA precursors have been used in this study.

^{13}C photo-CIDNP MAS NMR spectra of 4-^{13}C ALA labeled *Hb. mobilis* cells are shown in Figure 2.9. Spectra A and B originate from Braunstoff and Grünstoff, respectively. Apart from the signals in the aromatic region, one light induced signal is observed in the aliphatic region in both spectra. It originates from C-17 of the donor, which gains signal intensity via ^{13}C-^{13}C spin diffusion from the nearby aromatic carbons of the cofactor.[22] In the spectrum of Braunstoff, only absorptive signals are strongly enhanced. In the spectrum of Grünstoff, both strongly enhanced positive and negative signals are observed. A shift of intensity from negative to positive signals upon isotope labeling is evident and demonstrates that magnetic nuclei actively participate in the spin dynamics. Interestingly, for the 3-ALA labeled sample (Figure 2.11), in which the magnetic isotopes are more distant from the π-system, the shift of intensity is less pronounced. Since isotope labeling modifies the photo-CIDNP intensities, the concentration of isotope label is difficult to extract by comparing signals from labeled and unlabeled positions. However, in 2-dimensional experiments cross-peaks were difficult to detect (data not shown), which indicates a label incorporation below 50%.

The expanded view of the light induced signals from 4-^{13}C ALA labeled *Hb. mobilis* cells in both forms is presented in Figure 2.10. The absorptive light-induced signals with chemical shifts of 165.6, 154.5, 169.1 and 145.8 ppm can be attributed to to C-19, C-1, C-6, and C-11 of the donor BChl *g'* (see black labels in the Figure 2.2 A) in both Braunstoff and Grünstoff (see Table 2.2). The absorptive signal in the aliphatic region at 52.4 ppm belongs to C-17 of BChl *g'* which is the only aliphatic carbon that is ^{13}C labeled when using a 4-^{13}C ALA

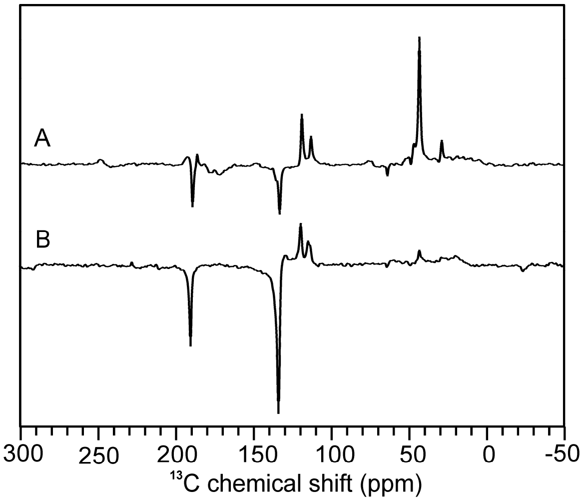

Figure 2.11: ^{13}C photo-CIDNP spectra of 3-ALA *Hb. mobilis* cells, anaerobically (Braunstoff) (A) and aerobically (Grünstoff) (B) treated. The spectra have been obtained by illumination with continuous white light in a magnetic field of 4.7 T and at a temperature of 235 K.

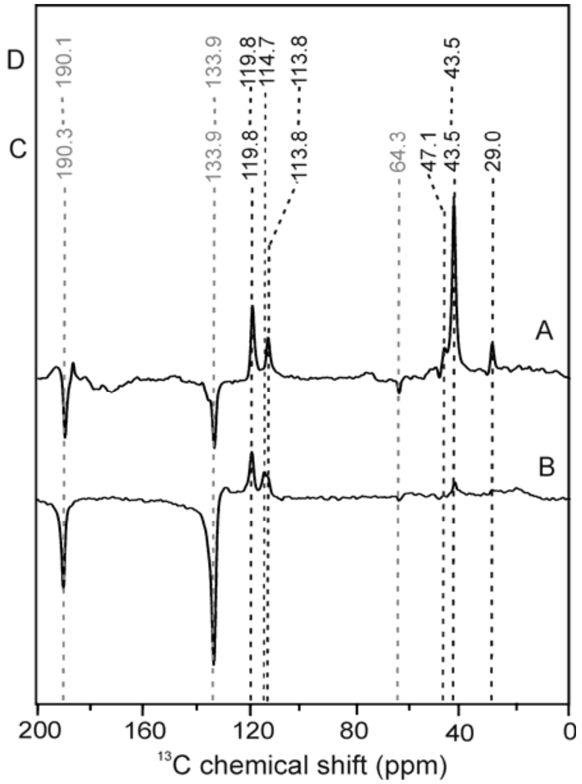

Figure 2.12: Expanded view of the ^{13}C photo-CIDNP MAS NMR spectra of anaerobically (Braunstoff) (A) and aerobically (Grünstoff) (B) treated cells of 3-ALA labeled *Hb. mobilis.* Chemical shifts in the lower row belong to Braunstoff and the assignments in the upper row belong to Grünstoff. Black dashed lines indicate the absorptive peaks and gray dashed lines correspond with emissive signals.

labeled substrate. The emissive light induced signals with chemical shifts of 156.7. 171.5, 144.7, 139.8, and 127.5 ppm can be attributed to the C-1, C-6, C-8, C-3, and C-13 of the primary acceptor 8^1-OH Chl a_F (see black labels in Figure 2.2 B and Table 2.2). Again, it is evident that the donor and acceptor cofactors both give rise to a unique NMR response. Since the chemical shift pattern remains the same in the conversion from Braunstoff to Grünstoff, the functional symmetry and identity of the active cofactors appears not affected by the transition

In the ^{13}C photo-CIDNP MAS NMR spectra of 3-^{13}C ALA labeled *Hb. mobilis* cells (Figure 2.11 and Figure 2.12), the spectrum of Braunstoff (A) shows mixed patterns of absorptive and emissive light induced signals. That the signal intensity of the positive signal in the aliphatic region (43.5 ppm, C-7 of the donor)

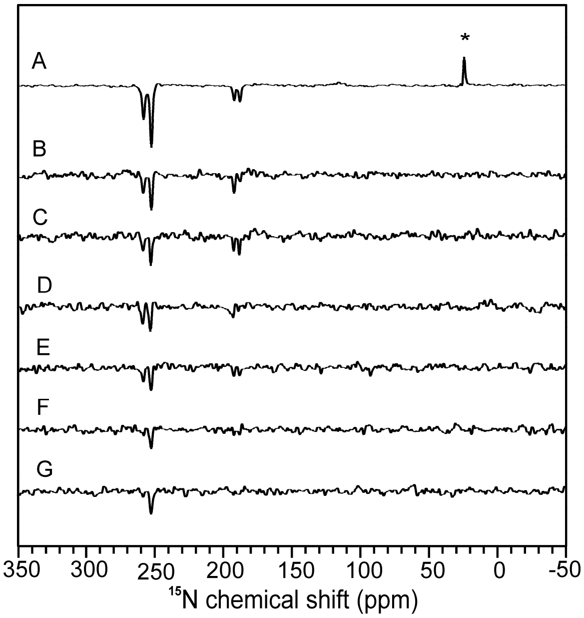

Figure 2.13: Series of time-resolved ^{15}N photo-CIDNP spectra of uniformly ^{15}N labeled *Hb. mobilis* cells, anaerobically treated (Braunstoff). The spectra have been obtained in a magnetic field of 4.7 T and at a temperature of 235 K. The laser pulses have a length of ~10 ns and a wavelength of 532 nm. The delay times between the laser pulse and the start of NMR data acquisition is 0 μs (B), 10 μs (C), 30 μs (D), 50 μs (E), 100 μs (F), 200 μs (G). The spectrum at the top (A), obtained with continuous illumination, is shown for comparison.

is stronger than for labeled aromatic carbons might be due to local dynamics.[45] The positive signals in the aliphatic region are due to carbons C-7, C-17^1 and C-18 of the primary donor BChl *g*' (see gray labels in Figure 2.2 A and Table 2.2). The resolved response at 29.0 ppm originates from C-17^1 of the donor, while the only emissive signal in the aliphatic region occurs at 64.3 ppm and can be tentatively assigned to C-8^1 of the acceptor. The weak negative signals near to the 29 and 47 ppm signals belong to C-17^1 and C-18 of the primary acceptor 8^1-OH Chl a_F (see gray labels in Figure 2.2 B and Table 2.2). Hence, the isotope labeling experiment supports the assignment of the positive signals to the donor cofactor and of the negative signals to the acceptor cofactor.

The absorptive signals at 119.8 and 113.8 ppm in the aromatic region correspond to the C-12 and C-13 carbon atoms of BChl *g*' (Table 2.2). The emissive light-induced signals at 190.3 and 133.9 ppm correspond with the C-13^1 and C-2 carbon atoms of the acceptor 8^1-OH Chl a_F (Table 2.2). These are the most intense signals in the spectrum of Grünstoff. Table 2.2 summarizes the assignments. There is one absorptive signal originating from the C-3^1 carbon atom of the BChl *g*' donor in the spectrum of Grünstoff that appears to be doubled (113.8 and 114.7 ppm). In both spectra, positive and negative signals appear to be very narrow, with almost equal linewidths of ~35 Hz. The observation of very sharp lines from the cofactors seems to be a general feature of RCs,[34,38,42] providing a well defined, homogeneously ordered, dynamically averaged, environment. These features remain intact upon photoconversion to Grünstoff.

2.4.4 *Time-resolved -photo-CIDNP MAS NMR experiments*

Time-resolved photo-CIDNP MAS NMR experiments allow for observation of the evolution of spin dynamics and of the reaction kinetics of the radical pair on a microsecond timescale.[22,32] Here we report time-resolved data obtained from both Braunstoff and Grünstoff by solid-state photo-CIDNP MAS NMR experiments on ^{15}N uniformly labeled as well as on 3-^{13}C ALA labeled *Hb. mobilis* cells using nanosecond laser flashes. The time resolution was obtained by varying the delay time Δ, which is the time difference between the laser pulse and the beginning of the NMR $\pi/2$ detection pulse (see Figure 2.3).

Figure 2.13 shows the photo-CIDNP ^{15}N MAS NMR spectra of *Hb. mobilis* cells (Braunstoff). The top spectrum (A) is the photo-CIDNP MAS NMR response obtained with continuous illumination of white light. The other traces represent the time-resolved photo-CIDNP MAS NMR data obtained by varying the delay time from Δ = 0 μs (B) to Δ = 200 μs (G). In the spectrum with Δ=0 μs (B), four signals with chemical shifts of 188.4, 258.8, 193.1, 253.0 ppm occur, attributed to the N-I, N-II, N-III, N-IV nitrogen atoms of BChl *g*' , respectively. The spectra were collected with a delay time Δ of 10 (C), 30 (D), 50 (E), 100 (F) or 200 μs (G). Compared with the spectrum obtained with continuous illumination, these time-resolved spectra show a lower signal to noise ratio. The intensity of light induced signals decays with an increase in the delay time from 0 μs to 100 μs, especially for the signals at chemical shifts of 188.4 (attributed to N-I) and 193.1 (attributed to N-III) ppm. The light-induced signal at 253 ppm persists at a delay time of 200 μs and

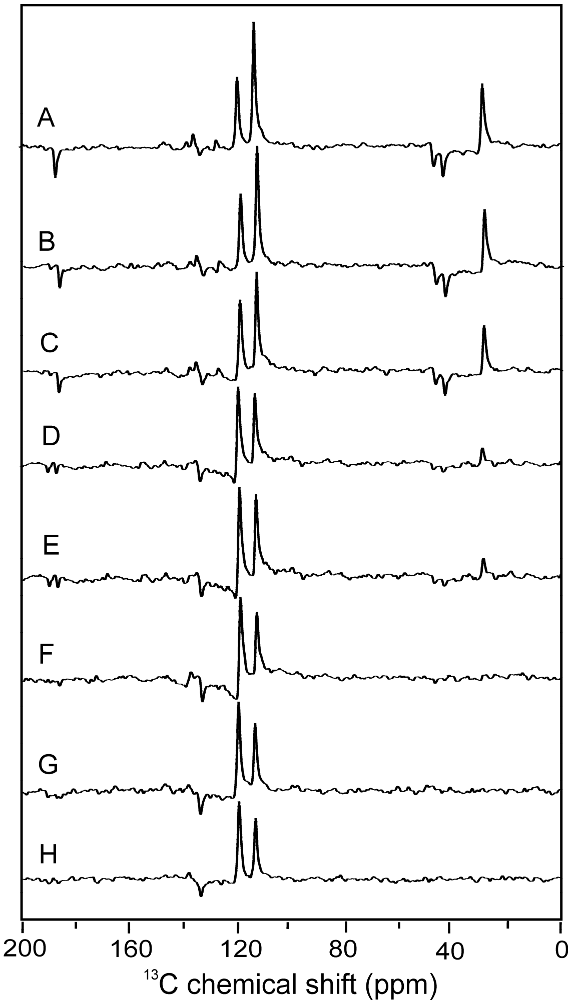

Figure 2.14: Series of time-resolved ^{13}C photo-CIDNP MAS NMR spectra of 3-ALA labeled *Hb. mobilis* cells, anaerobically (Braunstoff) treated. The spectra have been obtained in a magnetic field of 4.7 T and at a temperature of 235 K. The laser pulses have a length of ~10 ns and a wavelength of 532 nm. The delay time between laser pulse and NMR measurement is 0 μs (A), 10 μs (B), 30 μs (C), 50 μs (D), 100 μs (E), 200 μs (F), 500 μs (G) and 1 ms (H).

longer. As shown in Scheme 2.1, the transient signals are due to the RPM polarization of the cofactors that are in the ground state following the rapid decay via the singlet channel with T_s = 20 ns, and are observable until the nuclear spin population of the cofactors that reach the ground state from the triplet leads to the recovery of the Boltzmann equilibrium and quenching of the light-induced enhancement on the time scale of the donor triplet lifetime τ =~100 μs. A very similar pattern of decay of light induced signals with increase of delay time and life time (τ) of donor triplet was observed in time-resolved photo-CIDNP MAS NMR measurements of *Rb. sphaeroides* R26.[39] In the time evolution of Braunstoff, the same kinetics, at a time scale τ =~100 μs, is found in the parallel decay of three signals, while steady state nuclear polarization builds up leading to the dominant signal at 253.0 ppm. This would imply that, similar to *Rb. spheroides* R26, Braunstoff has a long-lived ^{3}P state which is not quenched by nearby carotenoids.

From 3-^{13}C ALA labeled *Hb. mobilis* cells, high-quality time-resolved photo-CIDNP spectra have been obtained. A set of laserflash photo-CIDNP spectra of Braunstoff with different delay time Δ is shown in Figure 2.14. The data collected with a delay time of 0 μs (A) show the light-induced signals almost similar to the steady state photo-CIDNP MAS NMR spectra of 3-^{13}C ALA labeled Braunstoff (see Figure 2.11A), except for the absence of the emissive signal at 133.9 ppm, the occurrence of the signal at 187.0 ppm and for the different phasing of the signals in aliphatic region. The signals in the aliphatic region disappear within about 100 μs, confirming the transient nuclear polarization from cofactors in their ground state in the time window 20ns <Δ<100 μs, *i.e.* between the rapid decay from the singlet state and the slower decay from the triplet state.[22] In the same time interval, also the transient signal of the carbonyl carbon at 187.0 ppm disappears and the emissive signal at 133.9 ppm evolves. After 100 μs, the light-induced signals are due to the steady state photo-CIDNP effect. Hence, the time evolution clearly demonstrates (i) the occurrence of a long-lived ^{3}P donor triplet state in Braunstoff by the observation of transient nuclear polarization associated with the rapidly decaying singlet component of the radical pair that (ii) confirms a triplet lifetime τ = ~100 μs (Scheme 2.1), which (iii) matches the kinetics reported for *Rb. sphaeroides* R26.[22]

Figure 2.15 shows a series of time resolved photo-CIDNP ^{13}C MAS NMR datasets collected from 3-^{13}C ALA labeled cells of Grünstoff. This transient nuclear polarization is similar to that observed in Braunstoff since the transient features disappear on a timescale of 100 μs. The similarity of the spectral features of the transient nuclear polarization as well as the conservation of its decay kinetics, demonstrate that the identity of the cofactors forming the radical pair is not changed upon phototransformation. There is, however, a remarkable difference in the time-evolution of both forms. Unlike the time resolved spectrum of Braunstoff, light-induced signals are observed in the time resolved spectrum of Grünstoff after the initial 10 μs (Figure 2.15). Such a 'silent' initial period has not yet been reported from other RCs. Except for the signal at 133.9 ppm, the signals decay for $\Delta > 100$ μs (data not shown). This demonstrates that Grünstoff has a triplet lifetime $\tau = 100$ μs, similar to the Braunstoff, and for $\Delta < 100$ μs the polarization from the RC fraction subject to recombination via the singlet channel is observed (Scheme 2.1).

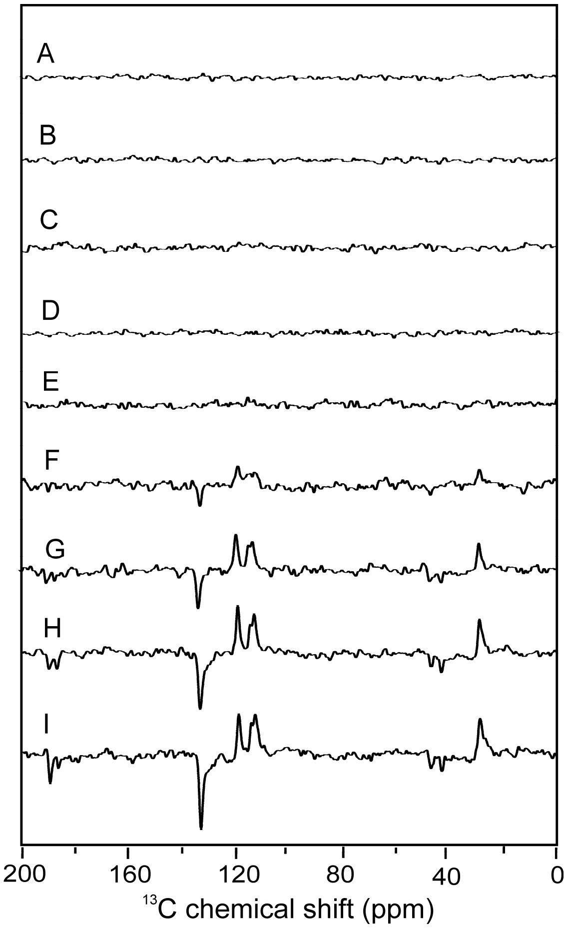

Figure 2.15: Series of time-resolved ^{13}C photo-CIDNP MAS NMR spectra of 3-ala labelled *Hb. mobilis* cells, aerobically (Grünstoff) treated. The spectra have been obtained in a magnetic field of 4.7 T and a temperature of 235 K. The laser pulses have a length of ~10 ns and a wavelength of 532 nm. The delay time between laser pulse and NMR measurement is 0 μs (A), 3 μs (B), 5 μs (C), 7 μs (D), 8 μs (E), 9 μs (F), 10 μs (G), 30 μs (H) and 50 μs (I).

2.5 *Discussion*

2.5.1 *Structure of the primary radical pair in Braunstoff*

The solid state photo-CIDNP data provide converging evidence that the overall radical pair structure and kinetics in *Hb. mobilis* are similar to those in RCs of *Rb. sphaeroides* R26. The positive sign of the donor signals, the proposed occurrence of the DR mechanism[15] and in particular the triplet lifetime $\tau = 100$ μs match very well with the data from R26 RCs. It is tempting to conclude that *Hb. mobilis* has a similar cofactor arrangement as for the R26 RCs, with a central special pair, accessory cofactors and primary acceptor cofactors leading to a similar dynamics of electron transfer and triplet lifetime in the two species. The triplet kinetics obtained from time resolved experiments provides evidence for a long lived donor triplet state that is not quenched by carotenoids, similar to the case of R26 RCs.

In such a scheme, any difference with the heterodimeric R26 RCs would be due to the homodimeric symmetry of the subunits in heliobacterial RCs. Alternatively, dynamic symmetry breaking of the homodimer may lead to a monomeric (accessory) chlorophyll carrying the donor charge and not a dimeric primary donor, similar to PSII.[46] The heterodimeric nature of R26 RCs leads to different chemical shifts for the two donor cofactors in the photo-CIDNP MAS NMR spectra of R26 RCs.[21] In *Hb mobilis* there is no indication for signal doubling at the donor site. At the acceptor site, a clear doubling occurs in the methine carbon region, since five instead of four signals are present. The resonances with shifts of 96.8 and 95.9 ppm and with the same intensity (Figure 2.8), are assigned to the C-5 of 8^1-OH Chl a_F cofactors. Hence, at the acceptor side a very minor difference occurs, which can be reconciled with minor symmetry breaking of the homodimer, if both branches are equally active. A similar functional symmetry of acceptor cofactors is found in PSI.[44]

2.5.2 *Structure of the early radical pair in Grünstoff*

The chemical shift patterns for the absorptive and emissive signals in Braunstoff and Grünstoff are virtually identical, and this confirms the identity of the chemical structure of the radical pair in both forms. Also for Grünstoff both branches appear to be active, as shown by the slight doubling of the signals at 92.4/90.6 (C-20) and 101.9/100.4 (C-15) (Figure 2.8). There might be a slight asymmetry of intensities observable at the C-5 signal of the acceptor at about 96.4 ppm. That the functional symmetry remains upon phototransformation demonstrates that the general radical pair structure remains unchanged and is robust. In particular, the phototransformation acts symmetrically on both parts of the homodimer.

There are two significant differences between the spectra of Braunstoff and Grünstoff: (i) The ratio between absorptive and emissive signals is shifted. This is certainly due to a weakening of the effect of DR in the first 10 μs, as demonstrated in the time-resolved experiments. It might indicate a difference in the composition of the contributions of the solid-state photo-CIDNP mechanisms in favour of the TSM, which contributes to the inversion of signals in Grünstoff. (ii) The occurrence of the ‘silent’ initial phase in the triplet evolution of Grünstoff while signals are visible in the case of Braunstoff. While after 10 μs the donor triplet state is localized and produces signal enhancement, it appears that the localization is preceded by early mobility of either the radical cation or the donor triplet state. This can be explained by the change of environment near the donor cofactor due to the involvement of accessory cofactors in early charge separation. Since the radical cation decays on the ns timescale, the observed dynamics is due to the donor triplet. In fact, complex dynamics in the excited state with coexistence of different charge transfer channels and mobility of the donor triplet state has been resolved for PS II, with the radical cation state and the ^{3}P680 located on a monomeric (accessory) chlorophyll and not on the dimeric primary donor.[47,46] Also for *Hb. mobilis*, the excitation dynamics appears complex with possibly a mobile donor triplet formed on another cofactor, most likely a photoconverted accessory cofactor, before it settles after 10 μs and forms the radical pair state that is active in the photo-CIDNP.

2.5.3 *Functional flexibility*

The accessory cofactor appears to be modified by the phototransformation from BChl *g* to Chl a_F. The presence of a donor triplet state on accessory chlorophylls has been reported in PSII at cryogenic temperature.[48,49] Most likely

Grünstoff carries the donor triplet on a accessory cofactor which resembles PSII rather than PSI. In both plant RCs an accessory pigment also acts as the primary electron donor,[50-53] although on an NMR timescale the stabilized radical pair is observed.[38,54] Similarly, charge separation in RCs of *Rb. sphaeroides* that occurs with the participation of accessory pigments is observed on the time-scale of an NMR experiment as a radical cation of the special pair.[55] Here, the radical pair observed in the Grünstoff might not be the primary radical pair, but a product of a stabilization process on the sub-μs timescale.

The RCs of heliobacteria have been proposed to be ancestors of PSI. On the one hand, bidirectional electron transfer is a feature of PSI. On the other hand, the possible involvement of an accessory cofactor in triplet formation is reminiscent of PSII, although heliobacterial RCs do not appear to be an evolutionary ancestor of PSII. This would imply that the function of RCs is rather flexible. RCs maintain a general cofactor architecture, which can be homodimeric or not, which is functionally robust for changes of the matrix, which simply lead to changes of the pathways but not a change of function. The transformation of heliobacteria confirms the remarkable combination of robustness, efficiency and flexibility of natural RCs.

The root of the photosynthesis phylogenetic tree has been difficult to ascertain. Assuming that all photosynthetic RCs have been evolved from a common homodimeric ancestor,[56,57] heliobacteria might be placed near to this ancestor, very early in evolution.[58] The remarkable flexibility of heliobacterial RCs, as demonstrated here, might have allowed for branching into type-I and type-II RCs, in an evolutionary scheme where optimization of photosynthesis for energy conversion and use as a primary biological selection criterion.

References

(1) Gest, H. *Photosyn. Res*. **1994**, 41, 17-21.

(2) Stevenson, A. K.; Kimble, L. K.; Woese, C. R.; Madigan, M. T. *Photosyn. Res.* **1997**, *53*, 1-11.

(3) Golbeck, J. *Photosyn. Res.* **2007**, *91*, 139-140.

(4) Vassiliev, I. R.; Antonkine, M. L.; Golbeck, J. H. *Biochim. Biophys. Acta.* **2001**, *1507*, 139-60.

(5) Nitschke, W.; Rutherford, A. W. *Trends. Biochem. Sci.* **1991**, *16*, 241-5.

(6) Liebl, U.; Mockensturmwilson, M.; Trost, J. T.; Brune, D. C.; Blankenship, R. E.; Vermaas, W. *Pro. Natl. Acad. Sci. USA* **1993**, *90*, 7124-7128.

(7) Olson, J. M.; Blankenship, R. E. *Photosyn. Res.* **2004**, *80*, 373-386.

(8) Gest, H.; Favinger, J. L. *Arch. Microbiol.* **1983**, *136*, 11-16.

(9) Brockmann, H.; Lipinski, A. *Arch. Microbiol.* **1983**, *136*, 17-19.

(10) Kobayashi, M.; Vandemeent, E. J.; Erkelens, C.; Amesz, J.; Ikegami, I.; Watanabe, T. *Biochim. Biophys. Acta* **1991**, *1057*, 89-96.

(11) van de Meent, E. J.; Kobayashi, M.; Erkelens, C.; Vanveelen, P. A.; Amesz, J.; Watanabe, T. *Biochim. Biophys. Acta* **1991**, *1058*, 356-362.

(12) Amesz, J. *J. Photochem. Photobio.* **1995**, *30*, 89-96.

(13) Nabedryk, E.; Leibl, W.; Breton, J. *Photosyn. Res.* **1996**, *48*, 301-308.

(14) Prince, R. C.; Gest, H.; Blankenship, R. E. *Biochim. Biophys. Acta* **1985**, *810*, 377-384.

(15) Roy, E.; Rohmer, T.; Gast, P.; Jeschke, G.; Alia, A.; Matysik, J. *Biochemistry* **2008**, *47*, 4629-4635.

(16) Zysmilich, M. G.; McDermott, A. *J. Am. Chem. Soc.* **1994**, *116*, 8362-8363.

(17) Matysik, J.; Diller, A.; Roy, E.; Alia, A. *Photosyn. Res.* **2009**, *102*, 427-435.

(18) Daviso, E.; Jeschke, G.; Matysik, J. in Biophysical Techniques in Photosynthesis II (Aartsma T.J., Matysik, J., eds.), Springer Dordrecht, pp. 385-399 (**2008**).

(19) Jeschke, G.; Matysik, J. *Chem. Phy.s* **2003**, *294*, 239-255.

(20) Prakash, S.; Alia; Gast, P.; de Groot, H. J. M.; Jeschke, G.; Matysik, J. *J. Am. Chem. Soc.* **2005**, *127*, 14290-14298.

(21) Prakash, S.; Alia; Gast, P.; de Groot, H. J. M.; Matysik, J.; Jeschke, G. *J. Am. Chem. Soc.* **2006**, *128*, 12794-12799.

(22) Daviso, E.; Alia, A.; Prakash, S.; Diller, A.; Gast, P.; Lugtenburg, J.; Matysik, J.; Jeschke, G. *J. Phys. Chem. C* **2009**, *113*, 10269-10278.

(23) Jeschke, G. *J. Chem. Phys.* **1997**, *106*, 10072-10086.

(24) Polenova, T.; McDermott, A. E. *J. Phys. Chem. B* **1999**, *103*, 535-548.

(25) McDermott, A.; Zysmilich, M. G.; Polenova, T. *Solid State Nucl. Mag. Res.* **1998**, *11*, 21-47.

(26) Goldstein, R. A.; Boxer, S. G. *Biophys. J.* **1987**, *51*, 937-946.

(27) Closs, G. L. *Chem. Phys. Lett.* **1975**, *32*, 277-278.

(28) Janssen, G. J.; Daviso, E.; van Son, M.; de Groot, H. J. M.; Alia, A.; Matysik, J. *Photosyn. Res.* **2010**, *104*, 275-282.

(29) Daviso, E.; Janssen, G. J.; Alia, A.; Jeschke, G.; Matysik, J.; Tessari, M. *J. Am. Chem. Soc.* **2011**, *133*, 16754-16757.

(30) Jeschke, G.; Anger, B. C.; Bode, B. E.; Matysik, J. *J. Phys. Chem. A* **2011**, *115*, 9919-9928.

(31) Daviso, E.; Diller, A.; Alia, A.; Matysik, J.; Jeschke, G. *J. Magn. Reson.* **2008**, *190*, 43-51.

(32) Van de Meent, E. J.; Kleinherenbrink, F. A. M.; Amesz, J. *Biochim. Biophys. Acta* **1990**, *1015*, 223-230.

(33) Schulten, E. A. M.; Matysik, J.; Alia; Kiihne, S.; Raap, J.; Lugtenburg, J.; Gast, P.; Hoff, A. J.; de Groot, H. J. M. *Biochemistry* **2002**, *41*, 8708-8717.

(34) Fischer, M. R.; de Groot, H. J. M.; Raap, J.; Winkel, C.; Hoff, A. J.; Lugtenburg, J. *Biochemistry* **1992**, *31*, 11038-11049.

(35) Matysik, J.; Alia; Hollander, J. G.; Egorova-Zachernyuk, T.; Gast, P.; de Groot, H. J. M. *Indian J. Biochem. Biophys.* **2000**, *37*, 418-423.

(36) Matysik, J.; Schulten, E.; Alia; Gast, P.; Raap, J.; Lugtenburg, J.; Hoff, A. J.; de Groot, H. J. M. *Biol. Chem.* **2001**, *382*, 1271-1276.

(37) Bennett, A. E.; Rienstra, C. M.; Auger, M.; Lakshmi, K. V.; Griffin, R. G. *J. Chem. Phys.* **1995**, *103*, 6951-6958.

(38) Diller, A.; Roy, E.; Gast, P.; van Gorkom, H. J.; de Groot, H. J. M.; Glaubitz, C.; Jeschke, G.; Matysik, J.; Alia, A. *Pro. Natl. Acad. Sci. USA* **2007**, *104*, 12767-12771.

(39) Daviso, E.; Prakash, S.; Alia, A.; Gast, P.; Jeschke, G.; Matysik, J. *Appl. Magn. Reson.* **2010**, *37*, 49-63.

(40) Prakash, S.; Tong, S. H.; Alia, A.; Gast, P.; Jeschke, G.; Matysik, J. in Photosynthesis: Fundamental Aspect to Global Perpectives, (A. ed. by van der Est, A. Bruce), Allen Press Montreal, pp. 236-237, (**2005**).

(41) Eisenmayer, T. J.; de Groot, H. J. M.; van de Wetering, E.; Neugebauer, J.; Buda, F. *J. Phys. Chem. Lett.* **2012**, *3*, 694-697..

(42) Matysik, J.; Alia; Gast, P.; van Gorkom, H. J.; Hoff, A. J.; de Groot, H. J. M. *Pro. Natl. Acad. Sci. USA* **2000**, *97*, 9865-9870.

(43) Boender, G. J . (1996) Ph.D. Thesis, University of Leiden, Leiden, The Netherlands.

(44) Santabarbara, S.; Kuprov, I.; Fairclough, W. V.; Purton, S.; Hore, P. J.; Heathcote, P.; Evans, M. C. W. *Biochemistry* **2005**, *44*, 2119-2128.

(45) Sai Sankar Gupta, K. B. (2011) Ph.D. Thesis, University of Leiden, Leiden, The Netherlands.

(46) Novoderezhkin, V. I.; Romero, E.; Dekker, J. P.; Van Grondelle, R. *Chem. Phys. Chem.* **2011**, *12*, 681–688.

(47) Lubitz, W.; Lendzian, F.; Bittl, R. *Acc. Chem. Res.* **2002**, *35*, 313-320

(48) Lendzian, F.; Bittl, R.; Telfer, A.; Lubitz, W. *Biochim. Biophys. Acta* **2003**, *1605*, 35-46.

(49) Kammel, M.; Kern, J.; Lubitz, W.; Bittl, R. *Biochim. Biophys. Acta* **2003**, *1605*, 47-54.

(50) Muller, M. G.; Niklas, J.; Lubitz, W.; Holzwarth, A. R. *Biophys. J.* **2003**, *85*, 3899-3922.

(51) Holzwarth, A. R.; Muller, M. G.; Niklas, J.; Lubitz, W. *Biophys. J.* **2006**, *90*, 552-565.

(52) Prokhorenko, V. I.; Holzwarth, A. R. *J. Phys. Chem. B* **2000**, *104*, 11563-11578.

(53) Holzwarth, A. R.; Muller, M. G.; Reus, M.; Nowaczyk, M.; Sander, J.; Rogner, M. *Pro. Natl. Acad. Sci. USA* **2006**, *103*, 6895-6900.

(54) Alia; Roy, E.; Gast, P.; van Gorkom, H. J.; de Groot, H. J. M.; Jeschke, G.; Matysik, J. *J. Am. Chem. Soc.* **2004**, *126*, 12819-12826.

(55) van Brederode, M. E.; van Mourik, F.; van Stokkum, I. H. M.; Jones, M. R.; van Grondelle, R. *Pro. Natl. Acad. Sci. USA* **1999**, *96*, 2054-2059.

(56) Xiong, J.; Bauer, C. E.; *Annu. Rev. Plant Bio.* **2002**, *53*, 503-521.

(57) Allen, J. F.; Vermaas, W. F. Evolution of photosynthesis. In: Encyclopedia of Lifesciences (ELS) (2010) John Wiley & Sons, Ltd: Chichster.

(58) Giacometti, G.; Giacometti, G. M.; *Appl. Magn. Reson.* **2010**, *37*, 13-25.

Chapter 3

Electron spin density distribution in the special pair triplet of Rhodobacter sphaeroides R26 revealed by the magnetic field dependence of the solid-state photo-CIDNP effect

---

3.1 *Abstract*

Photo-CIDNP (photochemically induced dynamic nuclear polarization) can be observed in frozen and quinone-blocked photosynthetic reaction centers (RCs) as a modification of the magic-angle spinning (MAS) NMR signal intensity upon illumination. Studying the carotenoid-less mutant strain R26 of *Rhodobacter (Rb.) sphaeroides*, experiment and theory provide converging evidence that contributions to the nuclear spin polarization from the three-spin mixing and differential decay mechanisms can be separated from polarization generated by the radical pair mechanism that is due to differential relaxation (DR) between the singlet and triplet branches. In a magnetic field of 1.4 T, the DR contribution leads to dramatic signal enhancement of about 80,000 and dominates over the two other mechanisms. The DR mechanism encodes information on the spin density distribution in the donor triplet state. Relative peak intensities in the photo-CIDNP spectra provide a critical test for triplet spin densities computed for different model chemistries and conformations. The unpaired electrons are distributed almost evenly over the two moieties of the special pair of bacteriochlorophylls, with only slight excess on the P_L half.

This chapter is published in *J. Am. Chem. Soc.* **2012**, *134*, 5921–5930.

3.2 *Introduction*

The solid-state photo-CIDNP effect at high fields, discovered by M. Zysmilich and A. McDermott in 1994 on quinone-reduced and frozen photosynthetic reaction centers,[1] provides a method to overcome the intrinsically low sensitivity of NMR by generation of non-Boltzmann populations of nuclear spin states by photochemical reactions in solids (for review, see 2,3). This photochemically induced dynamic nuclear polarization (photo-CIDNP) can be detected by magic-angle spinning (MAS) NMR as strong modifications of signal intensities. Enhancement factors of more than 10,000 have been reported for ^{13}C photo-CIDNP MAS NMR in a magnetic field of 4.7 T (*i.e.*, 200 MHz ^{1}H frequency and 50 MHz ^{13}C frequency) in photosynthetic reaction centers (RCs) of the purple bacteria *Rhodobacter (Rb.) sphaeroides* wild type (WT)[4] and the carotenoid-less mutant R26.[5] Such strong signal enhancement allows, for example, for highly selective observation of the photosynthetic cofactors at nanomolar concentrations in entire cells.[5,6] Due to the long ^{13}C relaxation time in solids, the nuclear polarization of subsequent photocycles can be accumulated in continuous illumination experiments making photo-CIDNP MAS NMR a sensitive analytical tool. It appears to be an intrinsic property of natural photosynthetic RCs[7-11] and has been proposed to be related to efficient electron transfer.[12] Recently the effect was observed in a blue-light photoreceptor, the phototropin mutant LOV1-C57S at 2.4 T, demonstrating that the effect is not limited to natural photosynthesis (see chapter 4).

The cyclic spin-chemical processes producing such high nuclear polarizations are well understood for a spin-correlated radical pair interacting with a single nuclear spin in the high-field limit in quinone-depleted and quinone-blocked RCs of *Rb. sphaeroides*.[2,13] Upon illumination, RCs of *Rb. sphaeroides*[14,15] form radical pairs with the primary electron donor P, the “special pair” of two bacteriochlorophylls (BChl), as radical cation and the primary electron acceptor Φ, a bacteriopheophytin (BPhe), as radical anion (Scheme 3.1). The initial electron spin zero-quantum coherence, which is created upon photogeneration of the radical pair in the S state in the S-T_0 manifold of states, is transferred by two solid-state mechanisms, the three-spin mixing (TSM)[16,17] and the differential decay (DD),[18] into *net* nuclear polarization. In the electron-electron-nuclear TSM mechanism, the antisymmetry between the α and β nuclear spin states in the singlet and triplet

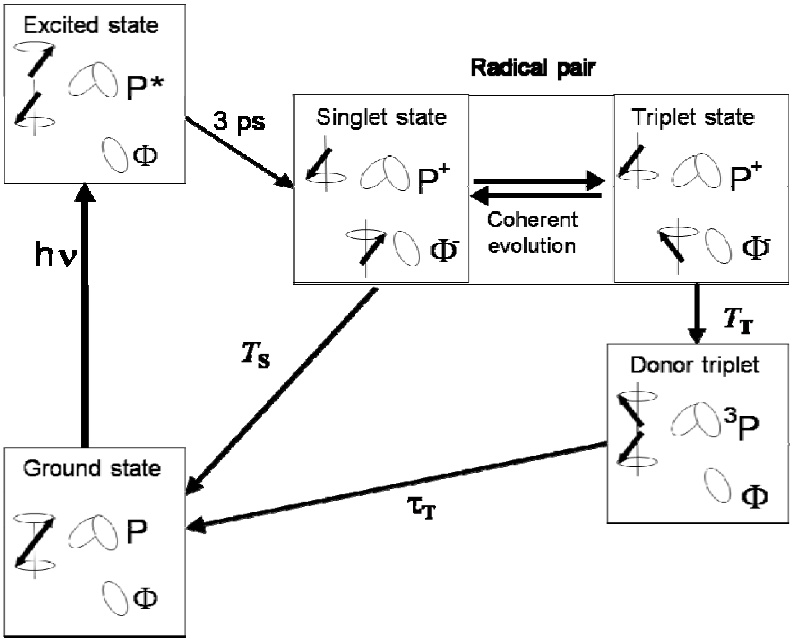

Scheme 3.1. Photocycle in quinone-blocked RCs of *Rb. sphaeroides* WT and R26. Upon illumination and fast electron transfer from an excited singlet state, a radical pair is formed in a pure singlet state having high electron spin order. The radical pair is formed by a radical cation at the two donor BChls (Special pair, P) and a radical anion on the BPhe acceptor cofactor (Φ) of the active branch. The chemical fate of the radical pair depends on its electronic spin state: while the singlet state is allowed to recombine with a lifetime of T_S = 20 ns, for the triplet state a direct recombination is spin-forbidden and a donor triplet (^{3}P) is formed by inter-system crossing with a lifetime of T_T = 1 ns. The lifetime of ^{3}P depends on the relaxation channel provided by the environment. It is short in WT RCs having a nearby carotenoid and significantly longer in the carotenoid-less mutant R26.

branches during the coherent spin evolution in the correlated radical pair is broken by state mixing due to anisotropic electron-electron dipolar coupling and pseudosecular hyperfine coupling B. The ratio $|\omega_I/A_{zz}|$ determines the extent of mixing of the nuclear spin states, and thus also the extent to which population antisymmetry is violated. State mixing is maximized at the double matching condition $2|\Delta\Omega| = 2|\omega_I| = |A|$, *i.e.*, the difference of the electron Zeeman frequencies $\Delta\Omega$, the nuclear Zeeman frequency ω_I and the secular part of the hyperfine interaction A must match. In the DD mechanism, this antisymmetry of nuclear spin populations is broken by different reaction constants of the decay of the S and the T_0 states (T_S and T_T) of the radical pair as well as by pseudosecular hyperfine coupling B. In this case, only a single matching of interactions $2|\omega_I| = |A|$ is required and the difference of singlet and triplet radical pair lifetimes must be of the order of the B^{-1}. During the radical pair evolution the occurrence of these two competing mechanisms in RCs of *Rb. sphaeroides* WT leads to a set of entirely emissive (negative) signals, whose relative intensity encodes information on the spin density distribution in the radical pair state.[4] Since $\Delta\Omega$ and ω_I depend on the magnetic field, while A does not, both the TSM and DD mechanism produce maximum absolute nuclear polarization at a matching field.

For RCs having a long donor triplet lifetime, such as the carotenoid-less mutant R26 of *Rb. sphaeroides*, contributions from a third mechanism have been observed.[5] In this situation polarization generated by the radical pair mechanism (RPM),[19,20] which has the same amplitude and opposite sign in the singlet and triplet branch and thus usually cancels in cyclic reactions, is partially maintained[21,22] due to different longitudinal nuclear relaxation in the two branches (for a review see Chapter 1). In the solid state this has been termed the differential relaxation (DR) mechanism to emphasize that RPM polarization is modified according to the different T_1 relaxation rates for different nuclei.[2] This mechanism explains the differences between photo-CIDNP spectra of RCs of *Rb. sphaeroides* WT and R26.[5] The DR mechanism relies on enhanced nuclear relaxation in the triplet branch, which is in turn caused by fluctuations of the anisotropic hyperfine couplings of these nuclei to the donor triplet (^{3}P) in its T_0 state. Therefore, the relative line intensity in this case also encodes information on the spin density distribution in the ^{3}P state.[5] Such information is of interest to understand the photoprotection of the RCs by fast triplet quenching.[14] In addition, studies of the triplet state of bacterial RCs have provided insight into the strongly asymmetric distribution of electron transfer between the nearly symmetric M and L branches of bacterial RCs.[23,24]

In practice, the three mechanisms are operative simultaneously, and for the DR mechanism the relative line intensities depend on the spin density distribution in both the radical pair state (through the RPM) and the donor triplet state (through paramagnetically induced relaxation). In the present work, it is demonstrated that these contributions can be disentangled. The analysis relies on the separate characterization of the RPM polarization by time-resolved ^{13}C photo-CIDNP MAS

NMR[25] and on different field dependences of the three mechanisms. Previous experimental studies on both RC types WT and R26 clearly demonstrated a strong increase of the photo-CIDNP enhancement with lower fields between 17.4 and 4.7 T.[4,5] From the experiment it is not known whether the enhancement further increases and at which field a maximum occurs. The discovery of the effect in a blue-light photoreceptor occurred at an even lower field of 2.4 T (see chapter 4). Simulation of the TSM and DD mechanisms in the high field to medium field range (17.6T to 1.4T) for photosynthetic RCs suggests a maximum polarization at ≈2 T for ^{13}C nuclei,[26] which has not been experimentally verified to date. Although information on the relaxation dispersion of the electron spin in the donor triplet ^{3}P is restricted, relaxation theory suggests that for the expected electron T_1 spin relaxation times in the microsecond range, paramagnetic relaxation enhancement increases down to fields well below 2 T.[27] Accordingly, DR polarization should dominate at sufficiently low fields. Here, an experimental "trial drill" towards lower fields, as far as commercial NMR hardware allows, is provided. At the fields of 1.4 and 2.4 T, coherent evolution is still strictly within the S-T_0 manifolds, and the contribution of a recently proposed TSM mechanism based on S-T_- mixing[28] appears negligible.

3.3 *Materials and Methods*

3.3.1 *Sample Preparation*

RCs from *Rb. sphaeroides* WT were isolated as described by Shochat *et al.*,[29] RCs from *Rb. sphaeroides* R26 were isolated by the procedure of Feher and Okamura.[30] The removal of Q_A has been done by incubating the RCs at a concentration of 0.6 μM in 4% LDAO, 10 mM *o*-phenanthroline, 10 mM Tris buffer, pH 8.0, for 6 h at 26 ˚C, followed by washing with 0.5 M NaCl in 10 mM Tris buffer, pH 8.0, containing 0.025% LDAO and 1mM EDTA.[31] Approximately 5 mg of the RC protein complex embedded in LDAO micelles was used for NMR measurements.

3.3.2 *MAS-NMR Measurements*

The NMR experiments in different fields were performed with DSX-750, DMX-400, DMX-200, AV-100 and AV-60 NMR spectrometers equipped with MAS probes (Bruker, Karlsruhe, Germany). The sample was loaded into a clear 4-mm sapphire rotor and inserted into the MAS probe. The sample was frozen slowly at a low spinning frequency of ν_r = 400 Hz to ensure a homogenous sample distribution against the rotor wall.[32] The light and dark spectra were collected with a Hahn echo pulse sequence and TPPM proton decoupling.[33] The hardware of the spectrometer does not allow for proton decoupling in magnetic fields less than 2.4 Tesla. The spectra at lower magnetic fields were measured with an anti-ringing pulse sequence.[34] All ^{13}C photo-CIDNP MAS NMR spectra were obtained at a temperature of 235 K with continuous illumination using white light.[35]

The MAS rotation frequency was 8 kHz in all experiments. For the five fields of 1.4, 2.4, 4.7, 9.6 and 17.6 Tesla, line broadenings of 10 Hz, 10 Hz, 20 Hz, 50 Hz or 120 Hz, respectively, were applied prior to the Fourier transformation. In all cases, a cycle delay of 4 s was used. The ^{13}C MAS NMR spectra were referenced to TMS by using the ^{13}COOH response of solid tyrosine·HCl at 172.1 ppm.

3.3.3 *Simulations*

Hyperfine anisotropies ΔA_k in the donor triplet state were computed with ADF 2004.1,[36,37] employing the BLYP functional[38,39] and DP basis sets for ^{13}C nuclei based on the special pair structure from *Rb. sphaeroides* R26 in the charge-neutral state (PDB entry 1AIJ)[40] and with ADF 2009.1[36,41] utilizing a TZP basis set and the BP86 functional.[38,39] The coordinates from the charge-neutral state of *Rb. sphaeroides* WT (PDB entry 1PCR)[42] have been amended with hydrogen atoms and optimized in Turbomole V6.0. For the geometry optimization a TZVP[43] basis and the BP86 functional have been used in combination with the RI approximation using the standard TZVP basis set from Turbomole.[44,45] Coordinates were first optimized for the radical cation state and relaxed in the ^{3}P configuration. DR intensities have been simulated by a home-written Matlab program as described in ref 5, assuming that the nuclear longitudinal relaxation rate constant $1/T_{1n}$ is proportional to the square of the hyperfine anisotropy ΔA^2 (*vide infra*). Here, ΔA is defined as $3(A_z - a_{\mathrm{iso}})/2$, where A_z is the largest eigenvalue of the hyperfine tensor and a_{iso} its trace. Calculation of polarizations for the singlet and triplet branches due to RPM was done by the density operator formalism as described in refs 4 and 5.

3.4 *Results*

Figures 3.1 and 3.2 show the amplitude of the solid-state photo-CIDNP effect in the magnetic field range from 2.4 to 17.6 T in WT and R26, respectively. In this regime, ^{13}C MAS NMR data can be acquired with ^{1}H decoupling. While dark experiments (Figures 3.1 and 3.2, right panel) show an increase in signal intensity and resolution towards higher field, the light-induced signals (Figures 3.1 and 3.2, left panel) show the opposite trend. The lower the field, the stronger the intensity of the light induced signals. The optimum for the spectral resolution is reached at about 4.7 T (200 MHz ^{1}H frequency) since at 2.4 T the spectral dispersion is poor while at higher field artificial line-broadening is required to compensate for low signal-to-noise ratio. In this field range, these trends hold for both types of RCs, WT (Figure 3.1) and R26 (Figure 3.2). Hence, the question arises whether or not the enhancement further increases at even lower field.

Over the entire field range, the intensity patterns are different for the spectra of WT and R26 RCs. While the first provide entirely emissive spectra, for the latter both emissive and absorptive lines occur. Previous analysis has shown that a set of entirely emissive signals originates from both the donor and the acceptor of the primary radical pair of WT RCs (Figure 3.1).[4,13] This non-equilibrium polarization has been interpreted in terms of competing TSM and DD mechanisms.[4] The all-emissive spectrum is caused by a predominance of the TSM over the DD mechanism. For the DD contribution, the sign of the signal depends on the signs of the secular hyperfine coupling and of the g tensor difference.[2] In R26 RCs, the DR mechanism leads to admixture of polarization from the RPM for those donor nuclei that exhibit strongly anisotropic hyperfine couplings in the ^{3}P state.[2] For positive isotropic hyperfine couplings in the radical pair state this DR polarization is absorptive, while it is emissive for negative isotropic hyperfine couplings in the

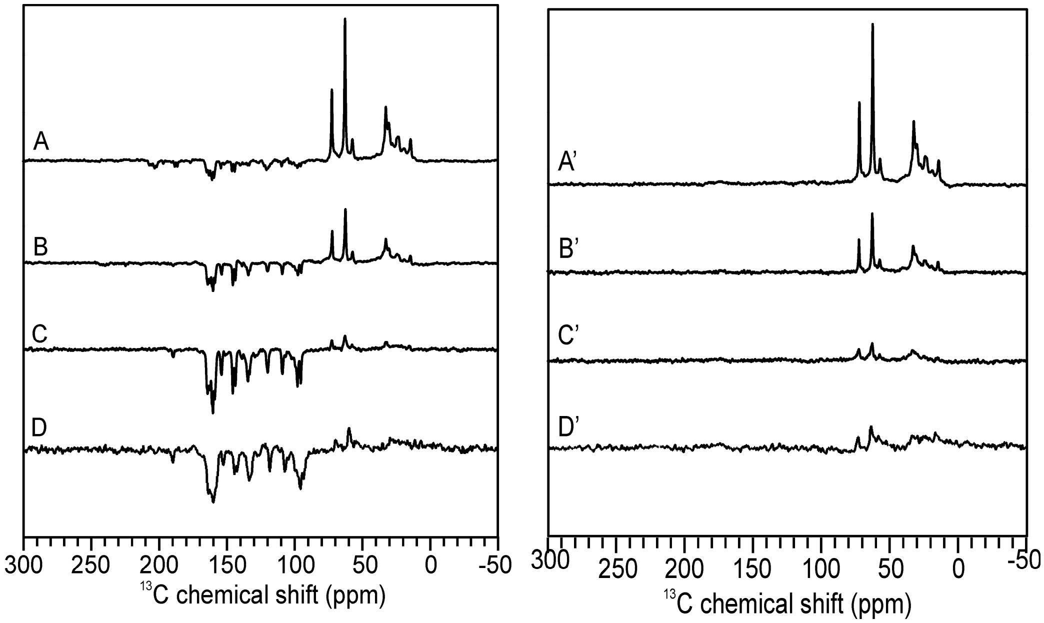

Figure 3.1. ^{13}C MAS NMR spectra of quinone depleted RCs of *Rb. sphaeroides* WT in the dark (right panel) and with illumination (left panel) in a field of 17.6 T (A, A'), 9.4 T (B, B'), 4.7 T (C, C') or 2.4 T (D, D'). The spectra were obtained at 235 K with a MAS frequency of 8 kHz using ^{1}H decoupling.

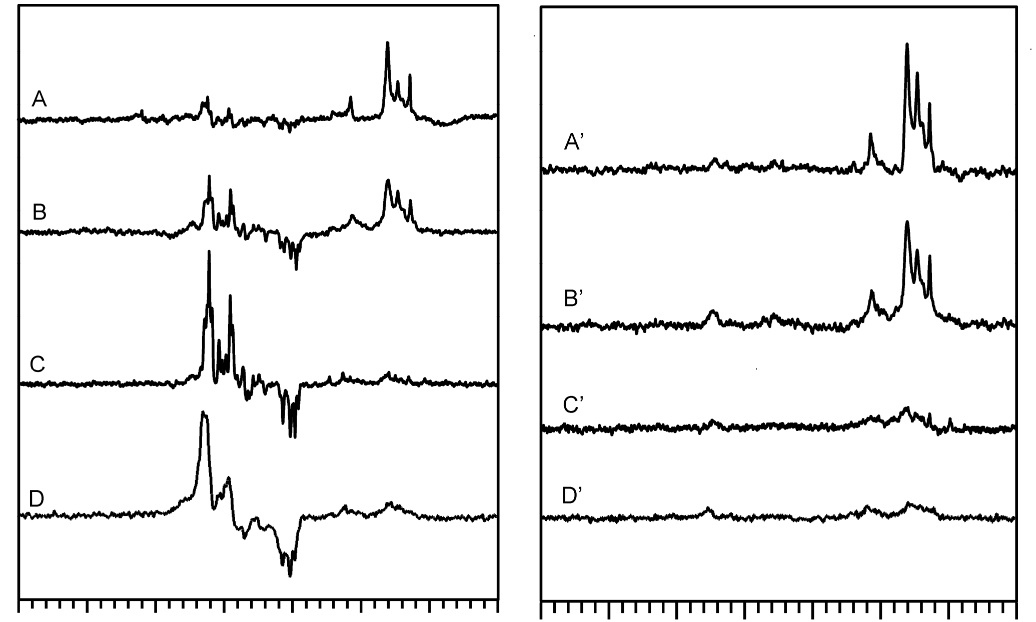

Figure 3.2. ^{13}C MAS NMR spectra of quinone depleted RCs of *Rb. sphaeroides* R26 in the dark (right panel) and with illumination (left panel) in magnetic fields of 17.6 T (A, A'), 9.4 T (B, B'), 4.7 T (C, C') or 2.4 (D, D') T. The spectra were obtained at 235 K with a MAS frequency of 8 kHz using ^{1}H decoupling.

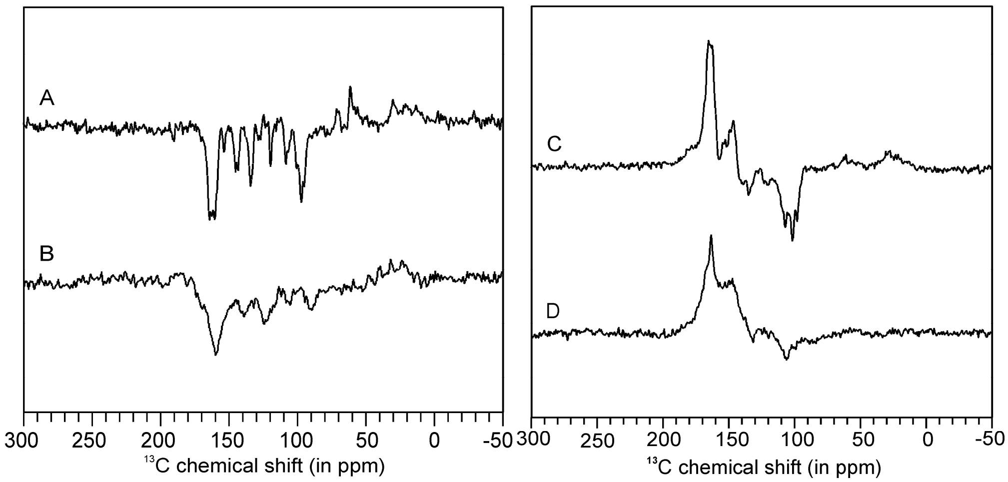

Figure 3.3: ^{13}C photo-CIDNP MAS NMR spectra of *Rb. sphaeroides* WT (left panel) and R26 (right panel) RCs in a magnetic field of 2.4 T with ^{1}H decoupling (A, C) and without ^{1}H decoupling (B, D).

radical pair state. This sign rule may be violated if the anisotropic contribution strongly dominates over the isotropic contribution to the hyperfine coupling in the radical pair state. Generally the field dependence of the TSM, DD, and DR mechanisms may be different, implying that also the spectral pattern changes with the field. In the photo-CIDNP spectra of R26 RCs (Figure 3.2), however, the ratio of negative to positive signals appears to depend only weakly on the field strength.

In magnetic fields less than 2.4 T, our hardware does not allow for ^{1}H decoupling. To compare the effect of decoupling on the spectra, we measured ^{1}H–coupled and decoupled spectra for both samples (Figure 3.3) in a field of 2.4 T. The comparison shows that in particular the signals around 100 ppm, originating from methine bridge carbons that are directly bound to a proton, are broadened beyond detection in the ^{1}H-coupled spectra while the other signals broaden substantially.

Experiments in magnetic fields of 2.4 and 1.4 T (100 and 60 MHz ^{1}H frequency, respectively) for RCs of WT and R26 are shown in Figures 3.4 and 3.5. In Figure 3.4 the solid-state photo-CIDNP effect considerably weakens towards lower fields. Hence, the present data provide empirical evidence that the coherent high-field solid-state photo-CIDNP effect for bacterial RCs shows a maximum around 2.4 T. In Figure 3.5, on the other hand, the light-induced positive feature strongly increases towards lower field. The ratio between positive and negative

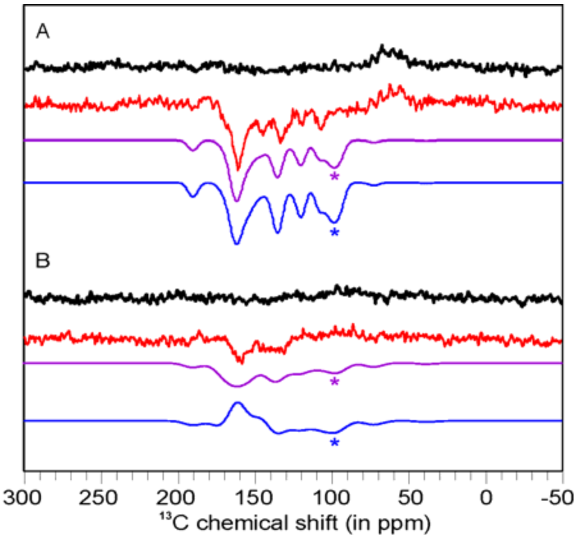

Figure 3.4. ^{13}C MAS NMR spectra of quinone depleted RCs of *Rb. sphaeroides* WT in the dark (black) and with illumination (red), as well as numerical simulations of the photo-CIDNP effect with T_{1T} = 100 ns (lilac) and T_{1T} = 56 ns (blue) at 2.4 Tesla (A) and 1.4 Tesla (B). The experimental data were obtained at a temperature of 235 K with a MAS frequency of 8 kHz and without ^{1}H decoupling. The asterisks mark methine carbon signals that are lost without decoupling.

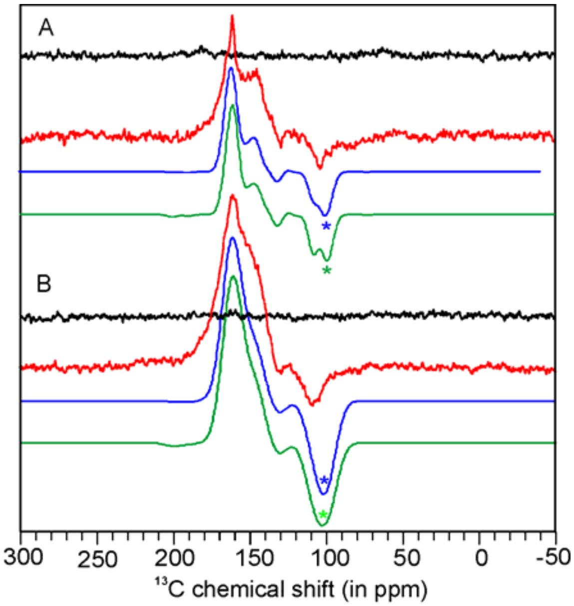

Figure 3.5. ^{13}C MAS NMR spectra of quinone depleted RCs of *Rb. sphaeroides* R26 in the dark (black) and with illumination (red) as well as numerical simulations of the photo-CIDNP effect with T_{1T} = 56 ns and triplet spin density from DFT computations with the BLYP functional (blue) and the BP86 functional (green) in magnetic fields of 2.4 Tesla (A) and 1.4 Tesla (B). The experimental data were obtained at 235 K with a MAS frequency of 8 kHz and without ^{1}H decoupling. The asterisks mark methine carbon signals that are broadened without decoupling.

signals is changed strongly in favor of the first. Thus, while the TSM and DD mechanisms become less efficient at 1.4 T, the DR mechanism becomes more potent. Experiments at even lower fields would require a different type of hardware. In particular, a field cycling system would be suitable to avoid further loss of resolution.

All spectra are presented with similar signal-to-noise ratio. In previous work, using the response of the methyl groups as an internal standard for estimating the enhancement factor of the solid-state photo-CIDNP effect, this factor was found to be about 10000 in a magnetic field of 4.7 T.[4,5] The methyl signal at 30 ppm corresponds to the ~3300 methyl groups in the RC protein. The experiments at 2.4 T for RCs of WT and R26 show stronger enhancement compared to 4.7 T. Using the same standard for the spectra obtained at 2.4 T, enhancement factors have been determined to be 20000 for WT RCs and 40000 for R26 RCs.

Because proton decoupling is not feasible with the spectrometer in our laboratory operating at magnetic fields less than 2.4 T, the enhancement factor cannot be calculated as above. It is, however, possible to estimate the enhancement factor in R26 RCs by comparing with the data collected without proton decoupling at 2.4 and 1.4 T from the same sample in the same measurement time (Figure 3.5 A and B). Since decoupling does not affect the polarization, the factor 40000 is to a reasonable approximation also valid for the spectrum obtained without ^{1}H decoupling. To estimate the polarization, the absorptive and emissive signals are integrated for the spectra of R26 RCs collected in magnetic fields of 2.4 and 1.4 T. The ratio of emissive to absorptive signals appears to be twice as large in a magnetic field of 1.4 T compared to the ratio in spectra acquired at 2.4 T. If the contributions from the DD and TSM mechanisms remain the same when decreasing the field strength, the enhancement factor for R26 RCs at 1.4 T can be estimated as 80000. This is a lower limit, since our simulations (*vide infra*) indicate that the contribution from the DD and TSM mechanisms decreases between 2.4 and 1.4 T.

The photo-CIDNP results indicate that for the lowest fields indeed contributions from the DR mechanism are very strong and dominate over the TSM and DD processes. This gives rise to the opportunity of characterizing the spin

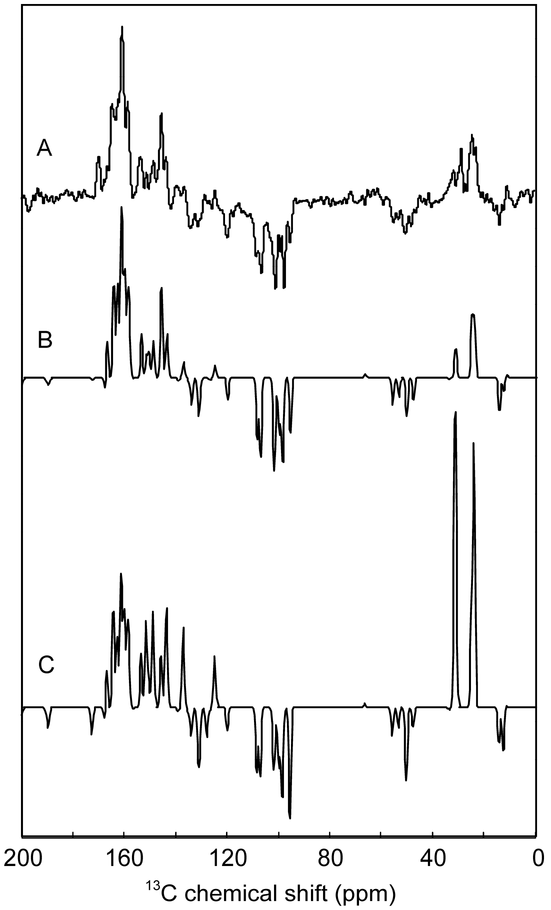

Figure 3.6: ^{13}C photo-CIDNP MAS NMR spectrum of *Rb. sphaeroides* R26 RCs in a magnetic field of 4.7 T immediately after a nanosecond laser flash[25] (A), fit obtained in matlab by scaling factors for simulated peak intensities (B) and simulation using the ΔA_k for the radical pair state from a DFT computation[5] (C).

density distribution for the triplet state of the special pair, ^{3}P. To do so, an estimate of the nuclear polarization generated by the RPM in the singlet and triplet branch with opposite signs is required. In principle, such an estimate can be obtained from simulations. For this, experimentally unknown ^{13}C hyperfine parameters ΔA_k in the radical pair state are required, which can be estimated by density functional theory (DFT) computations.[4,5] This approach does, however, introduces uncertainty from errors in the DFT calculations, which are approximate.

Here, a different route is followed, where the RPM polarization pattern is taken from time-resolved photo-CIDNP MAS NMR experiments that allow to observe the spectrum immediately after a single photocycle has been initiated by a laser pulse.[25] At that time polarization from the singlet branch, *i.e.* from cofactors in RCs that have returned to the ground state following decay from the S state, is selectively detected, as RCs in the triplet branch are still in a paramagnetic state which shifts and broadens the NMR signals beyond detection. We have performed a linear least squares fit of the spectrum of *Rb. sphaeroides* R26 RCs obtained immediately after the nanosecond flash at 4.7 T[25] in Matlab with lorentzian lines by scaling of nuclear polarization values that were obtained using ΔA_k estimates from a DFT-based computation (Figure 3.6). This provides a table representing the intensity profile for the RPM polarization signal that can serve as a template for simulations. We apply this profile in all further analysis, although strictly it applies only at 4.7 T. By comparing simulations with and without such scaling to the experimental spectra, it was confirmed that RPM polarization scaled by the experimentally derived intensity factors provides a better approximation at the other fields than the RPM polarization simulated directly from DFT-computed ΔA_k values.

To simulate polarizations from the DR mechanism, the nuclear longitudinal relaxation times $T_{1\mathrm{n},k}$ in the ^{3}P state are required. In a first exploration of the DR mechanism,[46] McDermott *et al.* used a uniform *ad hoc* relaxation time of 300 s^{-1} to fit ^{15}N photo-CIDNP MAS NMR data. In contrast with this earlier simplified treatment, I find that it is possible to use the powder-averaged Redfield theory expression

$$T_{1\mathrm{n},k} = 45\,\omega_I^2\, T_{1\mathrm{T}} / (4\Delta A_k^2) \qquad (3.1)$$

as well, as a first approximation, where $\Delta A_k = 3(A_{z,k} - a_{\mathrm{iso},k})/2$ is the hyperfine anisotropy of nucleus k, ω_I is the nuclear Zeeman frequency, which scales linearly with the magnetic field, and $T_{1\mathrm{T}}$ is the longitudinal electron spin relaxation time in the ^{3}P state.[*] The z-axis is here again along the principal component with the largest magnitude. Eq. (3.1) can be obtained from an expression for the paramagnetic relaxation in solids derived by Abragam[27], by replacing the distance-dependent dipole-dipole coupling between electron and nuclear spin by the ΔA_k which is

---

[*] Eq (3.1) matches Abragam's definition $\Delta A = 3\gamma_\mathrm{I}^2\gamma_\mathrm{S}^2\nabla^2\mu_0^2/(16\pi^2 r^6)$ for the point-dipole approximation. This expression is a factor of three smaller than the convention used in this chapter, and because the square of ΔA is used, a factor of 9 is introduced in the numerator of Eq. (3.1) relative to the existing literature.[27]

Cofactor	Atom number	ΔA_k ^{13}C hfi anisotropy [MHz]
P_L	1	8.8
	2	12.7
	3	3.8
	3'	0.6
	4	9.3
	5	1.8
	6	8.7
	9	10.6
	10	2.7
	11	9.7
	12	15.1
	13	3.1
	13'	1.2
	14	7.9
	15	5.2
	16	13.0
	19	10.2
	20	5.8
P_M	1	6.2
	2	9.8
	3	2.5
	4	5.8
	5	2.9
	6	4.9
	9	7.0
	10	4.5
	11	6.5
	12	12.1
	13	2.1
	13'	1.2
	14	5.8
	15	3.0
	16	7.5
	19	6.3
	20	3.8

Table 3.1. Hyperfine anisotropies ΔA_k for the ^{13}C nuclei in the L and M moieties computed by DFT with the BLYP functional.

largely due to spin density in p_z orbitals, and assuming $|\omega_I T_{1T}| >> 1$, which applies for all magnetic fields used in this work.

From measurements of T_{1T} in *Rb. sphaeroides* R26 RCs along the Y axis of the zero-field splitting tensor at a temperature of 233 K and a field of

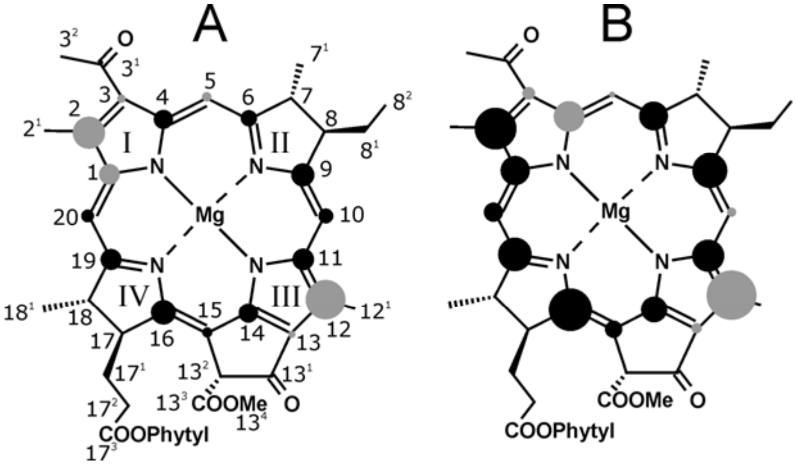

Figure 3.7. Spin density distribution in the special pair triplet state visualized via the relative anisotropic hyperfine parameter ΔA_k for the ^{13}C nuclei computed by DFT with the BLYP functional in the M (A) and L (B) moiety. Atom numbering is shown in (A). A circle diameter of one carbon-carbon bond length corresponds to $\Delta A_k = 2\pi\cdot 15$ MHz. Black circles correspond to hyperfine anisotropies that can be experimentally tested, while gray circles indicate the hyperfine anisotropies that are not accessible experimentally.

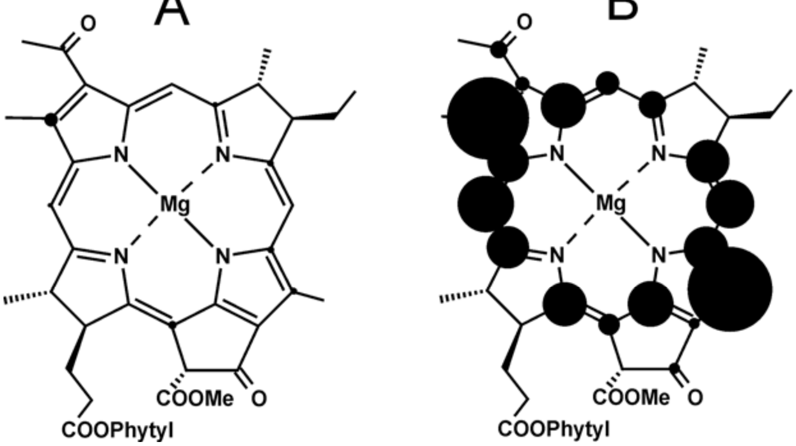

Figure 3.8: Spin density distribution in the special pair triplet state visualized via relative anisotropic ^{13}C hyperfine parameters ΔA_k computed by DFT with the BP86 functional in the M (A) and L (B) moiety. The atom numbering is same as in Figure 3.6 A. A circle diameter of one carbon-carbon bond length corresponds to $\Delta A_k = 2\pi\cdot 15$ MHz.

approximately 0.35 T,[47] we expect that T_{1T} is in the microsecond range. Our DFT computations show that the ΔA_k for the nuclei with the largest spin density are of the order of $2\pi\cdot 10$ MHz (Table 3.1). The Redfield regime normally breaks down when $T_{1T} \sim 3/\Delta A_k$ and is violated for T_{1T} larger than ~ 20 ns. However, the scaling with ΔA_k^2 is expected to hold for $\Delta A_k << 2\ \omega_I$, *i.e.* up to ~ 10 T as in this regime second order perturbation theory, as simplified in Redfield theory, provides a good approximation.[27] In addition, preliminary computations for electron spin 1/2 indicate that the Redfield approximation remains valid throughout the range of T_{1T} and ΔA_k encountered in this work (data not shown). Since Redfield theory is semi classical, it is applicable to spin 1 electronic systems as well.

Estimates for the ΔA_k in Eq. (3.1) were obtained by two DFT computations for the triplet state of the special pair. The first computation, used already in [5] was based on non-optimized heavy atom coordinates of the x-ray crystal structure of R26 RCs in the charge neutral state (PDB 1AIJ).[40] Protons were attached with standard bond lengths and geometries and a spin-unrestricted computation with the BLYP functional was performed.[38,39] This leads to a spin density that is almost symmetrically distributed over the two moieties of the special pair, with only a

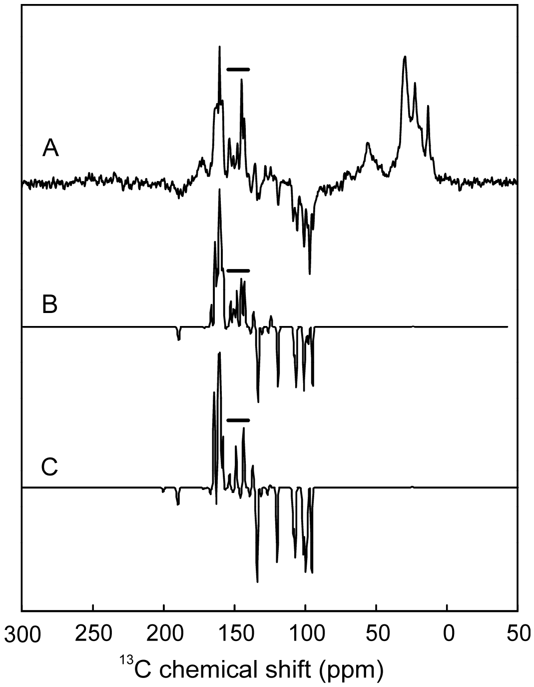

Figure 3.9. ^{13}C MAS NMR spectrum of quinone depleted RCs of *Rb. sphaeroides* R26 under illumination at 4.7 T (A) as well as numerical simulations of the photo-CIDNP effect with T_{1T} = 56 ns and triplet spin density from DFT computations with the BLYP functional (B) and the BP86 functional (C). The bars denote a spectral range where the number of signals differs in the two simulations.

slight excess in the L moiety (Figure 3.7). In the second DFT computation the WT special pair structure was optimized in TURBOMOLE[48] first for the radical cation state and then for the triplet state and the ΔA_k were obtained by a spin-unrestricted computation with the BP86 functional.[38,49] This led to a completely asymmetrical spin density distribution with both unpaired electrons being localized almost exclusively on the L moiety (Figure 3.8).

Nuclear polarization after a single photocycle for R26 RCs for the singlet branch ($p_{S,k}$) and triplet branch ($p_{T,k}$) due to RPM, and the TSM and DD mechanisms was computed by the density operator formalism, following the procedures described in reference [5]. Polarization p_k after return of molecules from both branches to the ground state was taken as an approximation for the steady-state polarization observed in our experiments. This is computed by

$$p_k = p_{S,k} + [1- \exp(-\tau_T/T_{1n,k})]\, p_{T,k} \qquad (3.2)$$

where τ_T is the triplet lifetime (100 µs for R26 and 0.1 µs for WT RCs) and the $T_{1n,k}$ are calculated by Eq. (3.1). For every spectrum T_{1T} in Eq. (3.1) is the only fit parameter. Finally, the p_k are multiplied by the experimental RPM scaling factors

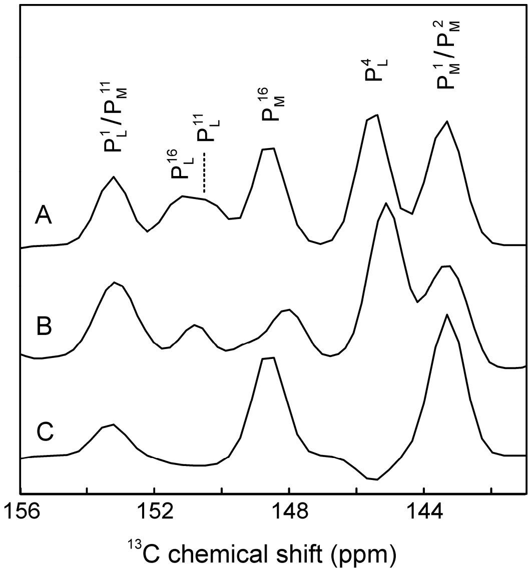

Figure 3.10. Detail of the ^{13}C photo-CIDNP MAS NMR spectrum of quinone depleted RCs of *Rb. sphaeroides* R26 obtained with continuous illumination in a magnetic field of 9.4 T (A), as well as numerical simulations of the photo-CIDNP effect with T_{1T} = 56 ns and triplet spin density from DFT computations with the BLYP functional (B) and the BP86 functional (C).

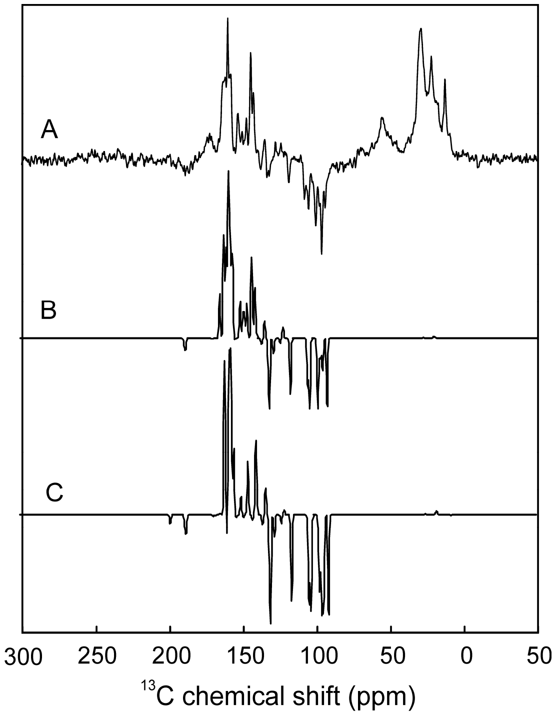

Figure 3.11: ^{13}C MAS NMR spectrum of quinone depleted RCs of *Rb. sphaeroides* R26 obtained with continuous illumination in a magnetic field of 9.4 T (A), as well as numerical simulations of the photo-CIDNP effect with T_{1T} = 0.5 μs and triplet spin density from DFT computations with the BLYP functional (B) and the BP86 functional (C).

that were obtained by fitting the time-resolved photo-CIDNP MAS NMR data collected at 4.7 T and shown in figure 3.6. Figure 3.9 shows the analysis of the data collected at 4.7 T. The best fit for both sets of ΔA_k with T_{1T} = 56 ns is obtained here. Well in line with earlier investigations, the agreement between experiment and simulation is better for the BLYP computation without geometry optimization of the R26 structure (Figure 3.9 B) than for the BP86 computation after geometry optimization of the WT structure (Figure 3.9 B). In particular, in the chemical shift range between 141 and 156 ppm (overbars) the number of signals differs between the two simulations and only the BLYP simulation agrees with experiment.

The analysis of the data collected in a magnetic field of 9.4 T confirm that T_{1T} = 56 ns over a considerable field range. From the detail plot shown in Figure 3.10 it is clear that signals from both moieties are experimentally observed with similar intensity, as is predicted by the BLYP computation without geometry optimization of the R26 structure, but not by the BP86 simulation with geometry optimization of the WT structure (see Figure 3.11 for simulation of the complete

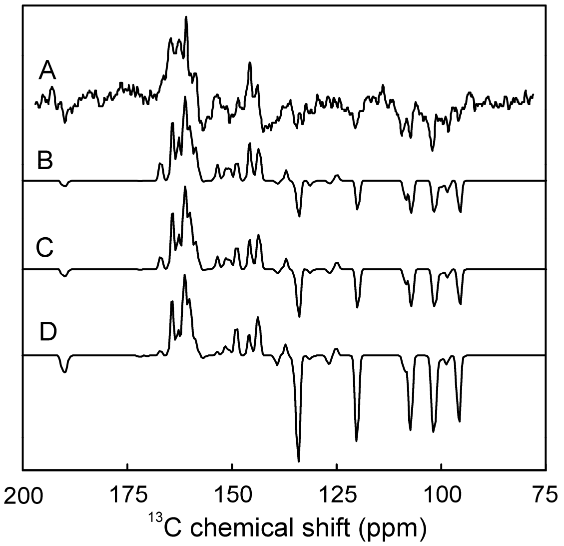

Figure 3.12. Detail of the ^{13}C MAS NMR spectrum of quinone depleted RCs of *Rb. sphaeroides* R26 under illumination in a magnetic field of 17.6 T (A) as well as numerical simulations of the photo-CIDNP effect triplet spin density using the ΔA_k from DFT computations with the BLYP functional at T_{1T} = 56 ns. (B), T_{1T} =22 ns (C) , and T_{1T} = 11 ns (D).

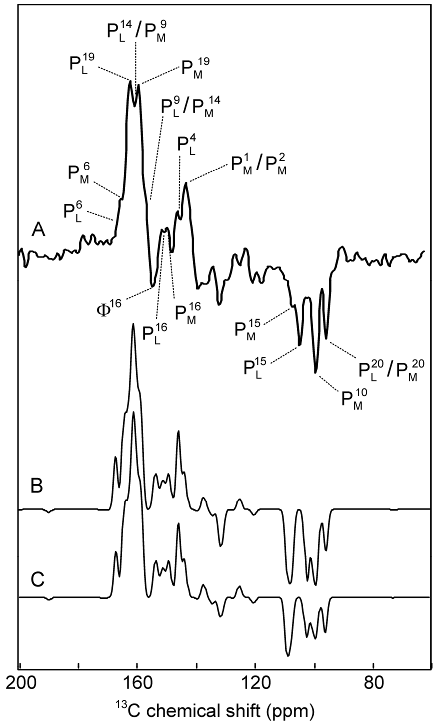

Figure 3.13 Detail of the ^{13}C MAS NMR spectrum of quinone depleted RCs of *Rb. sphaeroides* R26 under illumination in a magnetic field of 2.4 T (A) as well as numerical simulations of the photo-CIDNP effect triplet spin density from DFT computations with the BLYP functional at T_{1T} = 56 ns (B) and T_{1T} = 222 ns (C). To enhance the resolution for peak assignment, the experimental spectrum was subjected to a line-narrowing Lorentz-Gauss transformation.

spectrum). Simulation of the ^{13}C photo-CIDNP MAS NMR spectrum of R26 RCs at 17.6 T with the same T_{1T} = 56 ns that led to the best fits at 4.7 and 9.4 T results in an overestimate of the emissive signal intensity compared to the enhanced absorptive intensity (compare the spectra A and D in Figure 3.12). At this field the best overall fit quality is obtained with T_{1T} between 11 and 22 ns (spectra B and C). At the lowest field where a decoupled spectrum is obtained (2.4 T), the relative peak intensities depend rather weakly on T_{1T} (Figure 3.13). This is because already at T_{1T} = 222 ns (C) the prefactor $1\text{-}\exp(-\tau_T/T_{1n,k})$ in Eq. (2) is close to zero for most nuclei with significant RPM intensity. The fit quality only slightly improves for T_{1T} = 111 ns (not shown) and 56 ns (B) and degrades again towards shorter T_{1T}.

In contrast, in simulations of the WT spectra with τ_T = 100 ns for a magnetic field of 2.4 and 1.4 T, a marked dependence of the signal strength on T_{1T} in that range is detected (Figure 3.4). Due to the inverse square dependence of the relaxation rate $1/T_{1n,k}$ implied by Eq. (3.1), nuclear spin relaxation in the triplet branch can potentially become significant at such fields, even for the short-lived triplet state in WT RCs. For WT RCs, T_{1T} as short as 56 ns can be excluded at 1.4 T. Considering the relatively poor signal-to-noise ratio of these spectra, any $T_{1T} \geq 100$ ns provides acceptable fits and only a lower limit of T_{1T} is derived, although line shapes slightly change at longer T_{1T}.

For simulations of the field dependence of polarization due to the DR mechanism, an ad hoc power law $T_{1T} = 22.2\cdot(17.6\text{ T}/B_0)^{0.69}$ ns was used, where B_0 is the magnetic field. The prefactor and exponent were chosen to provide a good match with the T_{1T} values at 17.6 and 4.7 T. This empirical choice fits all R26 spectra (Figure 3.14) and the WT spectra at 1.4 and 2.4 T (Figure 3.15).

Due to the square dependence of the $T_{1n,k}$ on ω_I and thus B_0 implied by Eq. (3.1), the empirical power law for T_{1T} leads to a scaling factor of $\mathrm{B}_0^2/\mathrm{B}_0^{0.69} = B_0^{1.31}$ $T_{1n,k}$. According to Eq. (3.2), such shortening of the $T_{1n,k}$ with decreasing field in turn leads to $p_k = p_{S,k}$ at sufficiently low field. Under such conditions the full nuclear polarization due to the RPM would be maintained and the Kaptein sign rules for cage products would apply.[50]

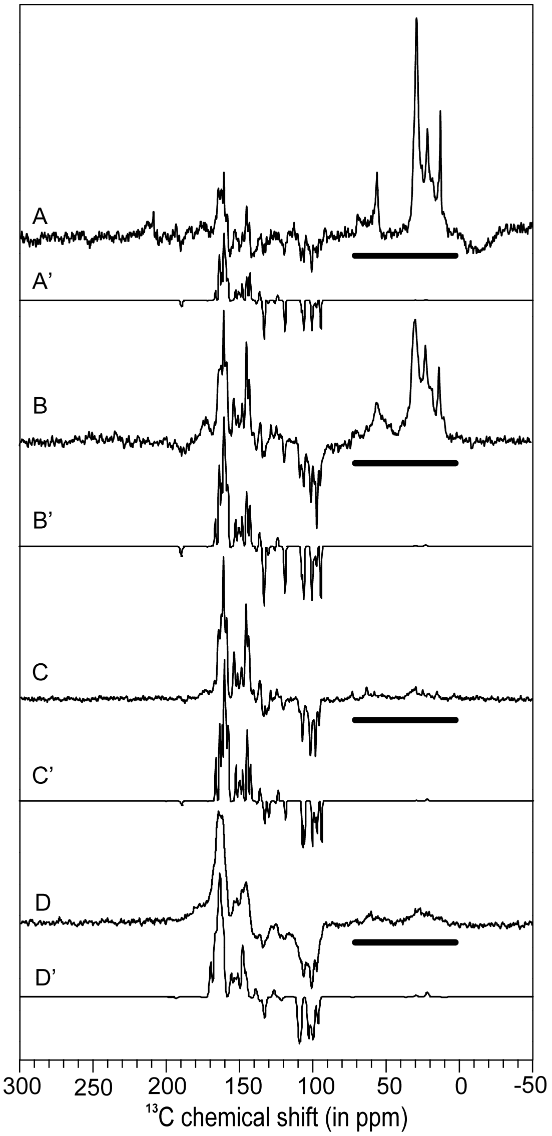

Figure 3.14: ^{13}C MAS NMR spectra of quinone depleted RCs of *Rb. sphaeroides* R26 with polarization enhancement by illumination in a magnetic field of 17.6 T (A), 9.4 T (B), 4.7 T (C), and 2.4 T (D) as well as numerical simulations of the photo-CIDNP effect with $T_{1T} = 0.2 \cdot (17.6\ \mathrm{T}/B_0)^{0.69}$ µs with triplet ΔA_k from a DFT computation with the BLYP functional without geometry optimization of the crystal structure at 17.6 (A’), 9.4 (B’), 4.7 (C’), and 2.4 (D’) Tesla. The experimental data were obtained at 235 K with a MAS frequency of 8 kHz and using ^{1}H decoupling. Signals in the chemical shift range indicated by bars are present already in the dark.

The trend in nuclear polarization predicted from the simulations is in qualitative agreement with experimental observations (Figure 3.16 A). For WT RCs, maximum emissive polarization is expected around 4.7 T, while for the

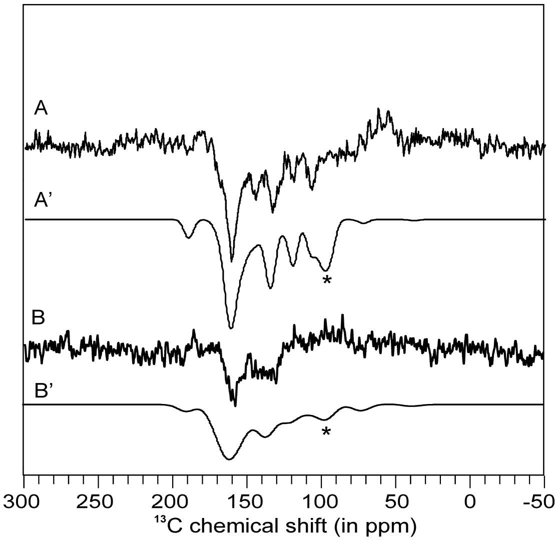

Figure 3.15: ^{13}C MAS NMR spectra of quinone depleted RCs of *Rb. sphaeroides* WT obtained by illumination in a magnetic field of 2.4 (A) and 1.4 (B) Tesla as well as numerical simulations of the photo-CIDNP effect with $T_{1T} = 0.2 \cdot (17.6\ \mathrm{T}/B_0)^{0.69}$ µs with triplet ΔA_k from a DFT computation with the BLYP functional without geometry optimization of the crystal structure for magnetic field strengths of 2.4 (A') and 1.4 (B') Tesla. The experimental data were obtained at a temperature of 235 K with a MAS frequency of 8 kHz and without ^{1}H decoupling. The asterisks denote methine carbon signals that are lost by broadening in spectra without decoupling.

polarization is very small at 1.4 T. The polarization in magnetic fields of 0.96, 0.48, and 0.24 T is also computed. These data points suggest that at even lower fields absorptive polarization due to the DR mechanism should appear. Note, however, that NMR sensitivity for a specific nuclear polarization scales with the square root of the magnetic field. If this scaling is taken into account, the maximum sensitivity in the low-field emissive spectra is expected to be about the same as for the absorptive spectra collected at 2.4 T and certainly worse than for the data obtained in a field of 4.7 T. Comparison of Figure 3.16 A and 3.17 A reveals that the emissive polarization in WT RCs in magnetic fields lower than 1.4 T in the *ad hoc* power law approach is due to the DR mechanism, since it vanishes at infinite T_{1T}.

For R26 RCs, the maximum nuclear polarization is predicted around 1.4 T, although the sensitivity for the same line width may be slightly better at 2.4 T (Figure 3.16 B). The contribution of acceptor signals to the maximum polarization corresponding to the blue dashed line, is comparable to the emissive donor signals at 4.7 T and much smaller than the donor signals at 2.4 and 1.4 T. For the field

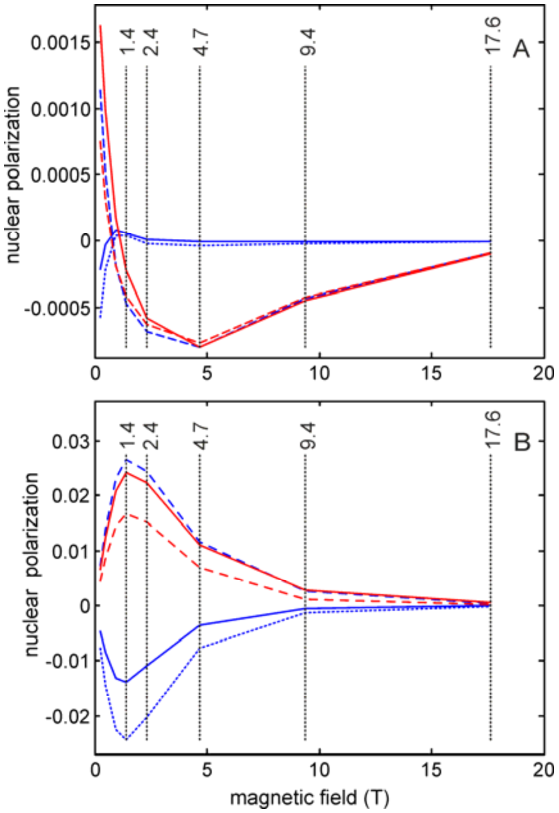

Figure 3.16. Simulated field dependence of donor nuclear polarization for selected nuclei of WT (A) and R26 (B) RCs of *Rb. sphaeroides*, with $T_{1\mathrm{T}} = 22.2\cdot(17.6\ \mathrm{T}/B_0)^{0.69}$ ns and triplet ΔA_k from a DFT computation with the BLYP functional without geometry optimization of the crystal structure. Blue lines correspond to the L moiety, $\mathrm{P_L}^4$ solid line, $\mathrm{P_L}^{14}$ dashed, $\mathrm{P_L}^{15}$ dotted. Red lines correspond to the M moiety. $\mathrm{P_M}^{10}$ solid, $\mathrm{P_M}^{16}$ dashed. Black dotted vertical lines denote fields were measurements were performed.

dependence of acceptor nuclear polarization due to the TSM and DD mechanisms, see Figure 3.17 B.

A quantitative comparison of the experimental and simulated field dependence of the signal intensity is hampered by the fact that the experimental intensities at low fields cannot reliably be normalized. Signal-to-noise ratio for the reference signal in the dark spectrum is poor already at 4.7 T, very poor at 2.4 T, and the signal is not detected in the spectrum without decoupling at 1.4 T.

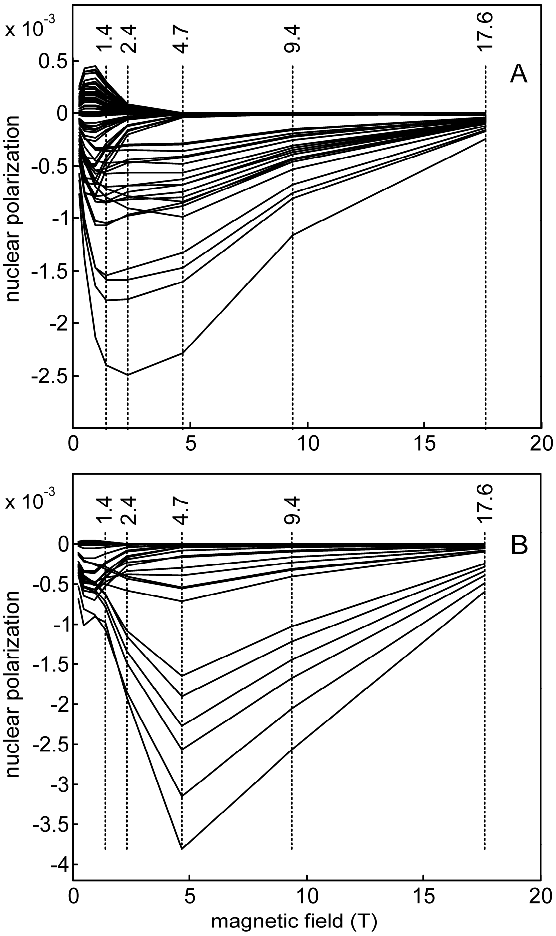

Figure 3.17. Simulated field dependence of donor nuclear polarization in the absence of differential relaxation, *i.e.*, for infinite T_{1T}, (A) and acceptor nuclear polarization (B) for RCs of *Rb. sphaeroides*. Dashed vertical lines denote fields where measurements are performed. Since neither of these simulations depends significantly on the triplet state lifetime τ_T, they apply to both R26 and WT RCs.

3.5 *Discussion*

3.5.1 *Triplet spin densities*

The conclusions on the electronic structure of the special pair triplet depend on the scaling of nuclear longitudinal relaxation times with the ΔA_k^2 suggested by the Redfield-regime expression in Eq. (3.1). The condition $\Delta A_k << 2\ \omega_I$ for the simplified Redfield theory is valid at 9.4 T, with $2\omega_I/\Delta A_k > 12$ for all nuclei. Hence, the data shown in Figure 3.10 provide convincing evidence for an approximately symmetric distribution of spin density over the two moieties of the special pair, as opposed to a strongly biased one.

The slightly asymmetric spin density distribution suggested in Figure 3.7 on the basis of a DFT computation is in line with the experimental data. Observation of the DR effect, and thus any conclusion on a ΔA_k in the triplet state, depends on significant RPM polarization for this nucleus. This in turn requires at least a moderate hyperfine coupling of this nucleus in the radical pair state. This condition is fulfilled for all nuclei whose signals are assigned in Figure 3.10 or 3.13. The corresponding circles for the ΔA_k in the triplet state are shown in black in Figure 3.7. For the nuclei where these circles are shown in gray, the corresponding CIDNP signal was not yet identified and hence, no experimental information on the ΔA_k is available.

Given the uncertainties in estimating $T_{1\mathrm{T}}$ (*vide supra*) and the remaining differences between experimental data and DFT simulations of the spectra, the hyperfine anisotropies ΔA_k listed in Table 3.1 should be considered as approximate. However, the distribution implied by the black circles in Figure 3.7 is expected to be semi-quantitatively correct, since spin dynamics is very sensitive to relative hyperfine couplings within the field range of more than one order of magnitude that is studied here, and the agreement between experiment and simulation is good throughout this field range (Figure 3.14).

In a simple picture, the electron spin density of the ^{3}P state can be rationalized in terms of a linear combination of a single-electron occupied HOMO and a single-electron occupied LUMO. Since the electron spin density in the radical cation state, which is related to the HOMO, has been demonstrated to be shifted to the L cofactor[4,25,51], our data suggest that the LUMO is somewhat shifted to the M cofactor. This is in line with results from Stark spectroscopy[52,53] and the tentative interpretation of results from ^{1}H ENDOR spectroscopy on ^{3}P.[54,23] In Figure 3.7, the gray circles correspond to atoms that should have significant LUMO electron density and small HOMO electron density.

3.5.2 *Longitudinal relaxation times of the nuclei and of the electron spin in the donor triplet state.*

The empirical power law $T_{1\mathrm{T}} = 22.2\cdot(17.6\ \mathrm{T}/B_0)^{0.69}$ ns, together with the Redfield-regime expression, Eq. (3.1), provide a good global fit of the photo-CIDNP data over more than one order of magnitude variation in the external magnetic field and qualitative agreement with the observed trends in signal intensity for R26 and WT RCs. The longitudinal relaxation times of the electron spins in the donor triplet predicted by Eq. 3.1 at a nominal temperature of 235 K are within an order of magnitude of the $T_{1\mathrm{T}}$ measured at 0.35 T by Hoff *et al.* along the y direction of the zero-field splitting tensor at 233 K.[47] This answers the long standing question[46] whether the DR mechanism in the solid state, as originally suggested by Goldstein and Boxer,[22] is a consistent explanation for the enhanced absorptive signals observed in *Rb. sphaeroides* R26 photosynthetic RCs.

3.5.3 *Field dependence of the solid-state photo-CIDNP mechanisms*

For photosynthetic RCs of the carotenoid-less R26 strain of *Rb. sphaeroides*, maximum polarization enhancement by the DR mechanism appears predominant at low field and occurs at lower fields than for the TSM and DD mechanisms. In addition, the optimum field for DR enhancement in WT RCs is lower than for R26.

For practical applications, the optimum field for polarization enhancement depends on the information that one seeks in the NMR spectra. If chemical shift assignments and magnetic parameters in the paramagnetic states with atomic resolution are requested, values of signal-to-noise ratio have to be compared at the same chemical shift resolution. This is possible, since in any spectroscopy sensitivity can be traded for resolution by deconvolution-convolution techniques, as they are applied to the spectrum shown in Figure 3.13. In this case, polarization enhancement for R26 RCs with dominating DR effect is optimal at fields between 4.7 and 9.4 T.

In other cases it may be sufficient to detect and roughly assign the polarization enhanced signals. Sensitivity is then proportional to $pB_0^{1/2}$, where p is the nuclear polarization. For R26 RCs, the optimum is then achieved at fields between 1.4 and 2.4 T.

Polarization enhancement with respect to thermal equilibrium polarization scales with p/B_0 because thermal equilibrium polarization in the high temperature approximation linearly scales with the transition frequency and thus with B_0. This parameter increases with decreasing field for all nuclei within the whole field range $B_0 > 0.25$ T that is simulated. Note however that the field dependence of this enhancement is of practical relevance only if contrast between polarization enhanced and thermal equilibrium signals needs to be optimized.

3.5.4 *Photo-CIDNP MAS NMR as enhancement method for solid-state NMR*

It is already shown here that the high-field TSM and DD mechanisms acting in RCs of *Rb. sphaeroides* show -as it is expected for a mechanism based on a matching condition[2]- a maximum, which is around 2 T. The maximum effect might well be encountered at lower fields for other electron transfer systems which may have weaker ^{13}C hyperfine couplings or smaller *g* value differences. In fact, the only observation of the solid-state photo-CIDNP effect in a non-photosynthetic system, a mutated blue-light photoreceptor, (see chapter 4) was achieved in a relatively low field of 2.4 T. Hence, application of lower fields might be a key to develop photo-CIDNP MAS NMR based on TSM and DD into a more generally applicable method for signal enhancement in solid-state NMR.

The main difficulty with such an approach is a loss of chemical shift resolution at lower fields, which is equivalent to a loss in effective sensitivity (*vide supra*). This problem could be circumvented by polarizing at lower fields than detecting, which requires shuttling of the sample between regions of the magnet with different field.[55,56] General application of solid-state photo-CIDNP would require artificial electron transfer systems which could be applied to surfaces and cavities in 'spin-torch' experiments in which the photo-CIDNP is transferred to explore the environment.

The simulations indicate that much stronger nuclear polarization can be obtained with optimized DR conditions than for the TSM and DD mechanisms (Figure 3.16). This is plausible, since the TSM and DD mechanisms depend on electron-nuclear spin state mixing near an avoided level crossing, which cannot be optimized for all nuclei at the same time and for a second matching condition, which cannot be controlled. This second matching is between the time scales of radical pair decay and hyperfine evolution for the DD mechanism or the electron Zeeman difference frequency and nuclear Zeeman frequency for the TSM mechanism.

In contrast, the DR mechanism depends on RPM polarization, which can lead to values of p of the order of unity. This polarization is completely retained in the ground state if nuclear spin longitudinal relaxation in the triplet state is much faster than triplet decay. The simulations demonstrate that this situation can be attained for many nuclei in R26 RCs at fields lower than 2.4 T. Hence, it appears feasible to achieve high absolute polarization of several percent also for artificial systems.

References

(1) Zysmilich, M. G.; McDermott, A. *J. Am. Chem. Soc.* **1994**, *116*, 8362-8363.

(2) Jeschke, G.; Matysik, J. *Chem. Phys.* **2003***, 294***,** 239-255.

(3) Daviso, E.; Jeschke, G.; Matysik, J. in *Biophysical Techniques in Photosynthesis II* (Aartsma T.J., Matysik, *J., eds.), Springer Dordrecht, pp. 385-399* (2008).

(4) Prakash, S.; Alia; Gast, P.; de Groot, H. J. M.; Jeschke, G.; Matysik, J. *J. Am. Chem. Soc.* **2005**, *127*, 14290-14298.

(5) Prakash, S.; Alia; Gast, P.; de Groot, H. J. M.; Matysik, J.; Jeschke, G. *J. Am. Chem. Soc.* **2006**, *128*, 12794-12799.

(6) Janssen, G. J.; Daviso, E.; van Son, M.; de Groot, H. J. M.; Alia, A.; Matysik, J. *Photosynth. Res.* **2010**, *104*, 275-282.

(7) Matysik, J.; Alia, Gast, P.; van Gorkom, H. J.; Hoff, A. J.; de Groot. H. J. M. *Proc. Natl. Acad. Sci. USA*. **2000**, *97*, 9865-9870.

(8) Alia; Roy, E.; Gast, P.; van Gorkom, H. J.; de Groot, H. J. M.; Jeschke, G.; Matysik, J. *J. Am. Chem. Soc.* **2004**, *126*, 12819-12826.

(9) Diller, A.; Roy, E.; Gast, P.; van Gorkom, H. J.; de Groot, H. J. M.; Glaubitz, C.;Jeschke, G.; Matysik, J. Alia, A. *Proc. Natl. Acad. Sci. U. S. A.* **2007**, *104*, 12767-12771.

(10) Roy, E., Alia, Gast, P.; van Gorkom, H. J.; de Groot, H. J. M.; Jeschke, G.; Matysik, J. *Biochem. Biophys. Act.* **2007**, *1767*, 610–615.

(11) Roy, E.; Rohmer, T.; Gast, P.; Jeschke, G.; Alia, A.; Matysik, J. *Biochemistry* **2008**, *47*, 4629-4635.

(12) Matysik, J.; Diller, A.; Roy, E.; Alia, A. *Photosynth. Res.* **2009**, *102*, 427-435.

(13) Daviso, E.; Alia, A.; Prakash, S.; Diller, A.; Gast, P.; Lugtenburg, J.; Jeschke, G.; Matysik, J. *J. Phys. Chem. C* **2009**, *113*, 10269-10278.

(14) Hoff, A. J.; Deisenhofer, J. *Phys. Rep.* **1997**, *287*, 2-247.

(15) Hunter, C. N.; Daldal, F.; Thurnauer, M. C.; Beatty, J. T. *The Phototropic Purple Bacteria* in *Advances in Photosyntheis and Respiration* (Series editor Govindjee)*, Springer Dordrecht, Volume 28* (2008).

(16) Jeschke*,* G. *J. Chem. Phys.* **1997**, *106*, 10072-10086.

(17) Jeschke, G. *J. Am. Chem. Soc.* **1998**, *120*, 4425-4429.

(18) Polenova, T.; McDermott, A. E. *J. Phys. Chem. B.* **1999**, *103*, 535-548.

(19) Closs, G. L.; Closs, L. E. *J. Am. Chem. Soc*. **1969**, *91*, 4549-4550.

(20) Kaptein, R.; Oosterhoff, J. L. *Chem. Phys. Lett.* **1969**, *4*, 195-197.

(21) Closs, G. L. *Chem. Phys. Lett.* **1975**, *32*, 277-278.

(22) Goldstein, R. A.; Boxer, S. G. *Biophys. J.* **1987**, *51*, 937-946.

(23) Marchanka, A.; Paddock, M.; Lubitz, W.; van Gastel, M. *Biochemistry* **2007**, *46*, 14782-14794.

(24) Marchanka, A.; Savitsky, A.; Lubitz, W.; Möbius, K.; van Gastel, M. *J. Phys. Chem. B* **2010**, *114*, 14364-14372.

(25) Daviso, E.; Prakash, S.; Alia, A.; Gast, P.; Neugebauer, J.; Jeschke, G.; Matysik, J. *Proc. Natl. Acad. Sci. USA*. **2009**, *106*, 22281-22286.

(26) Diller, A.; Prakash, S.; Alia, A.; Gast, P.; Matysik, J.; Jeschke, G. *J. Phys. Chem. B*. **2007**, *111*, 10606-10614.

(27) Abragam, A. *Principles of Nuclear Magnetism*, *Oxford University Press*, (1962).

(28) Jeschke, G.; Anger, B. C.; Bode, B. E.; Matysik, J. *J. Phys. Chem. A.* **2011**, *115*, 9919-9928.

(29) Shochat, S.; Arlt, T.; Francke, C.; Gast, P.; Vannoort, P. I.; Otte, S. C. M.; Schelvis, H. P. M.; Schmidt, S.; Vijgenboom, E.; Vrieze, J.; Zinth, W.; Hoff, A. J. *Photosyn. Res.* **1994**, *40*, 55-66.

(30) Feher, D.; Okamura, M. Y. In *The Photosynthetic Bacteria;* Clayton, R. K., Siström, W., Eds.; Plenum Press: New York, 1978; p 349-378.

(31) Okamura, M. Y.; Isaacson, R. A.; Feher, G. *Proc. Natl. Acad. Sci. U.S.A.* **1975**, *72*, 3491-3495.

(32) Fischer, M. R.; de Groot, H. J. M.; Raap, J.; Winkel, C.; Hoff, A. J.; Lugtenburg, J. *Biochemistry* **1992**, *31*, 11038-11049.

(33) Bennett, A. E.; Rienstra, C. M.; Auger, M.; Lakshmi, K. V.; Griffin, R. G. *J. Chem. Phys.* **1995**, *103*, 6951-6958.

(34) Zhang, S.; Wu, X.; Mehring, M. *Chem. Phys. Lett.* **1990**, *173,* 481-484.

(35) Matysik, J.; Alia; Hollander, J. G.; Egorova-Zachernyuk, T.; Gast, P.; de Groot, H. J. M. *Indian J. Biochem. Biophys.* **2000**, *37*, 418-423.

(36) te Velde, G.; Bickelhaupt, F. M.; van Gisbergen; S. J. A.; Fonseca Guerra, C.; Baerends, E. J.; Snijders, J. G.; Ziegler, T. J. Comput. Chem. 2001, 22, 931.

(37) ADF2004.01, SCM, Theoretical Chemistry, Vrije Universiteit, Amsterdam, The Netherlands, http://www.scm.com

(38) Becke, A. D. *Phys. Rev. A* **1988**, *38*, 3098.

(39) Lee, C.; Yang, W.; Parr, R. G. *Phys. Rev. B* **1988**, *37*, 785.

(40) Stowell, M. H.; McPhillips, T. M.; Rees, D. C.; Soltis, S. M.; Abresch, E.; Feher, G. *Science* **1997**, *276*, 812-816.

(41) ADF2009.01, SCM, Theoretical Chemistry, Vrije Universiteit, Amsterdam, The Netherlands, http://www.scm.com

(42) Dunning, T. H. Jr. *J. Chem. Phys.***1989**, *90*, 1007.

(43) Ermler, U.; Fritzsch, G.; Buchanan, S. K.; Michel, H. *Structure* **1994**, *2*, 925-936.

(44) Eichkorn, K.; Treutler, O.; Öhm, H.; Haser, M.; Ahlrichs, R. *Chem. Phys. Lett.* **1995**, *242*, 652.

(45) Eichkorn, K.; Weigend, F.; Treutler, O.; Ahlrichs, R. *Theor. Chem. Acc.* **1997**, *97*, 119.

(46) McDermott, A.; Zysmilich, M. G.; Polenova, T. *Solid State Nuc. Magn. Reson.* **1998**, *11*, 21-47.

(47) Hoff, A. J.; Proskuryakov, I. I. *Chem. Phys. Lett.* **1985**, *115*, 303-310.

(48) Ahlrichs, R.; Bär, M.; Häser, M.; Horn, H.; Kälmel, C. *Chem. Phys. Lett.* **1989**, *162*, 165.

(49) Perdew, J. P.; Wang, Y. *Phys. Rev. B* **1986**, *33*, 8822.

(50) Kaptein, R. *J. Chem. Soc. Chem. Commun.* **1971**, 732-733.

(51) Lendzian, F.; Huber, M.; Isaacson, R. A.; Endeward, B.; Plato, M.; Bönigk, B.; Möbius, K.; Lubitz, W.; Feher, G. *Biochim. Biophys. Acta* **1993**, *1183*, 139-160.

(52) Lockhart, D. J.; Boxer, S. G. *Proc. Natl. Acad. Sci. U. S. A.* **1988**, *85*, 107-11.

(53) Moore, L. J.; Zhou, H.; Boxer, S. G. *Biochemistry* **1999**, *38*, 11949-60.(54) Lubitz, W.; Lendzian, F.; Bittl, R. *Acc. Chem. Res.* **2002**, *35*, 313-320.

(55) Grosse, S.; Gubaydullin, F.; Scheelken, H.; Vieth, H. M.; Yurkovskaya, A. V. *Appl. Magn. Reson.* **1999**, *17*, 211-225.

(56) Ivanov, K. L.; Miesel, K.; Yurkovskaya, A. V.; Korchak, S. E.; Kiryutin, A. S.; Vieth, H. M. *Appl. Magn. Reson.* **2006**, *30*, 513-534.

Chapter 4

Solid-state photo-CIDNP effect observed in phototropin LOV1-C57S by ^{13}C magic-angle spinning NMR spectroscopy

4.1 *Abstract*

Until now, the solid-state photo-CIDNP effect, discovered in 1994 by Zysmilich and McDermott, has been observed exclusively in natural photosynthetic centers. The present work demonstrates the first observation of this effect in another system, the blue-light photoreceptor phototropin LOV1-C57S using ^{13}C magic-angle spinning (MAS) NMR.

This chapter is published in *J. Am. Chem. Soc.*, 2010, 132 (44), pp 15542–15543.

4.2 *Introduction*

4.2.1 *The solid state photo-CIDNP effect*

The solid-state photochemically induced dynamic nuclear polarization (photo-CIDNP) effect was observed for the first time in 1994 by McDermott's group in frozen and quinone-blocked bacterial RCs of ^{15}N-labeled *Rb. sphaeroides* R26 by MAS NMR.[1] The effect allows for enhancement of NMR signals by a factor of more than 10,000 due to non-Boltzmann nuclear polarization.[2,3] Since then, the effect has also been shown in various other RCs including those of algae[4] and plants,[5,6] and even at a cellular level for RC-antenna complexes when in the

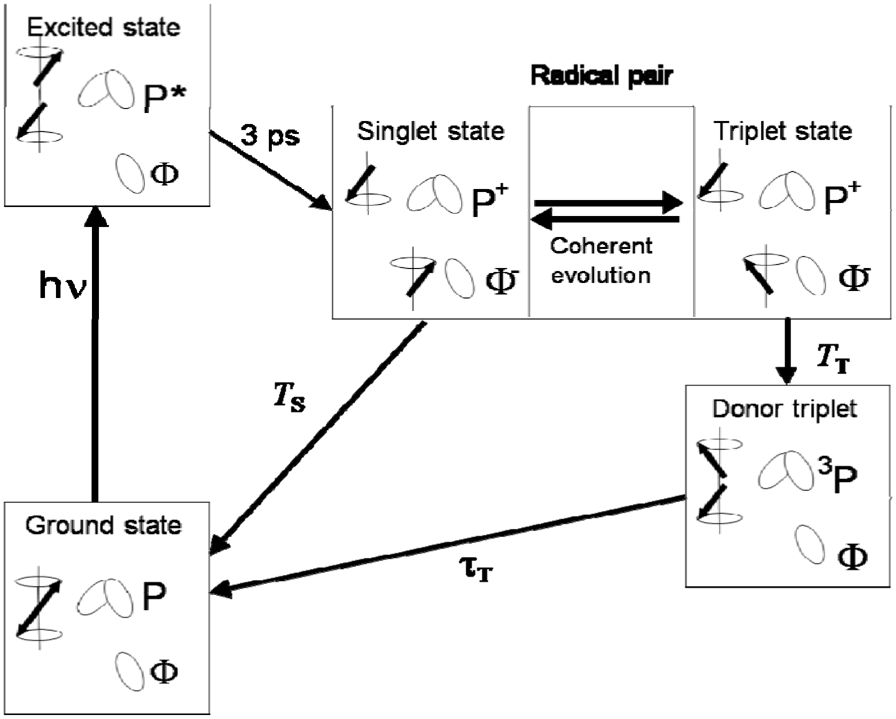

Figure 4.1.Photocycle in quinone-depleted RCs of *Rb. sphaeroides* WT and R26. Upon illumination and fast electron transfer from an excited singlet state, a radical pair is formed in a pure singlet state having high electron spin order. The radical pair is formed by a radical cation at the two donor BChls (Special pair, P) and a radical anion on the BPhe acceptor cofactor (Φ) of the active branch. The chemical fate of the radical pair depends on its electronic spin state: the singlet state is allowed to recombine with the lifetime of T_S= 20 ns and this recombination pathway is termed singlet channel. For the triplet state a direct recombination is spin-forbidden and a donor triplet (^{3}P) is formed with a lifetime of T_T= 1 ns. The lifetime of the donor triplet state (τ_T) is 100 ns for WT RCs and 100 μs for R26 RCs. The recombination pathway of the donor triplet to the ground state is termed triplet channel. Mechanisms building up photo-CIDNP under steady-state conditions are TSM, DD and DR.

membrane, in the natural environment.[3,4] Several attempts were made to observe polarization in other proteins, however, other systems with photoreaction kinetics that allows for the observation of the photo-CIDNP effect were not yet identified.[7] Here we demonstrate that the solid-state photo-CIDNP effect can also be observed in a rather different, non-photosynthetic protein, a mutant of the light-, oxygen-, or voltage-sensitive (LOV) domain of the blue-light photoreceptor phototropin. Signals were recorded from the flavin cofactor without isotopic enrichment.

Photo-CIDNP is well known in solution NMR and was explained by the radical pair mechanism (RPM) soon after its discovery in 1969. [8,9] The classical RPM in solution is based on molecular diffusion. The solid-state photo-CIDNP effect is interpreted by up to three mechanisms running in parallel,[10] three-spin mixing (TSM),[11] differential decay (DD),[12] and differential relaxation (DR)[13] (Figure 4.1), which allow for the conversion of the initial electron-spin zero quantum coherence of the spin-correlated radical pair[14] into nuclear polarization by symmetry breaking. In illuminated RCs, an electron is transferred from the excited electron-donor P^* to a primary acceptor Φ forming an spin correlated radical pair, initially in singlet state $^1(P^{+\bullet}\,\Phi^{-\bullet})$ and it converts to triplet state $^3(P^{+\bullet}\,\Phi^{-\bullet})$ and back by coherent evolution. The high electron spin order of initial singlet state is transferred to net nuclear polarization by two parallel and competing mechanism termed TSM[11] and DD[12]. The TSM mechanism is explained by the combined action of electron-electron dipolar coupling or exchange coupling, the nuclear Zeeman interaction and the pseudosecular hyperfine coupling (hfc) $B = (A_{zx}^2 + A_{zy}^2)^{1/2}$. This breaks the antisymmetry of $\langle I_z \rangle$nuclear spin population in coherent spin evolution of the spin correlated radical pair. The different lifetimes of singlet (T_S) and triplet states (T_T) breaks the antisymmetry of the nuclear spin population in the spin correlated radical pair by a buildup of net nuclear polarization via the B in a DD mechanism. In cyclic reactions, net nuclear polarization can occur if the products have different nuclear longitudinal relaxation rates. Such a type of RPM can also occur in solids, as in frozen R26 RCs having a long-lived donor triplet state, and is called the DR mechanism.

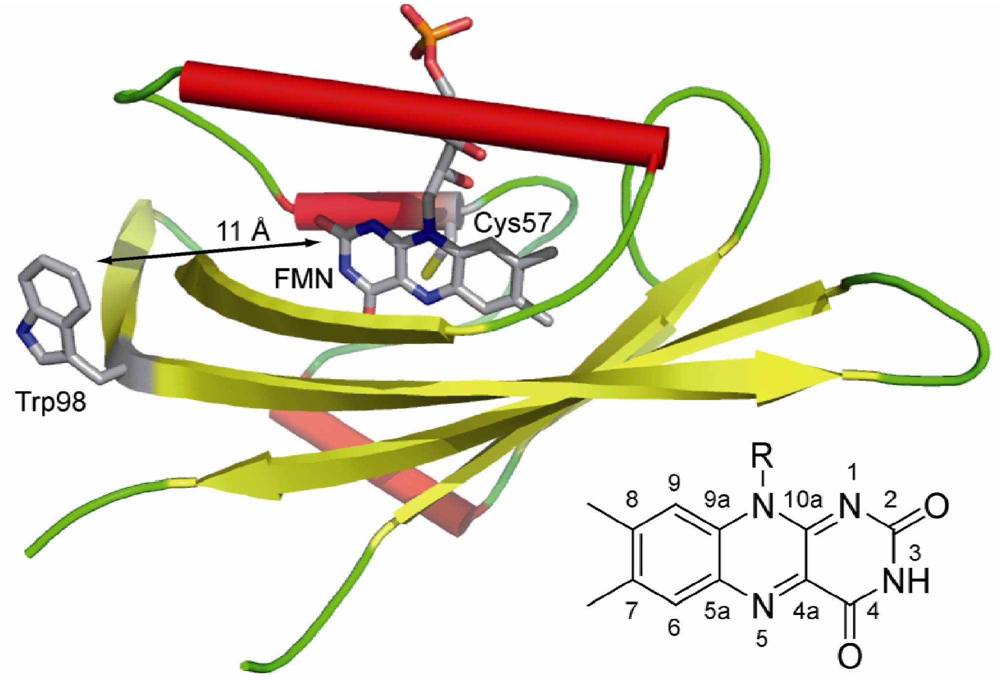

Figure 4.2: Structure of the phototropin LOV1 domain in the dark (PDB 1N9L).[15] Cysteine 57 was replaced by serine in this study. The numbering of the flavin chromophore is included.

4.1.2 *Phototropin LOV1-C57S*

Phototropin is a member of the family of flavin-containing blue-light photoreceptors and regulates key responses of plants to light, such as phototropic movement and chloroplast relocation.[16]Phototropin comprises two LOV domains, each binding non-covalently a flavin mononucleotide (FMN), and a kinase domain. Upon illumination, the triplet excited state of the flavin reacts with a nearby cysteine residue to form a covalent adduct as the signaling state.[17] Mutation of the reactive cysteine to serine or alanine abolishes this adduct formation. Instead, a less efficient competing pathway of electron transfer from a tryptophan leads to transient accumulation of a flavin anion radical on illumination[18,19] and finally to formation of a flavin neutral radical.[20] The radical is re-oxidized by oxygen. We investigated the mutant, C57S, of the phototropin-LOV1 domain from the green alga *Chlamydomonas reinhardtii* (Figure 4.2). [21]

4.3 *Materials and Methods*

4.3.1 *LOV1 expression and purification*

The C57S mutant of the LOV1 domain (amino acids 16-133) of *Chlamydomonas reinhardtii* was expressed in *E. coli* strain BL21(DE3) carrying an N-terminal 10x His-tag as described before.[21] The cells were disintegrated using a French Press and the protein was purified via affinity chromatography using His-bind resin (Novagen) loaded with copper sulphate. Protein was transferred into 50 mM potassium phosphate, pH 8, containing 300 mM NaCl by repeated ultrafiltration using an Amicon Ultra-15 filter device with a 10 kDa cutoff (Millipore). The final solution was concentrated to an optical density of ~20 at 450 nm (optical path length, 1 cm).

4.3.2 *MAS NMR experiment*

An Avance 100 MHz spectrometer equipped with 4-mm MAS probe (Bruker, Karlsruhe, Germany) was used for the ^{13}C MAS NMR experiments both in the dark and using continuous illumination with white light. The sample was packed into a 4-mm sapphire rotor and inserted into the MAS probe. For a homogeneous sample distribution against the rotor wall, the sample was frozen at a very low spinning frequency of 500 Hz.[22] The spinning frequency was increased to 8 kHz after the sample is completely frozen at 235 K. This frequency and set temperature were used for all ^{13}C MAS NMR measurements. A simple Hahn echo pulse sequence[23] with TPPM proton decoupling[24] was used for all NMR measurements. A cycle delay of 2 s was used for all NMR experiments and signals were accumulated for 12 h. An artificial line-broadening of 10 Hz was applied before Fourier transformation. All ^{13}C MAS NMR spectra were calibrated with respect to the ^{13}COOH chemical shift of solid tyrosine.HCl at 172.1 ppm. The same phase-correction parameters required to properly phase a tyrosine spectrum were used for the dark and photo-CIDNP spectra.

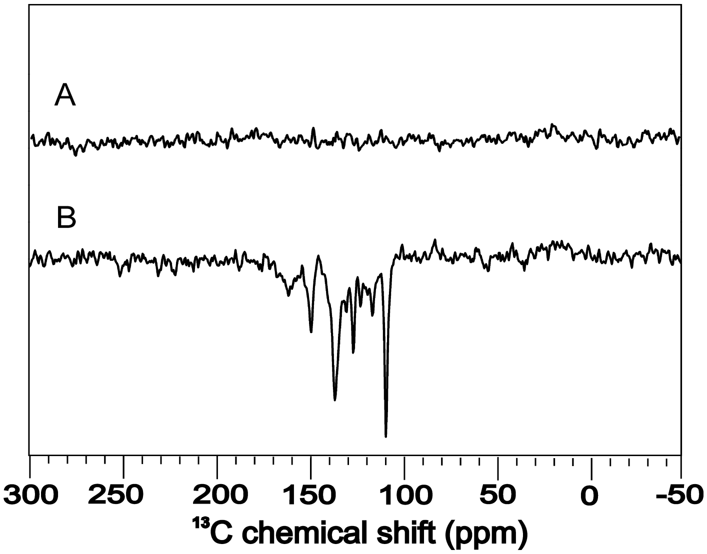

Figure 4.3.^{13}C MAS NMR spectra of phototropin LOV1-C57S obtained with 8 kHz MAS in a magnetic field of 2.3 T in the dark (A) and using continuous illumination with white light (B).

4.4 *Results and discussion*

4.4.1 *Comparison of Photo-CIDNP and dark MAS NMR spectra*

In Figure 4.3, the ^{13}C MAS NMR spectra of phototropin LOV1-C57S obtained in the dark (A) and with illumination (B) are shown. Both datasets were measured at 2.3 T (*i.e.*, 100 MHz ^{1}H frequency) using a spinning frequency of 8 kHz. At a set temperature of 235 K, the sample was entirely frozen as monitored by the NMR tuning frequency. A simple Hahn-echo pulse sequence with two-pulse phase-modulation protondecoupling was used. Continuous illumination was supplied by a 1 kW xenon lamp.[23] The cycle delay was 2 s and the measurement time was about 12 h. In the dark no resonance signal was detected but under illumination several strong signals appear in the aromatic region.

An enlarged view of the aromatic region of the solid-state photo-CIDNP spectrum is presented in Figure 4.4. All light-induced ^{13}C NMR peaks are emissive (negative). This pattern is reminiscent of the photo-CIDNP MAS NMR spectra obtained from RCs of *Rb. sphaeroides* WT[2] and of photosystem I[5] and contrasts

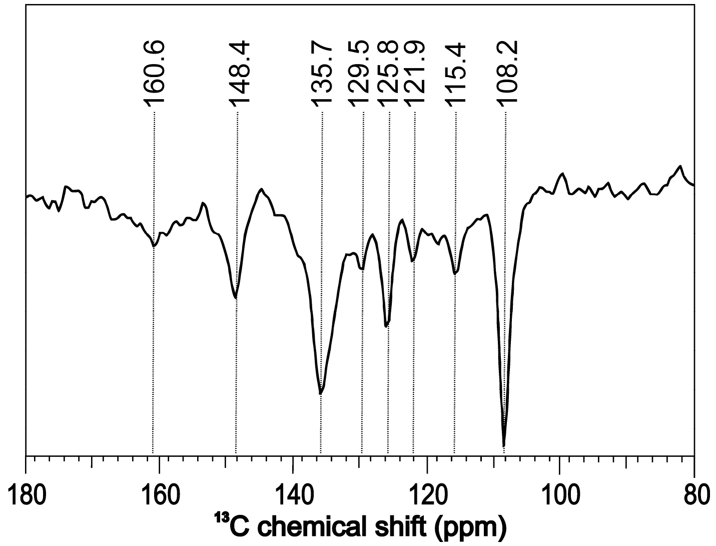

Figure 4.4. Expanded view on the aromatic region of the ^{13}C MAS NMR spectrum of phototropin LOV1-C57S showing the solid-state photo-CIDNP effect (Spectrum 4.3B).

with the mixed absorptive/emissive enhancement pattern observed by photo-CIDNP of a LOV2 sample in solution.[19]

4.3.2 *Preliminary assignments of light induced ^{13}C signals*

A preliminary assignment of these peaks can be obtained by comparison with the ^{13}C chemical shifts of FMN in solution and in the LOV2 domain of *Avenasativa* phototropin obtained by ^{13}C liquid-state NMR (Table 4.1). Six of the eight light-induced signals can be assigned to the ten aromatic carbons in the FMN cofactor, with four pairs of overlapping resonances (C2 and C4, C5a and C9a, C6 and C9, C7 and C8). The two additional signals at 108.2 and 115.4 ppm appear upfield of the others and probably do not arise from FMN. As known from solid-state photo-CIDNP studies on RCs, polarized signals are observed from both the electron-donor and the electron-acceptor. Hence, we assume that at least these two signals arise from the electron-donor in the spin-correlated radical pair. In fact, the

	^{13}C chemical shift in ppm			
	Free FMN in D_2O solution[a]	FMN bound to LOV2 in the dark[b]	FMN bound to LOV2 under illumination[b]	FMN bound to LOV1-C57S under illumination[c]
2	159.8	159.2	159.3	160.6
4	163.7	161.0	165.9	160.6
4a	136.2	134.5	65.0	129.5
5a	136.4	136.3	130.3	125.8
6	131.8	132.8	120.7	121.9
7	140.4	139.0	130.3	135.7
8	151.7	150.7	136.2	135.7
9	118.3	119.3	118.7	121.9
9a	133.5	134.2	127.7	125.8
10a	152.1	150.8	156.9	148.4

[a] ref. 25.

[b] LOV2 domain of *Avena sativa* phototropin reconstituted with [u-^{13}C^{15}N]-FMN, ref.26.

[c] This work.

Table 4.1. Preliminary assignment of ^{13}C chemical shifts of FMN in LOV1-C57S.

two peaks can be attributed to C^{γ} and $C^{\zeta 2}$ of a tryptophan residue (Trp) (Table 4.2), [27] while no match for the resonance at 108.2 ppm would be expected from the two other possible electron donors, histidine and tyrosine. Hence, the data can be reconciled with observed nuclear polarization originating from a light-induced [$FMN^{-\bullet}Trp^{+\bullet}$] radical pair. Trp at position 98 (Figure 4.1), the only Trp in the protein, is about 11 Å edge-to-edge distance from FMN and, thus, at a suitable distance for efficient electron transfer.

Carbon number	**^{13}C chemical shift in ppm**	
	Trp^{a}	Trp^{b}
C	176.18	-
C^{α}	57.71	-
C^{β}	29.97	-
C^{γ}	110.6	108.2
$C^{\delta 1}$	126.5	125.8
$C^{\delta 2}$	127.49	129.5
$C^{\varepsilon 2}$	138.62	135.7
$C^{\varepsilon 3}$	120.46	121.9
$C^{\zeta 2}$	114.23	115.4
$C^{\zeta 3}$	121.40	121.9
$C^{\eta 2}$	123.83	121.9

[a] ref.27
[b] This work

Table4.2. ^{13}C chemical shifts of Tryptophan (Trp)

4.4 *Conclusion*

The data presented in this Chapter provide a first experimental demonstration that the solid-state photo-CIDNP effect is not only a peculiarity of photosynthetic systems but can arise in at least one other photo-active protein. In the same way that photo-CIDNP MAS NMR has provided detailed insights into photosynthetic electron transport in RCs, [1-7] a variety of applications in studies of the functionality of blue-light photoreceptors can be anticipated. For example, it may be possible to characterize in detail the photo-induced flavin and tryptophan radicals in cryptochrome, the flavoprotein that has been proposed as the radical pair magnetoreceptor for the avian magnetic compass.[29]

References

(1) Zysmilich, M. G.; McDermott, A. *J. Am. Chem. Soc.***1994**, *116*, 8362-8363.

(2) Prakash, S.; Alia; Gast, P.; de Groot, H. J. M.; Jeschke, G.; Matysik, J. *J. Am. Chem. Soc.***2005**, *127*, 14290-14298.

(3) Prakash, S.; Alia; Gast, P.; de Groot, H. J. M.; Matysik, J.; Jeschke, G. *J. Am. Chem. Soc.***2006**, *128*, 12794-12799.

(4) Janssen, G. J.; Daviso, E.; van Son, M.; de Groot, H. J. M.; Alia, A.; Matysik, *J. Photosynth. Res.* **2010**, *104*, 275-282.

(5) Alia; Roy, E.; Gast, P.; van Gorkom, H. J.; de Groot, H. J. M.; Jeschke, G.; Matysik, J. *J. Am. Chem. Soc.* **2004**, *126*, 12819-12826.

(6) Diller, A.; Roy, E.; Gast, P.; van Gorkom, H. J.; de Groot, H. J. M.; Glaubitz, C.;Jeschke, G.; Matysik, J. Alia, A. *Proc. Natl. Acad. Sci. U. S. A.***2007**, *104*, 12767-12771.

(7) Matysik, J.; Diller, A.; Roy, E.; Alia, A. *Photosynth. Res.* **2009**, *102*, 427-435.

(8) (a) Closs, G. L.; Closs, L. E. *J. Am. Chem. Soc.* **1969**, *91*, 4549-4550. (b) Kaptein, R.; Oosterhoff, J. L. *Chem. Phys. Lett.***1969**, *4*, 195-197.

(9) (a) Bargon, J.; Fischer, F.; Johnson, U. *Z. Naturforsch.A* **1967**, *22*, 1551-1555. (b) Ward, H. R.; Lawler, R. G. *J. Am. Chem. Soc.***1967**, *89*, 5518-5519.

(10) (a) Daviso, E.; Jeschke, G.; Matysik, J. *J. Phys. Chem. C* **2009**, *113*, 10269-10278. (b) Jeschke, G.; Matysik, J. *Chem. Phys.***2003**, *294*, 239-255. (c) Daviso, E.; Jeschke, G.; Matysik, J. In *BiophysicalTechniques in Photosynthesis II*; Aartsma T.J., Matysik, J., eds.; Springer: Dordrecht, 2008; pp. 385-399.

(11) Jeschke, G. *J. Chem. Phys.***1997**, *106*, 10072-10086.

(12) Polenova, T.; McDermott, A. E. *J. Phys. Chem. B.***1999**, *103*, 535-548.

(13) (a) Closs, G.L. *ChemPhysLett***1975**, *32*, 277-278 (b) Goldstein, R. A.; Boxer, S. G. *Biophys J* **1987,***51*, 937-946. (c) McDermott, A.; Zysmilich, M. G.; Polenova, T. *Solid State Nuc. Magn. Reson.***1998**, *11*, 21-47.

(14) (a) Hore, P. J.; Hunter, D. A.; McKie, C. D.; Hoff, A. J. *Chem. Phys. Lett.***1987**, *137*, 495-500. (b) Closs, G. L.; Forbes, M. D. E.; Norris, J. R. *J. Phys.Chem.***1987**, *91*, 3592-3599.

(15) Fedorov, R.; Schlichting, I; Hartmann, E.; Domratcheva, T.; Fuhrmann, M.; Hegemann, P. *Biophys. J.***2003**, *84*, 2474-2482.

(16) (a) Christie, J. M. *Annu. Rev. Plant Biol.***2007**, *58*, 21-45. (b) Christie, J. M.; Reymond, P.; Powell, G. K.; Bernasconi, P.; Raibekas, A. A.; Liscum, E.; Briggs, W. R. *Science***1998**, *282*, 1698-1701.

(17) Salomon, M.; Christie, J. M.; Knieb, E.; Lempert, U.; Briggs, W. R. *Biochemistry***2000**, *39*, 9401-9410.

(18) Richter, G.; Weber, S.; Römisch, W.; Bacher, A.; Fischer, M.; Eisenreich, W. *J. Am. Chem. Soc.***2005**, *127*, 17245-17252.

(19) Eisenreich, W.; Joshi, M.; Weber, S.; Bacher, A.; Fischer, M. *J. Am. Chem. Soc.***2008**, *130*, 13544-13545.

(20) (a) Kay, C. W.; Schleicher, E.; Kuppig, A.; Hofner, H.; Rudiger, W.; Schleicher, M.; Fischer, M.; Bacher, A.; Weber, S.; Richter. G. *J. Biol. Chem.***2003**, *278*, 10973-10982. (b) Kottke, T.; Dick, B.; Fedorov, R.; Schlichting, I.; Deutzmann, R.; Hegemann, P. *Biochemistry***2003**, *42*, 9854-9862.

(21) Kottke, T.; Heberle, J.; Hehn, D.; Dick, B.; Hegemann, P. *Biophys. J.***2003**, *84*, 1192-1201.

(22) Fischer, M. R.; de Groot, H. J. M.; Raap, J.; Winkel, C.; Hoff, A. J.; Lughtenburg, J. *Biochemistry***1992**, *31*, 11038-11049.

(23) Matysik. J.; Alia; Hollander, J. G.; Egorova-Zachernyuk, T.; Gast, P.; de Groot, H. J. M. Indian J. *Biochem. Biophys.* **2000**, *37*, 418-423.

(24) Bennett, A. E; Rienstra, C. M.; Auger, M.; Lakshmi, K. V.; Griffin, R. G. *J. Chem. Phys.***1995**, *103*, 6951-6958.

(25) Vervoort, J.; Müller, F.; O'Kane, D. J.; Lee, J.; Bacher, A. *Biochemistry*. **1986**, *25*, 8067-8075.

(26) Salomon, M.; Eisenreich, W.; Dürr, H.; Schleicher, E.; Knieb, E.; Massey, V.; Rüdiger, W.; Müller, F.; Bacher, A.; Richter, G. *Proc. Natl. Acad. Sci. USA*. **2001**, *98*, 12357-12361.

(27) Sun, H.; Oldfield, E. *J. Am. Chem. Soc*. **2004**, *126*, 4726-4734.

(28) http://www.bmrb.wisc.edu

(29) Ritz, T.; Adem, S.; Schulten, K. *Biophys. J.* **2000**, *78*, 707-718.

Chapter 5

Magnetic field dependence of the solid-state ^{13}C photo-CIDNP effect in phototropin LOV1-C57S

5.1 *Abstract*

Recently, the experimental observation of a solid-state photo-CIDNP effect in the C57S mutant of the LOV1 domain of the blue light photoreceptor phototropin was reported [chapter 4]. It was the first description of this effect in a non-photosynthetic photoactive protein. The magnetic field dependence of the effect in the range between 1.4 and 9.6 T is studied here and shows a different range of signal enhancement with maximum at 2.4 T than for photosynthetic RCs. A future theoretical simulation of this field-dependence will test whether the mechanism for origin of solid-state ^{13}C photo-CIDNP effect in phototropin LOV1-C57S can be described in terms of the same mechanisms known to operate in photosynthetic systems.

5.2 *Introduction*

The solid-state photo-CIDNP (photochemically induced dynamic nuclear polarization) effect was discovered in 1994 by Zysmilich and McDermott[1] by studying quinone-blocked photosynthetic reaction centers (RCs) of the purple bacterium *Rhodobacter (Rb.) sphaeroide*s with solid-state magic-angle spinning (MAS) NMR spectroscopy while illuminating the sample. Although the classical radical-pair mechanism (RPM)[2,3] requires diffusion for symmetry breaking, the possibility to observe photo-CIDNP in solids was predicted by Goldstein and Boxer.[4] They recognized that a mechanism known from liquid-state photo-CIDNP can also be operative in solids. This mechanism, called 'cyclic reactions'[5,6] in the liquid-state and 'differential relaxation' (DR) in solid-state NMR,[7,8] the symmetry breaking relies on the difference in the nuclear relaxation kinetics of the chemical product originating from either the singlet or the triplet decay branch of the radical pair. The DR mechanism, however, did not fully explain the experimental observations. Also signals of the acceptor cofactor obtain enhancement, while the difference in relaxation occurs only on the donor during its molecular triplet state. Signal enhancement by optical nuclear polarization (ONP)[9,10] involves selective population of the molecular triplet states (T_0, T_+ and T_-) that leads to electron polarization that is transferred to nuclei. This requires matching the applied magnetic fields with the hyperfine fields in the mT range. Although ONP has been reported for solids, the high field of the NMR magnet provides little prospect for ONP as a possible source of the enhanced polarization.

Therefore, two other mechanisms have been proposed, transferring under solid-state conditions the initial electron-spin order (pure singlet or pure triplet state), occurring upon generation of the radical pair in a non-stationary state, into nuclear polarization. Both mechanisms, called three-spin mixing mechanism (TSM)[11,12] and differential decay (DD)[13] have been described in detail in Chapter 1.

Analysis of the field-dependence[7,14][Chapter 3] and time-evolution[15] in RCs of *Rb. sphaeroides* wild type (WT) and the carotenoid-less mutant R26 allowed for recognition of the enhancement mechanisms. In particular, in Chapter 3, we studied the full field range of the effect from 1.4 to 17.6 T, demonstrating that the effect is

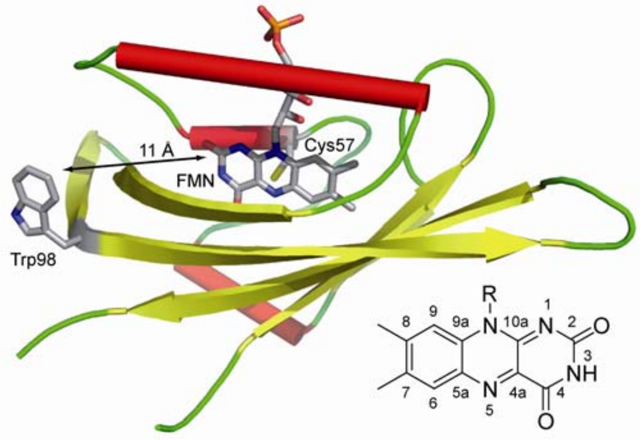

Figure 5.1: Structure of the LOV1 domain of the blue-light receptor phototropin. The flavin cofactor is shown at the bottom.

indeed a matching effect as expected for a TSM and DD based origin. Hence, in WT RCs, the all-emissive (*i.e.* negative) ^{13}C NMR envelope is explained by the dominance of the TSM over the DD in absence of another mechanism.[14] In R26 RCs, the DR occurs in addition to TSM and DD, and allows also for positive signals, mainly from donor signals that are affected by the long-living donor triplet state[8] [Chapter 3].

The effect is also observed in a variety of other natural RCs,[16-19] and the strong enhancement allows for observations directly in membranes[17] and cells.[8,20] The short radical-pair lifetime in RCs, ~20 ns or less, leads to a very limited number of coherent evolution cycles within the radical pair and to broad matching windows[22] which makes photo-CIDNP MAS NMR studies on these systems rather straightforward. The radical pair lifetime of phototropin LOV1-C57S (Figure 5.1) from the alga *Chlamydomonas reinhardtii* can be more than ~100 ns.[21] This leads to a larger number of coherent evolution cycles within the radical pair than for photosynthetic RCs. Assuming that the broad enhancement window as observed in photosynthetic RCs is due to lifetime broadening, the short life times in photosynthetic RCs of ~10 ns translate into a frequency window of ~100 MHz.[22] The field-dependent experiments on the blue-light photoreceptor are expected to show a smaller matching window ~10 MHz corresponding with the longer life time of ~100 ns. In this respect, many radical-pair systems as artificial RCs or other

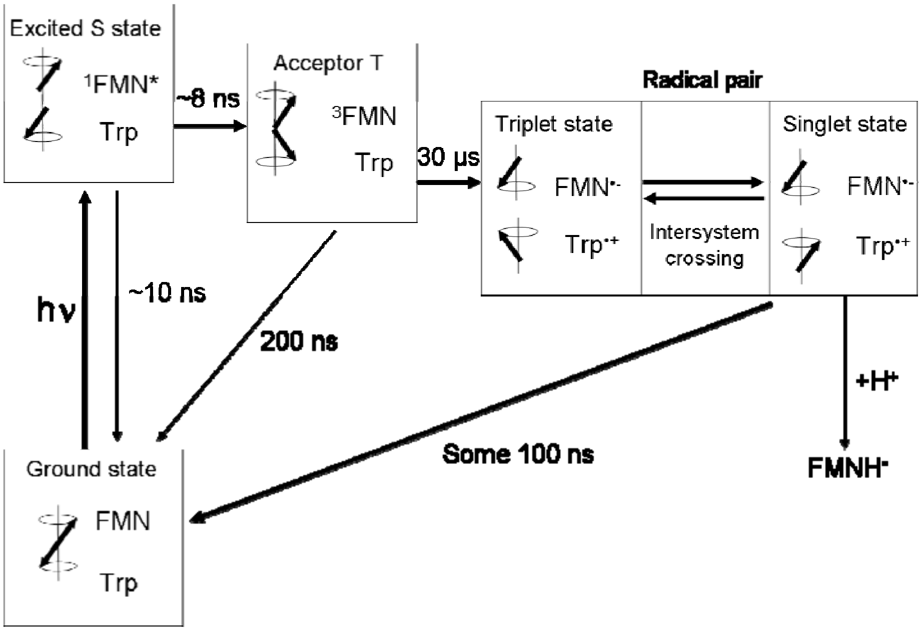

Scheme 5.1: Tentative photocycle in phototropin LOV1-C57S. The initial excited singlet state of the FMN converts into an acceptor triplet state, which is followed by slow electron transfer, on a time scale of ~30 µs to form the correlated radical pair in its non-stationary T_0 state.[21] The radical pair cannot decay via its triplet state but can convert into the singlet state by coherent evolution of the electron-electron zero quantum coherence. The singlet state can decay back to the ground state, which can take more than 100 ns, or it can form a product state $FMNH^+$ by uptake of a proton.

blue-light photoreceptors[23] have correlated radical-pair lifetimes in the µs range, leading to sharp matching windows that make it difficult to detect the photo-CIDNP effect with standard NMR equipment.

The long radical pair lifetime might be the reason why until now, despite extensive of effort, only a single non-photosynthetic system has been discovered that shows the solid-state photo-CIDNP effect [see chapter 4]. A homologous domain, LOV2-C250S from *Avena sativa* phototropin, has shown a CIDNP effect in solution as well.[24,25]

In the wild type LOV domains, illumination of oxidized flavin leads to formation of the triplet excited state. Its reaction with a nearby cysteine residue results in a covalent adduct as the signaling state. In the C57S or C250A mutants, the reactive cysteine has been replaced, which abolishes adduct formation and strongly increases triplet lifetime.[21] Instead, a much less efficient competing pathway of electron transfer from a tryptophan leads to transient accumulation of a flavin anion radical on illumination[24,25] and finally to formation of a flavin neutral radical[26,27] (Scheme 5.1).

Due to the concomitant presence of CIDNP effects in solution and in the solid, the question arises whether the solid-state photo-CIDNP effect can also explained in this system by a solid-state photo-CIDNP mechanism. In an attempt to answer this question, the field-dependent photo-CIDNP MAS NMR data presented here will provide the basis of future analysis.

5.3 *Materials and Methods*

5.3.1 *LOV1 expression and purification*

The C57S mutant of the LOV1 domain (amino acids 16-133) of *Chlamydomonas reinhardtii* phot was expressed in *E. coli* strain BL21(DE3) carrying an N-terminal 10x His-tag as described before.[21] The cells were disintegrated using a French Press and the protein was purified via affinity chromatography using His-bind resin (Novagen) loaded with copper sulphate. Protein was transferred into 50 mM potassium phosphate, pH 8, containing 300 mM NaCl by repeated ultrafiltration using an Amicon Ultra-15 filter device with a 10 kDa cutoff (Millipore). The final solution was concentrated to an optical density of ~20 at 450 nm (optical path length, 1 cm).

5.3.2 *MAS NMR experiment*

MAS NMR spectroscopy: The DMX-400, DMX-200, AV-100 and AV-60 MAS NMR spectrometers equipped with a 4-mm MAS probe (Bruker, Karlsruhe, Germany) were used for all MAS NMR experiments at different magnetic fields. The sample was packed into a 4-mm sapphire rotor and inserted into the MAS probe. For a homogeneous sample distribution against the rotor wall, the sample was frozen at a very low spinning frequency of 500 Hz.[28] The temperature setting was 235 K. The spinning frequency was increased to 8 kHz after the sample was completely frozen. This frequency and set temperature were used for all ^{13}C MAS NMR measurements at different magnetic fields. A simple Hahn echo pulse sequence[29] with TPPM (two-pulse phase-modulation) proton decoupling[30] was used for all NMR measurements at the magnetic fields of 9.6, 4.7 and 2.4 T. The

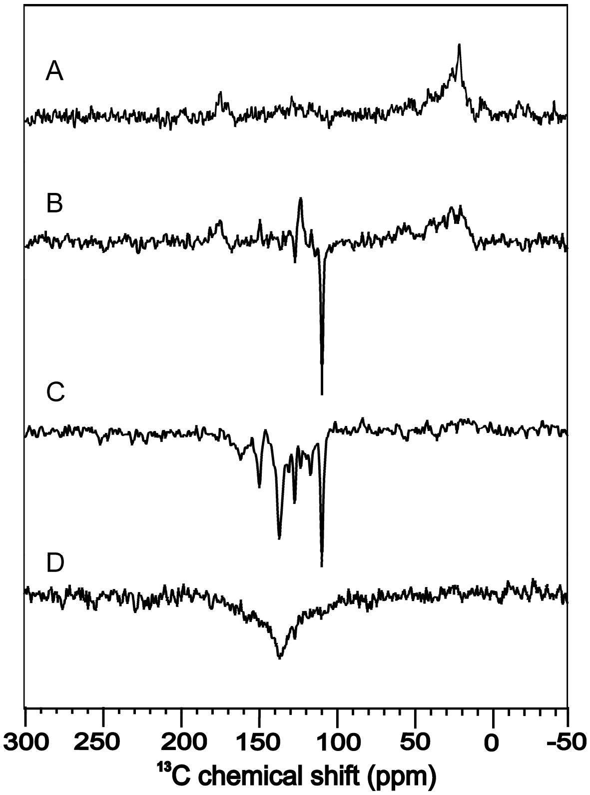

Figure 5.2: The solid-state photo-CIDNP effect in phototropin LOV1-C57S at 9.4 (A), 4.7 (B), 2.4 (C) and 1.4 T (D) observe by ^{13}C MAS NMR. Spectrum D is measured without ^{1}H decoupling. Spectra were obtained under continuous illumination with white light. Temperature was in all cases 235 K and MAS frequency 8 kHz.

hardware of the spectrometer does not allow for proton decoupling in magnetic fields less than 2.4 Tesla. Data collected in magnetic fields below 2.4 T were measured with an anti-ringing pulse sequence.[31] Continuous illumination with white light supplied by a 1 kW xenon lamp was used for all ^{13}C photo-CIDNP MAS NMR experiments.[29,32] For the four magnetic fields of 1.4, 2.4, 4.7 and 9.6 T, artificial line broadening of 10 Hz, 10 Hz, 20 Hz and 50 Hz, respectively, was applied prior to the Fourier transformation. A cycle delay of 2 s was used for all NMR experiments and signals were accumulated for 12 h. ^{13}C MAS NMR spectra were referenced with respect to the ^{13}COOH chemical shift of solid glycine at 176.04 ppm. The same phase-correction parameters required to properly phase a glycine spectrum were used for both the dark and photo-CIDNP spectra.

5.4 *Results and discussion*

Figure 5.2 shows ^{13}C MAS NMR spectra of phototropin LOV1-C57S that are CIDNP enhanced by continuous illumination with white light. The data show a solid-state photo-CIDNP effect between about ~7 and ~1 T. Light-induced signals occur at 4.7, 2.4 and 1.4 T (Spectra B-D), while essentially no induction is observed at 9.4 T (Spectrum A). The strongest effects are observed at 4.7 and 2.4 T, and the enhancement towards lower field appears to decrease, while the lack of decoupling contributes to the loss of spectral quality. The corresponding dark spectra, showing no signal, are presented in the Figure 5.3. This matching window is narrower than for the RCs of *Rb. sphaeroides* WT, which also shows significant enhancement at 17.4 and 9.4 T [chapter 3].[8,14] This is well in line with the difference in radical pair lifetime between the two species.

Figure 5.4 presents the light-induced signals in more detail. Apparently in phototropin LOV1-C57S each carbon signal has its own characteristic enhancement function. This observation contrasts previous studies on photosynthetic reaction

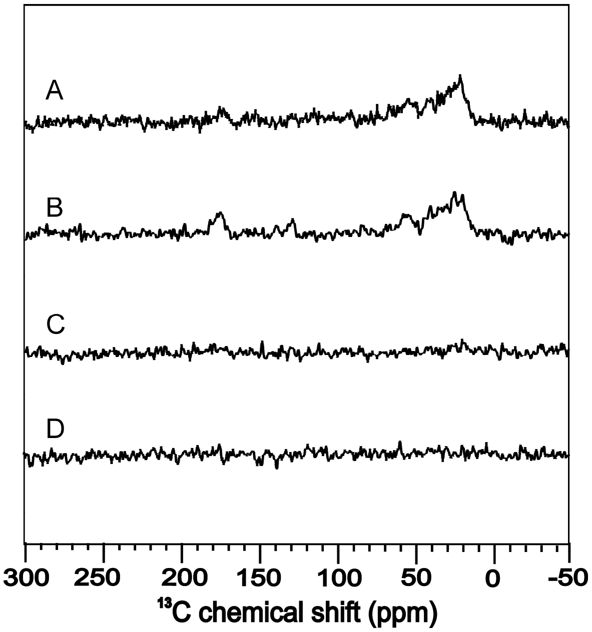

Figure 5.3: The ^{13}C MAS NMR spectra of phototropin LOV1-C57S at 9.4 (A), 4.7 (B), 2.4 (C) and 1.4 Tesla (D) under dark condition. Spectrum D is measured without ^{1}H decoupling. Spectra were obtained under continuous illumination with white light. Temperature was in all cases 235 K and MAS frequency 8 kHz

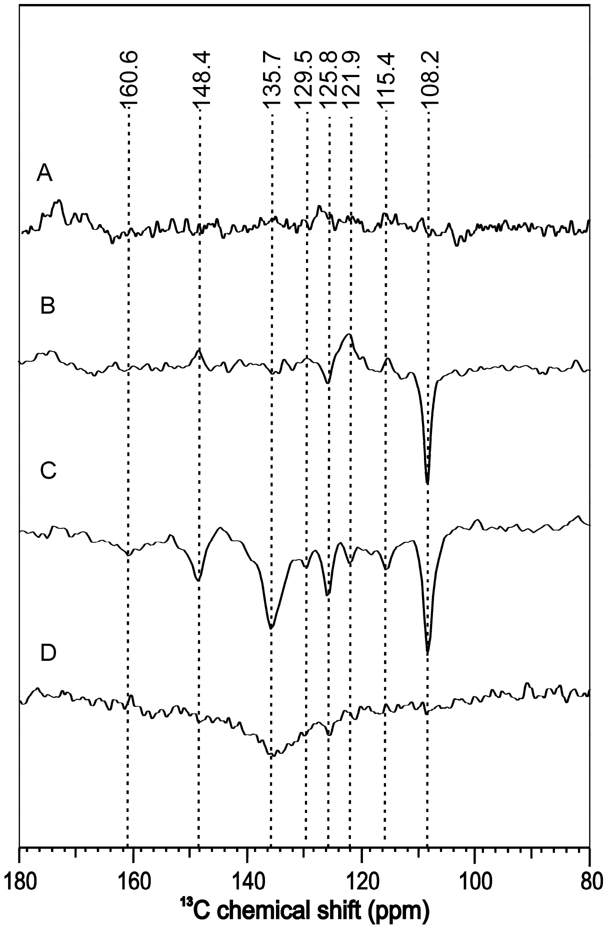

Figure 5.4: Expanded view on the spectra presented in Figure 5.2. The solid-state photo-CIDNP effect in phototropin LOV1-C57S at 9.4 (A), 4.7 (B), 2.4 (C) and 1.4 T(D) observed by ^{13}C MAS NMR. Spectrum D is measured without ^{1}H decoupling. Spectra were obtained under continuous illumination with white light. Temperature was in all cases 235 K and MAS frequency 8 kHz.

centers showing very similar enhancement factors across the carbons contributing to the ^{13}C photo-CIDNP response. The cofactors in blue-light photoreceptors that support the radical pair are significantly smaller than the chlorophylls in photosynthetic RCs and are structurally rather asymmetric. Probably substantial differences in the hyperfine parameters and their anisotropies lead to differences in field dependency for the involved nuclei.

References

(1) Zysmilich, M. G.; McDermott, A. *J. Am. Chem. Soc*. **1994**, *116*, 8362-8363.

(2) Closs, G. L.; Closs, L. E. *J. Am.Chem.Soc*. **1969**, *91*, 4549-4550.

(3) Kaptein, R.; Oosterhoff, J. L. *Chem.Phys.Lett*. **1969**, *4*, 195-197.

(4) Goldstein, R. A.; Boxer, S. G. *Biophys.J*. **1987**, *51*, 937-946.

(5) Closs, G. L. *Chem.Phys.Lett*. **1975**, *32*, 277-278.

(6) Hore, P. J.; Broadhurst, R. W. *Progr. NMR Spectrosc.***1993**, *25*, 345-402.

(7) McDermott, A.; Zysmilich, M. G.; Polenova, T. *Solid State Nuc. Magn. Reson.***1998**, *11*, 21-47.

(8) Prakash, S.; Alia; Gast, P.; de Groot, H. J. M.; Matysik, J.;Jeschke, G. *J. Am. Chem. Soc.***2006**, *128*, 12794-12799.

(9) Maier, G.; Haeberlen, U.; Wolf, H. C.; Hausser, K. H. *Phys. Lett.***1967**, *25A*, 384-385.

(10) Stehlik, D.; Colpa, J. P. *Chem. Phys*. **1977**, 21, 273-288.

(11) Jeschke, G. *J. Chem. Phys.***1997**, *106*, 10072-10086.

(12) Jeschke, G. *J. Am. Chem. Soc.***1998**, *120*, 4425-4429.

(13) Polenova, T.; McDermott, A. E. *J. Phys. Chem. B.***1999**, *103*, 535-548.

(14) Prakash, S.; Alia; Gast, P.; de Groot, H. J. M.; Jeschke, G.; Matysik, J. *J. Am. Chem. Soc.***2005**, *127*, 14290-14298.

(15) Daviso, E.; Alia, A.; Prakash, S.; Diller, A.; Gast, P.; Lugtenburg, J.; Jeschke, G.; Matysik, J. *J. Phys. Chem. C* **2009**, *113*, 10269-10278.

(16) Roy, E.; Alia; Gast, P.; van Gorkom, H.; de Groot, H. J. M.; Jeschke, G.; Matysik, J. *Biochim. Biophys. Acta***2007**, *1767*, 610-615.

(17) Roy, E.; Rohmer, T.; Gast, P.; Jeschke, G.; Alia, A.; Matysik, J. *Biochemistry***2008**, *47*, 4629-4635.

(18) Alia; Roy, E.; Gast, P.; van Gorkom, H. J.; de Groot, H. J. M.; Jeschke, G.; Matysik, J. *J. Am. Chem. Soc.***2004**, *126*, 12819-12826.

(19) Matysik, J.; Alia, Gast, P.; van Gorkom, H. J.; Hoff, A. J.; de Groot. H. J. M. *Proc. Natl. Acad. Sci. U.S.A*. **2000**, *97*, 9865-9870.

(20) Janssen, G. J.; Daviso, E.; van Son, M.; de Groot, H. J. M.; Alia, A.; Matysik, J. *Photosynth. Res.***2010**, *104*, 275-282.

(21) Kottke, T.; Heberle, J.; Hehn, D.; Dick, B.; Hegemann, P. *Biophys. J.***2003,***84*, 1192-1201.

(22) Closs, G. L. in Chemically induced magnetic polarization, NATO Advanced study institutes series (ed. by Muus, L.T.; Atkins, P. W.; McLauchlan, K. A.; Pedersen, J.B.; Reidel), Dordrecht, pp. 225-256, (1977).

(23) Biskup, T.; Schleicher, E.; Okafuji, A.; Link, G.; Hitomi, K.; Getzoff, E. D.; Weber, S. *Angew. Chem. Int. Ed.***2009,***48*, 404-407.

(24) Richter, G.; Weber, S.; Römisch, W.; Bacher, A.; Fischer, M.; Eisenreich, W. *J. Am. Chem. Soc.***2005,***127*, 17245-17252.

(25) Eisenreich, W.; Joshi, M.; Weber, S.; Bacher, A.; Fischer, M. *J. Am. Chem. Soc.***2008,***130*, 13544-13545.

(26) Kay, C. W.; Schleicher, E.; Kuppig, A.; Hofner, H.; Rüdiger, W.; Schleicher, M.; Fischer, M.; Bacher, A.; Weber, S.; Richter, G. *J. Biol. Chem.***2003,***278*, 10973-10982.

(27) Kottke, T.; Dick, B.; Fedorov, R.; Schlichting, I.; Deutzmann, R.; Hegemann, P. *Biochemistry***2003,***42*, 9854-9862.

(28) Fischer, M. R.; de Groot, H. J. M.; Raap, J.; Winkel, C.; Hoff, A. J.; Lugtenburg, J. *Biochemistry* **1992**, *31*, 11038-11049.

(29) Matysik, J.; Alia; Hollander, J. G.; Egorova-Zachernyuk, T.; Gast, P.; de Groot, H. J. M. *Indian J. Biochem. Biophys.* **2000**, *37*, 418-423.

(30) Bennett, A. E.; Rienstra, C. M.; Auger, M.; Lakshmi, K. V.; Griffin, R. G. *J. Chem. Phys.* **1995**, *103*, 6951-6958.

(31) Zhang, S.; Wu, X.; Mehring, M. *Chem. Phys. Lett.***1990**, *173,* 481-484.

(32) Matysik, J.; Schulten, E.; Alia; Gast, P.; Raap, J.; Lugtenburg, J.; Hoff, A. J.; de Groot, H. J. M. *Biol. Chem.***2001**, *382*, 1271-1276.

Chapter 6

General discussion

In the past, work on the solid-state photo-CIDNP effect received significant attention,[1,2] although its limitation to isolated, frozen, quinone reduced natural photosynthetic RCs has been a concern. Recently, some of this limit has been overcome. In particular, the solid-state photo-CIDNP effect was observed in large non-frozen photosynthetic membrane-complexes.[3] The possibility to observe the effect has also been demonstrated for cells without further isolation.[4,5] In addition, the theory of the solid-state photo-CIDNP-effect at high magnetic fields has been complemented by a low-field analogon, predicting significant nuclear polarization for various electron transfer-systems in the earth's field range.

This thesis is part of the efforts to develop the solid-state-photo-CIDNP effect to a generally applicable method for signal enhancement, similar to other hyperpolarization methods, for example dynamic nuclear polarization (DNP).[6,7] In this thesis, again several borders are addressed, extending previous experimental possibilities and also understanding, leading to a new view on the occurrence of the effect.

Although the pure observation of the effect was already possible in other cellular systems, in Chapter 2, it is demonstrated that photo-CIDNP MAS NMR can be applied as analytical tool to cellular systems. That allows to apply the method also to plenty of less studied photosynthetic systems in which isolation is difficult or unknown. Due to strong light scattering, even optical methods are difficult to apply, however, photo-CIDNP MAS NMR can study this systems in different states (here Braunstoff *vs*. Grünstoff).

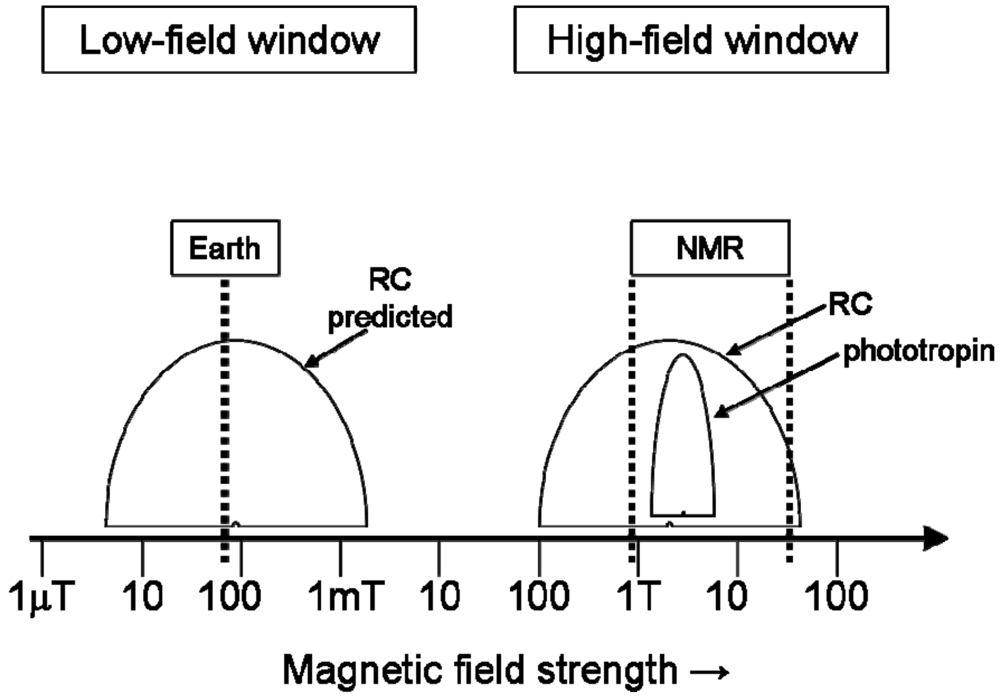

Figure 6.1: The two regimes of the solid-state photo-CIDNP effect. The high-field matching window has been fully experimentally studied in this thesis for two systems (RCs of *Rb. sphaeroides* WT, Chapter 3, and of the C57S-mutant of LOV1-phototropin, Chapter 5). The low-field matching window is theoretically predicted.

Previous experimental possibilities were limited to the magnetic field range of 17.6 to 4.7 T .[4,8] In Chapter 3, this field range is widened to low fields of 2.4 and 1.4 T. Here, for the first time, the high-field matching curve of the solid-state photo-CIDNP effect has been observed, very well in agreement with the high-field theory for RCs of *Rb. sphaeroides* WT.[4,9]

Chapter 4 presents the effect on the first non-photosynthetic system, a blue-light-photoreceptor phototropin LOV1-C57S. Hence, here it has been proven that the effect is not limited to natural photosynthetic systems but can also be observed in other electron-transfer systems. Chapter 5 provides deeper insight by showing the field dependence of the effect. It turns out that the matching window is smaller as in RCs of *Rb. sphaeroides*, inline with the assumption that the radical pair lifetime is correlated to the width of the window (Figure 6.1).

While the occurrence of the high-field matching window is now experimentally well established, observation of the predicted low-field window[10] (for example by using a shuttle system) again would open a new world in spin dynamics. The theory also predicts that this low-field effect is in particular strong for radical pairs having a distance similar to secondary radical pairs.[10] Hence, due to the larger distance, the radical-pair lifetime is in the μs- to -ms range and the matching windows must be very sharp. This selectivity of the conditions might also be the reason, why the effect is so difficult to observe in electron transfer systems as for example artificial reaction centers or cryptochromes.

If these narrow matching windows at and around earth's field could be explored experimentally, it might be possible to get direct access in the spin dynamics of light-dependent bird-navigation[11] or the stability of circadian rhythms in plants and animals.[12,13]

References

(1) Möbius, K.; Sakitsky, A. *High-Field EPR Spectroscopy on Proteins and their Model Systems Characterization of Transient Paramagnetic States, RSC publishing* (2009).

(2) Goez, M. (1997) *Photochemically induced dynamic nuclear polarization* In Advances in photochemistry, (eds. Neckers, D. C; Volman, D. H; von Bülau, G.) Wiley, New York, *Volume 23*, pp 63-163.

(3) Daviso, E.; Janssen, G. J.; Alia, A.; Jeschke, G.; Matysik, J.; Tessari, M. *J. Am. Chem. Soc.* **2011**, *133*, 16754-16757.

(4) Prakash, S.; Alia; Gast, P.; de Groot, H. J. M.; Matysik, J.; Jeschke, G. *J. Am. Chem. Soc.* **2006**, *128*, 12794-12799.

(5) Janssen, G. J.; Daviso, E.; van Son, M.; de Groot, H. J. M.; Alia, A.; Matysik, J. *Photosynth. Res.* **2010**, *104*, 275-282.

(6) Griffin, R. G.; Prisner, T. F. *Phys. Chem. Chem. Phys.* **2010**, *12*, 5737-5740.

(7) Leggett, J.; Hunter, R.; Granwehr, J.; Panek, R.; Perez-Linde, A. J.; Horsewill, A. J.; McMaster, J.; Smith, G.; Kockenberger, W. *Phys. Chem. Chem. Phys.* **2010**, *12*, 5883-5892.

(8) Prakash, S.; Alia; Gast, P.; de Groot, H. J. M.; Matysik, J.; Jeschke, G. *J. Am. Chem. Soc.* **2006**, *128*, 12794-12799.

(9) Diller, A.; Prakash, S.; Alia, A.; Gast, P.; Matysik, J.; Jeschke, G. *J. Phys. Chem. B.* **2007**, *111*, 10606-10614.

(10) Jeschke, G.; Anger, B. C.; Bode, B. E.; Matysik, J. *J Phys Chem A*, *115*, 9919-28.

(11) Ritz, T.; Adem, S.; Schulten, K. *Biophys. J.* **2000**, *78*, 707-718.

(12) Christie, J. M. *Annu Rev Plant Biol* **2007**, *58*, 21-45.

(13) Miyamoto, Y.; Sancar, A. *Proc Natl Acad Sci U S A* **1998**, *95*, 6097-102.

Summary

Solid-state photochemically induced dynamic polarization (photo-CIDNP) is one of the hyperpolarization techniques that tremendously enhances the sensitivity and selectivity of solid state NMR. This thesis addressed several new issues concerning the capacity of photo-CIDNP MAS NMR as hyperpolarization technique: The applicability to cells, the use of medium magnetic fields and its occurrence in non-photosynthetic systems. It is based on the solid-state photo-CIDNP effect which was first observed in 1994 in quinone-depleted bacterial RCs of purple bacteria *Rb. sphaeroides* under illumination and detected by enhanced MAS NMR signals as a dramatic modification of signal intensities. As shown in the Introduction (Chapter 1), the solid-state photo-CIDNP effect is based on several mechaninsms transferring the original electron spin order occurring at the birth of the radical pair to nuclear polarization. The maximum enhancement of this effect was observed at the magnetic field of 4.7 Tesla at about a factor of 10000. Over the years, this technique has proved to be very efficient in understanding the electronic structures of the RCs in several photosynthetic bacteria and plants.

The solid-state photo-CIDNP effect of heliobacterial (*Hb. mobilis*) cells is analytically used in Chapter 2. The pigment in strictly anaerobic *Hb. mobilis* cells (Braunstoff) is photoconverted with bubbling oxygen to a pigment which is very common in aerobic photosynthesis. The bacteria also change their colour to green (Grünstoff). Both forms of these *Hb. mobilis* cells are analyzed by whole-cell ^{15}N and ^{13}C photo-CIDNP MAS. The experiments on ^{15}N and ^{13}C isotope labelled *Hb. mobilis* cells reveal the identity of the radical pair in both forms of *Hb. mobilis*. Time resolved experiments on ^{15}N and 3-^{13}C-ALA labelled *Hb. mobilis* Braunstoff cells demonstrate a remarkable similarity with the photo-CIDNP response from the RC of *Rb. sphaeroides* R26. In Grünstoff, early mobility of triplet states is observed. The colour change and different spectral patterns are explained by the photoconversion of accessory cofactors. This study expands the application of the

solid-state photo-CIDNP effect to explore also natural systems in which the protein purification is impossible or difficult.

The maximum enhancement of the solid state photo-CIDNP effect was observed for a magnetic field of 4.7 Tesla in the quinone depleted RCs of *Rb. sphaeroides* WT and R26. In Chapter 3, the magnetic field dependent studies of the solid state photo-CIDNP effect are expanded to lower magnetic fields as 2.4 and 1.4 Tesla. WT and R26 RCs show different enhancement patterns in magnetic fields less than 4.7 Tesla. In WT RCS, the observed matching curve is well in agreement with the solid-state photo-CIDNP theory. In R26 RCs, the maximum enhancement factor of about 80000 is observed close to a magnetic field of 1.4 Tesla. This pure contribution of the DR mechanism allows to explore the electron spin density distribution of donor triplet state in R26 RCs.

Until now, the solid-state photo-CIDNP effect was considered to be an intrinsic property of photosynthetic RCs. The first observation of the solid-state photo-CIDNP effect for the blue-light photoreceptor phototropin LOV1-C57S is presented in Chapter 4. Magnetic field dependent studies of this protein are presented in Chapter 5. Also here a matching profile is observed that is narrower than the profile observed for WT RCs. It is assumed that the short radical pair lifetime in photosynthetic RCs leads to broad matching functions and therefore straightforward experimental observation.

We addressed several new issues concerning the capacity of photo-CIDNP MAS NMR as hyperpolarization technique: The applicability to cells, the use of medium fields and its occurrence in non-photosynthetic systems. In Chapter 6, it is assumed that photo-CIDNP effects are rather common in electron transfer systems, if the right conditions are applied. Long radical pair life times will lead to short matching windows. Hence, equipment as shuttle systems will have to be applied to operate in this regime. Upon success, photo-CIDNP MAS NMR has a chance to become an attractive generally applicable hyperpolarization method.

Samenvatting

Vaste stof ‘photochemicallyinduced dynamic polarisation’ (photo-CIDNP) is één van dehyperpolarisatie technieken die leidt tot zowel een sterke toename in de gevoeligheid als ook in de selectiviteit van vaste stof NMR. In dit proefschrift worden verschillende nieuwe kwesties besproken betreffende de potentie van photo-CIDNP MAS NMR als hyperpolarisatie techniek:Het gebruik van medium sterke magnetische velden en de toepasbaarheid op hele cellen en niet-fotosynthetische systemen. De techniek is gebaseerd op het vaste stof photo-CIDNP effect dat voor het eerst werd waargenomen in 1994 door belichting van het reactiecentrumvan purper bacterie *Rb. Sphaeroides* waaruit de chinonen waren verwijderd.Het werd met MAS NMR gedetecteerd als een sterke toename van de signaalintensiteit. Zoals blijkt uit de inleiding (hoofdstuk 1), is het vaste stof photo-CIDNP effect gebaseerd op verschillende mechanismen die de elektron spin correlatie van een licht-geïnduceerd radicaalpaar omzetten naar nucleaire polarisatie. De tot nu toe maximale versterkingbehaald met dit effect, een factor 10000, is waargenomen bij eenmagnetisch veld van 4,7 Tesla. In de loop der jaren heeft deze techniek bewezen uiterst doeltreffend te zijn voor het begrijpen van de elektronische structuren van fotosynthetische reactiecentra in verschillende soortenbacteriën en planten.

Het vaste stof photo-CIDNP effect van heliobacteriële (*Hb. mobilis*) cellen wordt analytisch toegepastin hoofdstuk 2. Het pigment in strikt anaerobische *Hb. mobilis* cellen (Braunstoff) wordt door een interactie met licht en borrelende zuurstof omgezet in een pigment dat zeer veelvoorkomtin aerobe fotosynthese. De bacteriën veranderen hierdoor ook vankleur en wordengroen (Grünstoff). Beide vormen van deze *Hb. mobilis* cellen zijngeanalyseerd met ^{15}N en ^{13}C Photo-CIDNP MASNMRexperimenten met hele cellen. De experimenten met ^{15}N en ^{13}C isotoop gelabelde *Hb. mobilis* cellen onthullende identiteit van het radicaalpaar in beide vormen van *Hb. mobilis*. Tijdsopgeloste experimenten op uniform en selectief ^{15}N en ^{13}C gelabelde *Hb. mobilis* Braunstoff cellen laten een opmerkelijk grote overeenkomst zien met eerder verkregen resultaten vanexperimenten met reactiecentra van *Rb. sphaeroides* R26. In Grünstoff is vroege mobiliteit van de triplet toestand waargenomen. De kleurverandering en verschillende spectrale patronen van Braunstoff en Grünstoffkunnen worden verklaard metde licht-geïnduceerde chemische omzetting van de 'accessory' cofactoren. Dit onderzoek vergroot de mogelijkheden voor de toepassing van het vaste stof photo-CIDNP effect voor het bestuderen van natuurlijke systemen waarvoor eiwitzuivering onmogelijk is of die anderszins moeilijk zijnte onderzoeken.

De maximale versterking van hetvaste stof photo-CIDNP signaal werd waargenomen bij een magneetveld van 4,7 Tesla in reactiecentra van *Rb. sphaeroides* WT en R26 waaruit de chinonen verwijderd zijn. De magneetveldafhankelijke experimenten van het vaste stof photo-CIDNP effect worden in hoofdstuk 3 uitgebreid naar lagere magneetvelden van 2,4 en 1,4 Tesla. WT en R26 reactiecentra van *Rb. sphaeroides* hebben verschillendeversterkingspatronen in magnetische velden van minder dan 4,7 Tesla. De waargenomen matching curve van WT reactiecentra is in goede overeenstemming met de vaste stof photo-CIDNP theorie. In R26 reactiecentra wordt een maximale versterkingsfactor van ongeveer 80000 waargenomen bijeen magnetische veldsterkte van rond de1,4 Tesla. Dit is een zuiverebijdrage van het DR mechanisme en maakt het mogelijk om de elektron spin-dichtheidsverdeling van de donor triplet toestand in R26 reactiecentrate onderzoeken.

Tot nu toe werd het vaste stof photo-CIDNP effect beschouwd als een intrinsieke eigenschap van fotosynthetische reactiecentra. De eerste waarneming van het vaste stof photo-CIDNP effect in een ander eiwit, de blauwe licht fotoreceptor fototropine LOV1-C57S, wordt gepresenteerd in hoofdstuk 4. Magneetveldafhankelijk onderzoek naar dit eiwit wordt gepresenteerd in hoofdstuk 5. Hier wordt ook een 'nauwere' matching voorwaardewaargenomen dan geldt voor WT reactiecentra. Ditwordt toegeschreven aan een langere levensduur van het radicaalpaar. Aangenomen wordt dat eenkortere levensduur van het radicaalpaar in fotosynthetische reactiecentra leidt tot bredere matching voorwaarden,waardoor het Photo-CIDNP effect hier relatief eenvoudig experimenteelkan worden waargenomen.

We hebben verschillende nieuwe zaken besprokenomtrent de capaciteit van het photo-CIDNP MAS NMR als hyperpolarisatie techniek: De toepasbaarheid op cellen, het gebruik van verschillendemagneetveldsterktes en de observatie van het photo-CIDNP effect in niet-fotosynthetische systemen. In hoofdstuk 6 wordt aangenomen dat het photo-CIDNP effect veelvuldig voorkomt in elektron transfer systemen met de juiste fysisch-chemische eigenschappen. Radicaalparen met eenlange levensduurzullen leiden tot nauwe matching voorwaardenen dus is het nodig om nieuwe apparatuur zoals shuttlesystemen te gebruiken om in dit gebied te kunnen werken. Indien succesvol heeft photo-CIDNP MAS NMR een kans om een aantrekkelijke, algemeen toepasbare hyperpolarisatie methode te worden.

List of publications

- Smitha Surendran Thamarath, A. Alia, Esha Roy, Karthick Babu Sai Sankar Gupta, John Golbeck, Jörg Matysik. "The field-dependence of the solid-state photo-CIDNP effect in two states of heliobacterial reaction centers". Photosyn. Res., in press.

- Xiaojie Wang, Smitha Surendran Thamarath, Jörg Matysik. "Magnetic-field dependence of the solid-state photo-CIDNP effect observed in phototropin LOV-C57S". Acta Chim. Sinica 71, 169-172 (2013).

- Bela E. Bode, Smitha Surendran-Thamarath, Karthick Babu Sai Sankar Gupta, A. Alia, Gunnar Jeschke, Jörg Matysik. "The solid-state photo-CIDNP effect and its analytical application". In: Hyperpolarization methods in NMR spectroscopy" (Lars Kuhn, ed.) Springer, pp. 105-121 (2013).

- Smitha Surendran Thamarath, A. Alia, Eugenio Daviso, Deni Mance, John H. Golbeck, Jörg Matysik (2012) Whole-cell NMR characterization of two photochemically active states of the photosynthetic reaction center in heliobacteria. *Biochemistry* 51 (29): 5763–5773.

- Smitha Surendran Thamarath, Bela E. Bode, Shipra Prakash, Karthick Babu Sai Sankar Gupta, A. Alia, Gunnar Jeschke, and Jörg Matysik (2012) Electron spin density distribution in the special pair triplet of *Rhodobacter sphaeroides* R26 revealed by magnetic field dependence of the solid-state photo-CIDNP Effect. *J. Am. Chem. Soc.* 134: 5921–5930.

- Smitha Surendran Thamarath, Joachim Heberle, P. J. Hore, Tilman Kottke, and Jörg Matysik (2010) Solid-state photo-CIDNP effect observed in phototropin LOV1-C57S by ^{13}C magic-angle spinning NMR spectroscopy. *J. Am. Chem. Soc.* 132: 15542–15543.

- Sreeja, T. S. Smitha, Deepak Nand, T. G. Ajithkumar and P. A. Joy (2008) Size dependent coordination behavior and cation distribution in $MgAl_2O_4$ nanoparticles from ^{27}Al solid state NMR studies. *J. Phys. Chem. C* 112: 14737–14744.

Curriculum Vitae

Following the completion of my schooling in 2001, I joined Sree Kerala Varma College, Thrissur, to pursue my bachelor's degree in Chemistry. I graduated in 2004 and undertook my master's studies in Applied Chemistry at the Department of Chemistry, Calicut University, Kerala. As part of my postgraduate study, I undertook a short term project titled "Solid state NMR studies of $MgAl_2O_4$ nanoparticles" under the supervision of Dr. T. G. Ajithkumar at National Chemical Laboratory (NCL), Pune. On securing my master's degree in October 2006, I worked as project assistant in the solid state NMR group of the NCL, Pune during which time I continued to work on my Masters project which saw completion in March 2008. In April 2008, I started my PhD under the supervision of Dr. J. Matysik in the Solid state NMR group of Prof. H. J. M. de Groot at the University of Leiden. As a part of my doctoral studies, I attended the Summer school "Advanced course in Solid state NMR" in 2008 at Denmark. I also had the opportunity of presenting my work in the form of posters at the Euromar Conference 'Magnetic Resonance for the Future' at St. Petersburg in 2008, the 43rd Meeting of the Dutch NMR-Discussion group at Eindhoven in 2008, the NWO meeting 'Spectroscopy and Theory' at Lunteren in 2009, the 6th Alpine Conference on Solid State NMR at Chamonix, France, in 2009, the 44th meeting of the Dutch NMR-DG in Leiden in 2009, the NWO meeting 'Spectroscopy and Theory' at Veldhoven in 2010, the Discussion Meeting and the Joint Benelux/German MR Conference at Münster in 2010, the Spin Chemistry Meeting at Noordwijk in 2011, the Reedijk Symbosium in Leiden in 2011 and the Physics@FOM at Veldhoven in 2012. I finally presented my work at the workshop 'Hot Topics in Spin-Hyperpolarization' in Leiden, The Netherlands, in 2012.